New approaches to study the marine carbon cycle

Andrea J. Fassbender

A dissertation

submitted in partial fulfillment of the

requirements for the degree of

Doctor of Philosophy

University of Washington

2014

Reading Committee:

Christopher L. Sabine, Chair

Paul D. Quay

Richard A. Feely

Program Authorized to Offer Degree:

School of Oceanography

University of Washington

Abstract

New approaches to study the marine carbon cycle

Andrea J. Fassbender

Chair of the Supervisory Committee:
Affiliate Professor Christopher L. Sabine
School of Oceanography

Seven years of *in situ* salinity and carbon dioxide (CO_2) measurements from two moorings located in the North Pacific Ocean were used to evaluate transformations in mixed-layer total alkalinity (TA) and dissolved inorganic carbon (DIC) using a time-dependent mass-balance approach. Results from the Kuroshio Extension Observatory (KEO) and Ocean Station Papa (OSP) moorings indicate that the physical input of carbon is primarily counterbalanced by biological processes over the annual cycle. At KEO these processes are highly coupled, while at OSP they are somewhat decoupled due to alternative limiting nutrient supply mechanisms. The annual net community production (NCP) at KEO was 4.5 ± 2.2 mol C m^{-2} yr^{-1} and at OSP was 1.9 ± 0.5 mol C m^{-2} yr^{-1}. Although NCP is higher at KEO, it occurs over ~4 months in spring and has little influence on the air-sea CO_2 exchange, while production at OSP occurs over ~7 months from winter to summer and has a large influence on sea surface CO_2 throughout the year. In addition, the low buffer capacity of waters at OSP makes it 50% easier for biology to reduce CO_2 levels than at KEO, which contributes to the larger role of biology in atmospheric CO_2 uptake at

OSP. Discovery of the complex interplay and timing of physics, biology and chemistry in these regions highlights the value of high-frequency, continuous observations.

This new dual-carbon-tracer approach makes it possible to study the drivers of ocean carbon cycling remotely, but relies upon the calculation of DIC from *in situ* salinity and CO_2 data when the direct measurement of DIC would be more ideal. To improve *in situ* carbon cycle study capabilities, a novel DIC sensor with an accuracy of ±5 μmol kg^{-1} was designed for extended-duration (>year) surface ocean monitoring. Results from two field tests of the prototype sensor indicate that direct measurement of DIC is ~90% more accurate than calculating DIC from collocated and contemporaneous measurements of pH and pCO_2. This sensor now makes it possible to directly measure the surface ocean carbon inventory and to conduct high-accuracy carbon cycle studies autonomously over the entire annual cycle.

Acknowledgements

The completion of this dissertation would not have been possible without the support and collaboration of numerous people that I have had the opportunity to work with and learn from while attending the University of Washington, School of Oceanography. I am truly grateful to everyone who has assisted me in this challenging journey.

I will start by thanking my academic advisor, Christopher Sabine. Thank you for introducing me to the world of marine carbon cycling and for providing unique and challenging opportunities to push scientific boundaries. Thanks to your example, I have learned so much about science and the way I'd like to do it as I move forward in my career. Your encouragement, along with the freedom you've given me to approach tough problems on my own, has allowed me discover what I can accomplish and has given me the confidence to continue pursuing my goals.

Thank you to the other members of my PhD committee: Richard Feely, Kathryn Kelly, Paul Quay, and Becky Alexander Suess. Your intellectual contributions throughout graduate school have guided me along this research path. I am glad to have gotten to know each of you as scientists, mentors, and people who have a sense of humor.

Thank you to the members of the Pacific Marine Environmental Laboratory (PMEL) Carbon Group and Engineering Development Division (EDD). I have enjoyed collaborating with you throughout this journey. I especially want to thank Noah Lawrence-Slavas from EDD, who worked with me tirelessly on the development of a moored dissolved inorganic carbon sensor. This project was a test of patience, and your positive attitude in all situations is something I truly

admire. I also would like to thank Stacy Maenner Jones from the Carbon Group for being an excellent friend, teacher, and colleague. You go out of your way to help me and others, and it does not go unnoticed.

Throughout the past 7.5 years, I am thankful to have enjoyed the friendship of so many students in the University of Washington School of Oceanography, Program on Climate Change, and IGERT Program on Ocean Change. In particular, it has been a blessing to have Kirsten, Elizabeth, Jesse, and Alyssa in my life. Earning a doctorate takes perseverance, and with you girls around, it just seemed like fun.

Finally, I want to thank my family. Without your support and encouragement this journey would have been exponentially more difficult. I am so thankful to have you in my life and I appreciate all that you have done for me. This achievement is shared with you.

Financial support for this research was provided by the National Oceanic and Atmospheric Administration (NOAA) Climate Program Office, the NOAA Ocean Acidification Program, the NOAA Global Carbon Cycle Program, the University of Washington (UW) Graduate School, the UW Program on Climate Change, and the UW IGERT Program on Ocean Change.

Table of Contents

List of Tables

List of Figures

Chapter 1

Biogeochemical controls on the ocean carbon inventory

1. Background

The ocean plays a major role in the carbon cycle [*Sabine et al.*, 2004; *Houghton*, 2007; *Gruber et al.*, 2009; *Le Quéré et al.*, 2009, 2014; *Ciais et al.*, 2013]. Approximately 50% of global photosynthetic carbon fixation occurs in the ocean by organisms that 1) make up only 0.2% of the photosynthetically active carbon biomass on Earth and 2) turn over on a weekly basis [*Falkowski*, 1998; *Field*, 1998]. When these organisms die and sink, or are passed to upper trophic levels and respired or excreted at depth, there is a transfer of carbon from the sunlit ocean surface to the ocean interior. This leaves a deficit of carbon in the surface ocean, allowing carbon dioxide (CO_2) gas exchange to occur across the air-sea boundary, transferring CO_2 from the atmosphere into the ocean. This biologically mediated transport of carbon, commonly referred to as the biological pump, gives rise to a strong vertical carbon gradient in the ocean [*Sarmiento and Gruber*, 2006b; *Emerson and Hedges*, 2008]. The biological pump, coupled with ocean circulation and chemical kinetics of air-sea gas exchange, allows the ocean to hold ~50 time more carbon than the atmosphere [*Sarmiento and Gruber*, 2006a; *Rhein et al.*, 2013].

In steady state, the biological carbon export from the ocean surface to the interior is equal to the amount carbon, and nutrients, that are physically upwelled to the sea surface, though these processes can occur in different regions [*Falkowski*, 1998]. In modern times, ~11 Pg of carbon is transported into and out of the intermediate ocean annually through the biological pump and upwelling, and only ~0.2 Pg of carbon escapes this loop and makes it to the seafloor [*Ciais et al.*,

2013]. The ocean has a long chemical memory due to its size and slow circulation [*Archer et al.*, 1998]. Changes in the efficiency at which the biological pump transports carbon to the ocean interior can, thus, have a significant influence on atmospheric CO_2 by increasing or decreasing the carbon input to the ocean reservoir, while it takes much longer for the upwelled carbon output to adjust and for a new equilibrium carbon inventory to be reached [*Sigman and Boyle*, 2000]. This type of biologically induced geochemical disequilibrium is thought to have caused atmospheric CO_2 levels to change by nearly 100 µatm during glacial-interglacial transitions that occurred throughout the past 800,000 years, highlighting the critical link between marine primary producers, ocean chemistry and physics, and global climate [*Archer and Maier-Reimer*, 1994; *Sigman and Boyle*, 2000].

In the past ~250 years, humans have released ~365 Pg of carbon to the atmosphere through the extraction and burning of fossil fuels [*Ciais et al.*, 2013]. This has increased atmospheric CO_2 concentrations by ~120 µatm, which is equivalent to the glacial-interglacial changes in atmospheric CO_2 that occurred over thousands of years [*Gattuso and Hansson*, 2011]. Anthropogenic CO_2 uptake by the ocean and terrestrial biosphere have reduced the atmospheric CO_2 growth rate by 50%, slowing the rate of global climate change. The ocean is responsible for absorbing ~25% of anthropogenic CO_2 emissions annually through air-sea gas exchange that is currently thought to be driven entirely by human induced changes in the atmospheric partial pressure of CO_2 [*Takahashi et al.*, 2009; *Le Quéré et al.*, 2014], as no discernable change in the biological pump has been identified. As CO_2 dissolves in seawater, it reacts with water to form a weak acid that rapidly deprotonates [*Millero*, 2007]. Thus, anthropogenic carbon uptake by the ocean has resulted in a 30% decline in sea surface pH levels due to this chemical reaction, a process

commonly referred to as ocean acidification [*Orr et al.*, 2005; *Doney et al.*, 2009a; *Gattuso and Hansson*, 2011]. In addition, global warming caused by the modern radiative imbalance has led to significant warming of the surface ocean [*Lyman et al.*, 2010]. Due to the important link between the biological pump and climate, and the numerous feedback mechanisms therein, there is a desire to better understand how ocean warming and acidification may impact marine carbon cycling [*Doney*, 2006, 2009; *Doney et al.*, 2012; *Passow and Carlson*, 2012].

Efforts to better understand anthropogenic CO_2 uptake by the ocean in the past few decades have led to the routine measurement of sea surface carbon dioxide [*Takahashi et al.*, 2009; *Bakker et al.*, 2014]. Millions of CO_2 measurements collected over these decades have made it possible to resolve the seasonal cycle of air-sea CO_2 flux throughout the oceans, revealing that the temperate latitudes are strong annual carbon sinks for atmospheric CO_2 [*Takahashi et al.*, 2006, 2009]. In particular, there are a growing number of moored time-series locations where continuous *in situ* observations of atmospheric and sea surface CO_2 measurements are being made [*Sutton et al.*, 2014]. These growing observational datasets can provide useful information about carbon cycle processes and responses to environmental variability on daily to decadal timescales.

In order to fully characterize the inorganic carbon chemistry of seawater and quantitatively study the carbon cycle, two carbonate system parameters must be measured simultaneously. The four carbonate system parameters that have been routinely measured from ships are: dissolved inorganic carbon (DIC), total alkalinity (TA), partial pressure of carbon dioxide (CO_2) and pH. Any two of these parameters can be used to calculate all other components of the carbonate system using equilibrium constants, temperature, pressure, and salinity [*Dickson et al.*, 2007; *van Heuven*

et al., 2011]. DIC is the sum of all dissolved inorganic carbon species and represents the total carbon inventory of the ocean. As the master carbon variable, DIC is influenced by all processes that affect seawater carbon chemistry, including biology.

It is generally best to directly measure the environmental variable of interest; however, autonomous DIC sensors are not yet commercially available for moored application. Advances in autonomous pH and CO_2 instrumentation now make it possible to measure these two parameters simultaneously at moored time-series locations, and to calculate DIC. CO_2 and pH strongly covary, however, so high-accuracy measurements are required in order to accurately compute other carbonate system parameters from this pair [*Dickson and Riley*, 1978; *Millero*, 2007; *Cullison Gray et al.*, 2011]. In consideration of growing time-series observations that link present and past ocean conditions, and the requirement of a modern reference point from which to assess changes in the marine carbon cycle, new techniques are needed that can leverage the available data and expand autonomous observing capabilities.

2. Overview of Research

With significant uncertainty surrounding the biogeochemical responses to ocean change, the goal of this thesis is to contribute a quantitative, modern reference point for carbon cycling in two regions of the North Pacific Ocean using autonomous inorganic carbon sensors. In particular, this work addresses the importance of continuous, high-frequency observations in learning about biogeochemical responses to different timescales of environmental forcing and contributes new observational capabilities for autonomous carbon cycle studies.

The North Pacific Ocean accounts for ~25% of the annual anthropogenic CO_2 uptake, much of which occurs across a swath of the basin at the boundary between the subtropical gyre and the subarctic region (~30ºN-45ºN; *Takahashi et al.*, 2002, 2009). Sustained carbon uptake in this region has been attributed to the geostrophic transport of low-DIC waters as well as biological activity [*Ayers and Lozier*, 2012]. Ocean Station Papa (OSP), located at 50°N, 145°W in the North Pacific Ocean, is a time-series site with a long history of chemical, physical, and biological observations [*Freeland*, 2007]. Numerous investigators have estimated the role of biology on carbon cycling at OSP [*Takahashi et al.*, 1993; *Wong et al.*, 1995, 2002a, 2002b, 2002c; *Signorini et al.*, 2001; *Emerson and Stump*, 2010; *Emerson et al.*, 2011; *Giesbrecht et al.*, 2012; *Lockwood et al.*, 2012]. Most of these assessments are based on summertime observations or winter-to-summer nutrient drawdown, in which seasonal resolution of biological processes is lost. Spring and winter observations, in particular, are lacking in terms of quantitative organic carbon and calcium carbonate ($CaCO_3$) production estimates. Thus, there are still questions about the seasonal cycle of biological production at OSP and how it influences the surface ocean carbon inventory.

Chapter 2 describes the use of a dual-tracer, mass-balance model that has been adapted from prior approaches [*Gruber et al.*, 1998; *Quay and Stutsman*, 2003; *Keeling et al.*, 2004] to diagnostically assess the processes that control mixed-layer DIC and TA at OSP. Three-hour CO_2 and pH measurements from the NOAA Ocean Station Papa mooring have been collected nearly continuously for seven years, providing high-temporal-resolution time series. These data were used to evaluate how the mixed-layer carbon inventory was affected by gas exchange, physics, evaporation and precipitation, and biology on a daily timescale throughout each of the seven annual deployments. After identifying complications in directly calculating DIC from the pH-CO_2

pair, an alternative approach was used to calculate mixed-layer DIC from salinity based estimates of TA and *in situ* measurements of CO_2. By evaluating changes in both TA and DIC within the mixed layer, the biological component of the budget could be separated into organic carbon production and inorganic carbon production components. The results of this analysis provide new, quantitative insights about the chemical, physical, and biological drivers of carbon cycling at OSP throughout the year.

The same approach was taken in Chapter 3 to evaluate controls on mixed-layer DIC at the NOAA Kuroshio Extension Observatory (KEO), located at 32.3°N, 144.6°E in the North Pacific Ocean recirculation gyre, just south of the Kuroshio Extension (KE) jet. Estimates of net biological carbon export from the mixed layer in this region are generally twice as large as those found in the eastern subarctic Pacific near OSP [*Wong et al.*, 2002b; *Sugiura and Tsunogai*, 2005; *Chierici et al.*, 2006; *Lockwood*, 2013; *Yasunaka et al.*, 2013, 2014; *Lin et al.*, 2014]. Seven years of three-hour CO_2 measurements collected at the KEO mooring were coupled with TA estimates from a regional salinity-based proxy to assess the physical, chemical and biological influences on carbon cycling at this location. Results from the analyses at both moorings are compared and the drivers of regional carbon cycle dynamics are discussed.

Chapter 4 builds off of the lessons learned from Chapter 2 about the challenges of using the pH-CO_2 pair of carbonate system parameters to calculate DIC and TA when laboratory-determined sensor accuracies are not met in the field. This chapter describes work that has been conducted in collaboration with the Pacific Marine Environmental Laboratory Engineering Development Division to develop a moored DIC sensor for extended autonomous carbon cycle studies. Details

about the sensor design and methodology are shared, as well as the results from a one-month field test in the Puget Sound, Washington and a seven-month fully autonomous deployment near Honolulu, Hawaii.

Major findings from these research projects are summarized in Chapter 5.

3. References

Archer, D., and E. Maier-Reimer (1994), Effect of deep-sea sedimentary calcite preservation on atmospheric CO_2 concentration, *Nature*, *367*(6460), 260–263.

Archer, D., H. Kheshgi, and E. Maier-Reimer (1998), Dynamics of fossil fuel CO_2 neutralization by marine $CaCO_3$, *Global Biogeochem. Cycles*, *12*(2), 259–276.

Ayers, J. M., and M. S. Lozier (2012), Unraveling dynamical controls on the North Pacific carbon sink, *J. Geophys. Res.*, *117*(C1), C01017, doi:10.1029/2011JC007368.

Bakker, D. C. E. et al. (2014), An update to the Surface Ocean CO_2 Atlas (SOCAT version 2), *Earth Syst. Sci. Data*, *6*(1), 69–90, doi:10.5194/essd-6-69-2014.

Bates, N. R., Y. M. Astor, M. J. Church, K. I. Currie, J. Dore, M. Gonaález-Dávila, L. Lorenzoni, F. Muller-Karger, J. Olafsson, and M. Santa-Casiano (2014), A Time-Series View of Changing Ocean Chemistry Due to Ocean Uptake of Anthropogenic CO_2 and Ocean Acidification, *Oceanography*, *27*(1), 126–141, doi:10.5670/oceanog.2014.16.

Chierici, M., A. Fransson, and Y. Nojiri (2006), Biogeochemical processes as drivers of surface fCO_2 in contrasting provinces in the subarctic North Pacific Ocean, *Global Biogeochem. Cycles*, *20*(1), doi:10.1029/2004GB002356.

Ciais, P. et al. (2013), Carbon and Other Biogeochemical Cycles, in *Climate Change 2013: The Physical Science Basis*, edited by V. B. and P. M. M. (eds. . Stocker, T.F., D. Qin, G.-K. Plattner, M. Tignor, S.K. Allen, J. Boschung, A. Nauels, Y. Xia, Cambridge University Press, Cambridge, United Kingdom and New York, NY, USA.

Cullison Gray, S. E., M. D. DeGrandpre, T. S. Moore, T. R. Martz, G. Friederich, and K. S. Johnson (2011), Applications of in situ pH measurements for inorganic carbon calculations, *Mar. Chem.*, *125*, 82–90, doi:10.1016/j.marchem.2011.02.005.

Dickson, A., C. Sabine, and J. Christian (Eds.) (2007), *Guide to best practices for ocean CO_2 measurements*, PICES Special Publication 3, 191 pp.

Dickson, A. G., and J. Riley (1978), The effect of analytical error on the evaluation of the components of the aquatic carbon-dioxide system, *Mar. Chem.*, *6*, 77–85, doi:10.1016/0304-4203(78)90008-7.

Doney, S. C. (2006), Plankton in a warmer world, *Nature*, *444*, doi:10.1029/2003GB002134.

Doney, S. C., V. J. Fabry, R. A. Feely, and J. a. Kleypas (2009a), Ocean acidification: the other CO_2 problem., *Ann. Rev. Mar. Sci.*, *1*(1), 169–92, doi:10.1146/annurev.marine.010908.163834.

Doney, S. C., B. Tilbrook, S. Roy, N. Metzl, C. Le Quéré, M. Hood, R. A. Feely, and D. Bakker (2009b), Surface-ocean CO_2 variability and vulnerability, *Deep Sea Res. Part II Top. Stud. Oceanogr.*, *56*(8-10), 504–511, doi:10.1016/j.dsr2.2008.12.016.

Doney, S. C. et al. (2012), Climate Change Impacts on Marine Ecosystems, *Ann. Rev. Mar. Sci.*, *4*(1), 11–37, doi:10.1146/annurev-marine-041911-111611.

Emerson, S. R., and J. I. Hedges (2008), Life Processes in the Ocean, in *Chemical Oceanography and the Marine Carbon Cycle*, Cambridge University Press, New York.

Emerson, S. R., and C. Stump (2010), Net biological oxygen production in the ocean—II: Remote in situ measurements of O_2 and N_2 in subarctic pacific surface waters, *Deep Sea Res. Part I Oceanogr. Res. Pap.*, *57*(10), 1255–1265, doi:10.1016/j.dsr.2010.06.001.

Emerson, S. R., C. L. Sabine, M. F. Cronin, R. A. Feely, S. E. Cullison Gray, and M. D. DeGrandpre (2011), Quantifying the flux of $CaCO_3$ and organic carbon from the surface ocean using in situ measurements of O_2, N_2, pCO_2, and pH, *Global Biogeochem. Cycles*, *25*(3), 1–12, doi:10.1029/2010GB003924.

Falkowski, P. G. (1998), Biogeochemical Controls and Feedbacks on Ocean Primary Production, *Science (80-.).*, *281*(5374), 200–206, doi:10.1126/science.281.5374.200.

Field, C. B. (1998), Primary Production of the Biosphere: Integrating Terrestrial and Oceanic Components, *Science (80-.).*, *281*(5374), 237–240, doi:10.1126/science.281.5374.237.

Freeland, H. J. (2007), A short history of Ocean Station Papa and Line P, *Prog. Oceanogr.*, *75*(2), 120–125, doi:10.1016/j.pocean.2007.08.005.

Gattuso, J.-P., and L. Hansson (Eds.) (2011), *Ocean Acidification*, Oxford University Press, Incorporated.

Giesbrecht, K. E., R. C. Hamme, and S. R. Emerson (2012), Biological productivity along Line P in the subarctic northeast Pacific: In situ versus incubation-based methods, *Global Biogeochem. Cycles*, *26*(3), n/a–n/a, doi:10.1029/2012GB004349.

Gruber, N., C. D. Keeling, and T. F. Stocker (1998), Carbon-13 constraints on the seasonal inorganic carbon budget at the BATS site in the northwestern Sargasso Sea, *Deep Sea Res. Part I Oceanogr. Res. Pap.*, *45*(4-5), 673–717, doi:10.1016/S0967-0637(97)00098-8.

Gruber, N. et al. (2009), Oceanic sources, sinks, and transport of atmospheric CO_2, *Global Biogeochem. Cycles*, *23*(1), 1–21, doi:10.1029/2008GB003349.

Van Heuven, S. M. A. C., D. Pierrot, J. W. B. Rae, E. Lewis, and D. W. R. Wallace (2011), MATLAB Program Developed for CO_2 System Calculations, *ORNL/CDIAC-105b. Carbon Dioxide Inf. Anal. Center, Oak Ridge Natl. Lab. U.S. Dep. Energy, Oak Ridge, Tennessee*.

Available from: http://cdiac.ornl.gov/ftp/co2sys/CO2SYS_calc_MATLAB_v1.1/ (Accessed 2 July 2014)

Houghton, R. A. (2007), Balancing the Global Carbon Budget, *Annu. Rev. Earth Planet. Sci.*, *35*(1), 313–347, doi:10.1146/annurev.earth.35.031306.140057.

Keeling, C. D., H. Brix, and N. Gruber (2004), Seasonal and long-term dynamics of the upper ocean carbon cycle at Station ALOHA near Hawaii, *Global Biogeochem. Cycles*, *18*(4), doi:10.1029/2004GB002227.

Lin, P., F. Chai, H. Xue, and P. Xiu (2014), Modulation of decadal oscillation on surface chlorophyll in the Kuroshio Extension, *J. Geophys. Res. Ocean.*, *119*(1), 187–199, doi:10.1002/2013JC009359.

Lockwood, D. (2013), Impact of the marine biological pump on atmospheric CO_2 uptake in the North Pacific: a study based on basin-wide underway measurements of oxygen/argon gas ratios and pO_2, University of Washington.

Lockwood, D., P. D. Quay, M. T. Kavanaugh, L. W. Juranek, and R. A. Feely (2012), High-resolution estimates of net community production and air-sea CO_2 flux in the northeast Pacific, *Global Biogeochem. Cycles*, *26*(4), n/a–n/a, doi:10.1029/2012GB004380.

Lyman, J. M., S. A. Good, V. V Gouretski, M. Ishii, G. C. Johnson, M. D. Palmer, D. M. Smith, and J. K. Willis (2010), Robust warming of the global upper ocean., *Nature*, *465*(7296), 334–7, doi:10.1038/nature09043.

Millero, F. J. (2007), The marine inorganic carbon cycle., *Chem. Rev.*, *107*, 308–341, doi:10.1021/cr0503557.

Orr, J. C. et al. (2005), Anthropogenic ocean acidification over the twenty-first century and its impact on calcifying organisms., *Nature*, *437*(7059), 681–6, doi:10.1038/nature04095.

Passow, U., and C. A. Carlson (2012), The biological pump in a high CO_2 world, *Mar. Ecol. Prog. Ser.*, *470*(2), 249–271, doi:10.3354/meps09985.

Quay, P. D., and J. Stutsman (2003), Surface layer carbon budget for the subtropical N. Pacific: constraints at station ALOHA, *Deep Sea Res. Part I Oceanogr. Res. Pap.*, *50*(9), 1045–1061, doi:10.1016/S0967-0637(03)00116-X.

Le Quéré, C. et al. (2009), Trends in the sources and sinks of carbon dioxide, *Nat. Geosci.*, *2*(12), 831–836, doi:10.1038/ngeo689.

Le Quéré, C. et al. (2014), Global carbon budget 2013, *Earth Syst. Sci. Data*, *6*(1), 235–263, doi:10.5194/essd-6-235-2014.

Rhein, M. et al. (2013), Observations: Ocean, in *Climate Change 2013: The Physical Science Basis. Contribution of Working Group I to the Fifth Assessment Report of the Intergovernmental Panel on Climate Change*, edited by V. B. and P. M. M. Stocker, T.F., D. Qin, G.-K. Plattner, M. Tignor, S.K. Allen, J. Boschung, A. Nauels, Y. Xia, Cambridge University Press, Cambridge, United Kingdom and New York, NY, USA.

Sabine, C. L. et al. (2004), The oceanic sink for anthropogenic CO_2, *Science*, *305*(5682), 367–71, doi:10.1126/science.1097403.

Sarmiento, J. L., and N. Gruber (2006a), Carbon Cycle, in *Ocean Biogeochemical Dynamics*, pp. 318–355, Princeton University Press, New Jersey.

Sarmiento, J. L., and N. Gruber (2006b), Organic Matter Production, in *Ocean Biogeochemical Dynamics*, Princeton University Press, New Jersey.

Sigman, D. M., and E. A. Boyle (2000), Glacial/interglacial variations in atmospheric carbon dioxide, *Nature*, *407*(6806), 859–869.

Signorini, S. R., C. R. McClain, J. R. Christian, and C. Wong (2001), Seasonal and interannual variability of phytoplankton, nutrients, TCO_2 , pCO_2 , and O_2 in the eastern subarctic Pacific (ocean weather station Papa), *J. Geophys. Res.*, *106*(C12), 31197–31215, doi:10.1029/2000JC000343.

Sugiura, K., and S. Tsunogai (2005), Spatial and temporal variation of surface xCO_2 providing net biological productivities in the western North Pacific in June, *J. Oceanogr.*, *61*.

Sutton, A. J. et al. (2014), A high-frequency atmospheric and seawater pCO_2 data set from 14 open ocean sites using a moored autonomous system, *Earth Syst. Sci. Data Discuss.*, *7*, 385–418, doi:10.5194/essdd-7-385-2014.

Takahashi, T., J. G. Goddard, and D. W. Chipman (1993), Seasonal Variation of CO_2 and Nutrients in the High-Latitude surface oceans: acomparative study, *Global Biogeochem. Cycles*, *7*(4), 843–878.

Takahashi, T., S. C. Sutherland, C. Sweeney, A. Poisson, N. Metzl, B. Tilbrook, N. R. Bates, R. Wanninkhof, R. A. Feely, and C. L. Sabine (2002), Global sea–air CO_2 flux based on climatological surface ocean pCO_2, and seasonal biological and temperature effects, *Deep Sea Res. Part II Top. Stud. Oceanogr.*, *49*(9-10), 1601–1622, doi:10.1016/S0967-0645(02)00003-6.

Takahashi, T., S. C. Sutherland, R. A. Feely, and R. Wanninkhof (2006), Decadal change of the surface water pCO_2 in the North Pacific: A synthesis of 35 years of observations, *J. Geophys. Res.*, *111*(C7), 1–20, doi:10.1029/2005JC003074.

Takahashi, T. et al. (2009), Climatological mean and decadal change in surface ocean pCO_2, and net sea–air CO_2 flux over the global oceans, *Deep Sea Res. Part II Top. Stud. Oceanogr.*, *56*(8-10), 554–577, doi:10.1016/j.dsr2.2008.12.009.

Wong, C., F. A. Whitney, K. Iseki, J. S. C. Page, and J. Zeng (1995), Analysis of trends in primary productivity and chlorophyll-a over two decades at Ocean Station P (50 N, 145 W) in the subarctic Northeast Pacific Ocean, *Can. Spec. Publ. Fish. Aquat. Sci.*, *121*, 107–117.

Wong, C., N. A. D. Waser, Y. Nojiri, W. K. Johnson, F. A. Whitney, J. S. C. Page, and J. Zeng (2002a), Seasonal and interannual variability in the distribution of surface nutrients and dissolved inorganic carbon in the Northern North Pacific: influence of El Niño, *J. Oceanogr.*, *58*(2), 227–243.

Wong, C., N. A. D. Waser, Y. Nojiri, F. A. Whitney, J. S. C. Page, and J. Zeng (2002b), Seasonal cycles of nutrients and dissolved inorganic carbon at high and mid latitudes in the North Pacific Ocean during the Skaugran cruises: determination of new production and nutrient uptake ratios, *Deep Sea Res. Part II Top. Stud. Oceanogr.*, *49*(24-25), 5317–5338, doi:10.1016/S0967-0645(02)00193-5.

Wong, C., N. A. D. Waser, F. A. Whitney, W. Johnson, and J. S. C. Page (2002c), Time-series study of the biogeochemistry of the North East subarctic Pacific: reconciliation of the Corg/N remineralization and uptake ratios with the Redfield ratios, *Deep Sea Res. Part II Top. Stud. Oceanogr.*, *49*(24-25), 5717–5738, doi:10.1016/S0967-0645(02)00211-4.

Yasunaka, S., Y. Nojiri, S. Nakaoka, T. Ono, H. Mukai, and N. Usui (2013), Monthly maps of sea surface dissolved inorganic carbon in the North Pacific: Basin-wide distribution and seasonal variation, *J. Geophys. Res. Ocean.*, *118*(8), 3843–3850, doi:10.1002/jgrc.20279.

Yasunaka, S., Y. Nojiri, S. Nakaoka, T. Ono, F. A. Whitney, and M. Telszewski (2014), Mapping of sea surface nutrients in the North Pacific: Basin-wide distribution and seasonal to interannual variability, *J. Geophys. Res. Ocean.*, n/a–n/a, doi:10.1002/2014JC010318.

Chapter 2

Net community production and calcification from seven years of NOAA Station Papa Mooring measurements

1. Background

The biological consumption and export of carbon from the ocean surface to the abyssal sediments, commonly referred to as the biological pump, is a major pathway for long-term carbon sequestration from the atmosphere [*Passow and Carlson*, 2012; *Ciais et al.*, 2013]. Approximately 11 Pg C yr^{-1} is exported from the surface ocean to the ocean interior as sinking organic and inorganic carbon particles are degraded in the water column [*Ciais et al.*, 2013] and 0.2 Pg C is delivered to the sediments annually by the biological pump. This biologically mediated carbon transport, in addition to other physical processes, gives rise to a vertical carbon gradient in the ocean and enables the ocean to hold ~50 times more carbon than the atmosphere [*Rhein et al.*, 2013]. If the vertical carbon gradient were to change due circulation changes or alterations in the biological pump, the efficiency of anthropogenic carbon dioxide (CO_2) uptake by the ocean could be affected through complex feedback mechanisms on societally relevant timescales [*Passow and Carlson*, 2012]. These feedback mechanisms have been discussed in the literature, but are not well understood due to the complexity of ecosystem interactions and uncertain biogeochemical responses to anthropogenic ocean warming and acidification. In order to identify changes in the efficiency of the biological pump, and quantitatively assess the climate implications on carbon cycling, a well constrained marine carbon cycle budget is needed.

Significant effort has been made to better understand marine carbon cycling. These efforts include observations from time-series sites, such as Bermuda Atlantic Time Series (BATS; *Bates*, 2012; *Lomas et al.*, 2013), European Station for Time-series in the Ocean (ESTOC; *González-Dávila et al.*, 2010), Hawaii Ocean Time-series (HOT; *Winn et al.*, 1998; *Brix et al.*, 2004; *Dore et al.*, 2009), Ocean Station Papa (OSP; *Wong et al.*, 2002c; *Timothy et al.*, 2013), and Carbon Retention in a Colored Ocean (CARIACO; *Taylor et al.*, 2012; *Astor et al.*, 2013). Long-term observations from these stations integrate over natural oscillations and stochastic variability to reveal multi-decadal trends as well as seasonal patterns of marine carbon cycling [*Bates et al.*, 2014]. Many of the longest and most robust observational time-series come from ship based work where sites are sampled at least 4 times per year. At these sites, globally consistent trends are emerging with regard to surface ocean carbonate chemistry, showing that modern ocean CO_2 uptake and pH changes have been primarily controlled by CO_2 solubility [*Bates et al.*, 2014; *Lauvset et al.*, 2014]. There are, however, a few outliers, indicating that the CO_2 trends in some regions cannot be explained solely by the atmospheric CO_2 increase and that physical and/or biogeochemical processes may now be influencing marine carbon cycling in these locations[14].

Moorings have become useful tools for studying complex and episodic processes that require continuous observations to unravel. With the ability to resolve both long-term trends and intermittent events, time-series studies on moorings can be used to learn about carbon cycling in remote locations and to develop modern, regional baselines for the biological pump [*McGillicuddy et al.*, 1998, 2007; *Wong et al.*, 1999; *Hamme et al.*, 2010]. High temporal resolution CO_2 observations from moorings have proven extremely useful in identifying stochastic biological events that may have been misinterpreted in a lower-frequency dataset [*Hamme et al.*, 2010]. This

type of event scale resolution is more important than ever when analyzing datasets for climate signals, which can be obscured by sample frequency biasing [*Bates et al.*, 2014]. In addition to the immediate utility of using biogeochemical mooring data to study carbon cycling, these platforms are useful for calibrating sensors on autonomous floats and gliders and may assist the development and training of satellite products for carbon cycle research [*Gledhill et al.*, 2009; *Johnson et al.*, 2009; *Hales et al.*, 2012].

Ocean Station Papa (OSP) is a time-series site located at 50°N, 145°W in a region of high annual atmospheric CO_2 uptake in the subarctic northeast Pacific Ocean [*Takahashi et al.*, 2009; *Ayers and Lozier*, 2012]. OSP began as a weather ship station in 1956. In 1981 when the program concluded, the Canadian DFO Line P program continued to make repeat hydrographic cruises at least 2-3 times per year through the present date [*Freeland*, 2007]. From this rich hydrographic data set, net community production (NCP), defined as the gross photosynthetic production minus the community respiration in the surface mixed layer, has been estimated from ^{14}C bottle incubations [*Wong et al.*, 1995], seasonal carbon and nutrient draw down ratios [*Takahashi et al.*, 1993; *Wong et al.*, 2002a, 2002b], thorium and uranium isotopes [*Charette et al.*, 1999], oxygen mass-balances [*Emerson*, 1987; *Emerson et al.*, 1991; *Emerson and Stump*, 2010; *Giesbrecht et al.*, 2012; *Lockwood*, 2013], as well as one-dimensional model simulations [*Signorini et al.*, 2001; *Wong et al.*, 2002c]. The total NCP over a given year, commonly referred to as the annual net community production (aNCP), is an upper limit on biologically mediated carbon export from the ocean surface to the interior each year, integrating both the particulate and the dissolved organic carbon production, the latter of which may vary significant at this location [*Emerson et al.*, 1991; *Bishop et al.*, 1999; *Wong et al.*, 2002c; *Emerson*, 2014].

In June 2007, a NOAA surface mooring carrying physical and biogeochemical sensors was deployed at OSP beginning a high-frequency, *in situ* observational time-series that continues to the present date. Oxygen and total gas pressure measurements from the OSP mooring were used to determine NCP [*Emerson and Stump*, 2010] and calcium carbonate ($CaCO_3$) production [*Emerson et al.*, 2011] in 2007; however, due to complexities in using oxygen as a mixed-layer tracer during winter, these estimates were confined to the summer. Scaling seasonal NCP estimates to annual values requires making assumptions about the duration of the productive season and consistency of the NCP rate throughout the year [*Emerson and Stump*, 2010]. With moored time-series becoming a common component in long-term observing efforts, methods that can resolved the entire annual cycle of NCP *in situ* are needed to make use of these important and growing data sets [*Sutton et al.*, 2014].

Here we assess seasonal and interannual variability in NCP and $CaCO_3$ production at OSP from seven years of high-frequency moored observations using a dual tracer, mixed-layer carbon budget. Changes in mixed-layer dissolved inorganic carbon (DIC) and total alkalinity (TA) are used to diagnostically isolate physical, chemical, and biological carbon transformations and assess their annual contributions to surface ocean carbon inventory changes. The use of two mixed-layer carbon tracers allows us to isolate organic carbon production (NCP) from inorganic carbon production ($CaCO_3$). This work contributes to the quantitative development of a modern baseline for carbon cycling in this important ocean carbon sink region [*Takahashi et al.*, 2006; *Takahashi*, 2009; *Ayers and Lozier*, 2012].

2. Data

2.1.Mooring Data

The NOAA Station Papa mooring, deployed in June 2007 at 50°N, 145°W, contributes to the global network of OceanSITES time series reference stations [*Send*, 2010]. The mooring carries a suite of meteorological, physical and biogeochemical sensors to monitor the air-sea exchanges of heat, moisture, momentum, and carbon dioxide. It is also designed to monitor ocean acidification and upper ocean temperature, salinity, oxygen and near surface currents. In particular, the buoy houses two inorganic carbon sensors used in this analysis: a Sunburst Sami-2 unit that measures sea surface pH and a Battelle Memorial Institute MapCO_2 system that monitors the mole fraction of carbon dioxide (xCO_2) in seawater and in the atmospheric boundary layer. As discussed later in Sections 3.1.1, 3.1.2 and 3.2, these measurements are used to calculate DIC and to estimate the air-sea CO_2 flux.

The analysis method described in the next section relies upon computing the sources and sinks of carbon inventory within the mixed layer. Mixed layer depth is computed from the mooring density profile measurements; mixed-layer velocity, used to estimate horizontal advection, is based upon the current meter data at 5 m, 15m, and 35 m, and a nearby upward looking Acoustic Doppler Current Profiler when available. Diffusivity at the base of the mixed layer was estimated by closing the mixed-layer heat budget following *Cronin et al.*, (2013). The carbon budget, thus, relies upon nearly every measurement made on the mooring. Details about the specific sensors and their orientations during each deployment can be found on the Ocean Climate Stations web page (*http://www.pmel.noaa.gov/OCS/Papa/*).

Sensors on the mooring have operated almost continuously from 2007 to 2014 (**Figure 1**). The mooring and all sensors are recovered and a fresh system is redeployed every year, typically in June. In fall of 2008, the mooring broke free resulting in a large data gap from November 2008 to June 2009. Smaller periods of missing data in the xCO_2 observation time-series in 2010, 2012, and 2013 were caused by sensor or battery failure. Due to the numerous sensors on the mooring, each programmed to sample at different frequencies, all data have been daily averaged and centered on 12:00 Greenwich Mean Time for this analysis.

2.2.Repeat Hydrography Data

Repeat hydrography cruise data that are publicly available from the Carbon Dioxide Information Analysis Center have been incorporated into the analysis for the development of relationships between carbonate system parameters (DIC and TA) and other commonly measured variables. Details about the use of these data are presented in Sections 3.1.1 and 3.3. The specific cruise data used in this analysis include CLIVAR Line P16 North in 2006 and in 2008, CLIVAR Line P01in 2007, and all Line P cruises between 1994 and 2010 (**Figure 2,** *Fukasawa et al.*, 2007; *Feely et al.*, 2008, 2011; *Miller et al.*, 2010). In addition, one degree optimally interpolated data fields from the 2013 World Ocean Atlas are used herein and discussed in Section 3.3 [*Garcia et al.*, 2013a, 2013b; *Locarnini et al.*, 2013; *Zweng et al.*, 2013].

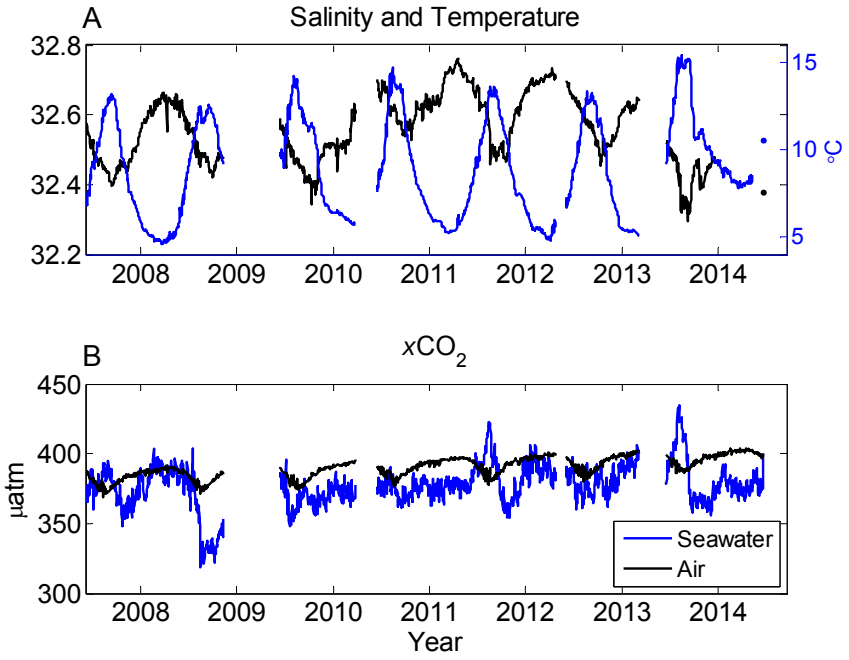

Figure 1: Time-series of sea surface (**A**) salinity, temperature, (**B**) xCO_2, and atmospheric boundary layer xCO_2 at Ocean Station Papa.

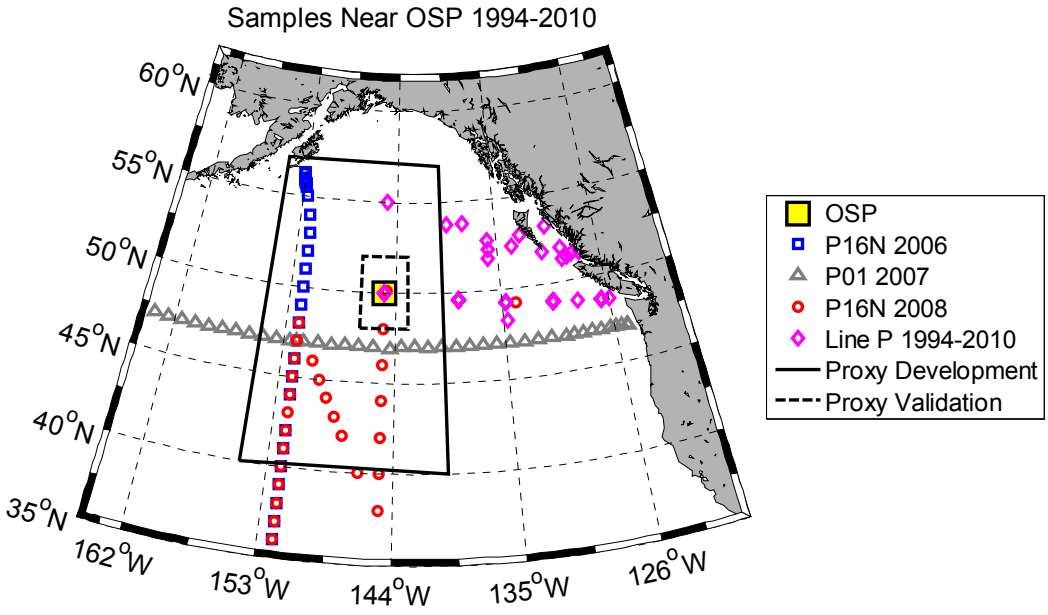

Figure 2: Map showing Ocean Station Papa (50°N, 145°W), nearby station locations from three CLIVAR repeat hydrography cruises between 2006 and 2008, and stations from numerous Line P cruises between 1994 and 2010. The large solid black box encompasses the stations used to develop a regional TA proxy. The dashed black box encompasses the stations used to validate the TA proxy performance near the Ocean Station Papa mooring.

2.3.Satellite Data

There are very few time periods when xCO_2 measurements are available and other sensor data are not. A two week data gap in anemometer wind speed measurements in 2008 was filled using 0.25 degree, 6 hourly, cross-calibrated multi-platform ocean surface winds from NASA [*Atlas et al.*, 2011]. During periods when ADCP and current meter data are not available, 1/3 degree, 5 day OSCAR satellite surface currents are used [*Bonjean and Lagerloef*, 2002]. Vertical velocity was estimated from the wind stress curl, assuming Ekman physics, using the daily ASCAT wind stress data set [*Bentamy and Fillon*, 2012].

3. Methods

Dissolved inorganic carbon (DIC) refers to the sum of the concentrations of carbonic acid (H_2CO_3), bicarbonate ion (HCO_3^-), carbonate ion (CO_3^{2-}), and carbon dioxide (CO_2) in aqueous solution:

$$DIC = [CO_2] + [H_2CO_3] + [HCO_3^-] + [CO_3^{2-}] \quad (\mathbf{1})$$

DIC is influenced by all carbon transformations in the mixed layer including air-sea gas exchange (Gas), physical transport and mixing (Phys), concentration effects caused by evaporation and precipitation (EP), and the biological processes of organic (NCP) and inorganic ($CaCO_3$) carbon production:

$$\frac{\partial DIC}{\partial t} = \left.\frac{\partial DIC}{\partial t}\right|_{Gas} + \left.\frac{\partial DIC}{\partial t}\right|_{Phys} + \left.\frac{\partial DIC}{\partial t}\right|_{EP} + \left.\frac{\partial DIC}{\partial t}\right|_{NCP} + \left.\frac{\partial DIC}{\partial t}\right|_{CaCO_3} \quad (\mathbf{2})$$

In situ observations from the NOAA Station Papa mooring can be used to estimate the term on the left hand side and the first three terms on the right hand side (i.e., gas exchange, physical processes, and EP), leaving one equation and two unknowns. In order to close the budget a second mixed-layer tracer is required. Total alkalinity (TA) is the charge balance in seawater, defined as the excess of proton acceptors over proton donors [*Wolfgladrow et al.*, 2007]:

$$TA = [HCO_3^-] + 2*[CO_3^{2-}] + [B(OH)_4^-] + [HPO_4^{2-}] + 2*[HPO_4^{3-}]\ldots + [OH^-] - [H^+] \quad (\mathbf{3})$$

TA is influenced by all of the same processes as DIC excluding gas exchange because dissolution of CO_2 has no net influence on the TA charge balance:

$$\frac{\partial TA}{\partial t} = \left.\frac{\partial TA}{\partial t}\right|_{Phys} + \left.\frac{\partial TA}{\partial t}\right|_{EP} + \left.\frac{\partial TA}{\partial t}\right|_{NCP} + \left.\frac{\partial TA}{\partial t}\right|_{CaCO_3} \quad (\mathbf{4})$$

DIC and TA are stoichiometrically related during the biological processes of photosynthesis and respiration (NCP) as well as calcium carbonate dissolution and precipitation ($CaCO_3$). The time-dependent DIC and TA mass-balances can therefore be rearranged to give two equations and two unknowns, making it possible to close the mixed-layer budgets.

Similar diagnostic carbon budget assessments have been made using ship based data [*Gruber et al.*, 1998; *Quay and Stutsman*, 2003; *Brix et al.*, 2004; *Keeling et al.*, 2004], and more recently using moored CO_2 time-series [*Sugiura and Tsunogai*, 2005; *Chierici et al.*, 2006; *Körtzinger et al.*, 2008]. Although autonomous DIC and TA sensors are not currently commercially available for extended duration deployments on moorings, CO_2 measurements at numerous moored time-

series locations [*Sutton et al.*, 2014] can be leveraged for more complex analyses and provide insights about biological carbon cycling until new sensors become available. Here we build off of the approaches of previous investigators and evaluate the drivers of seasonal and interannual DIC variability at Station Papa. This approach integrates physical and chemical moored time-series data along with observations from repeat hydrography cruises, the 2013 World Ocean Atlas gridded products, and satellites to evaluate annual net community production and calcium carbonate processes over a seven-year time period.

3.1. Creating a DIC Time-series

Evaluating changes in the carbon inventory of the surface mixed layer, and the processes responsible for those changes, requires a time-series of dissolved inorganic carbon (DIC). Without direct observations of mixed-layer DIC, alternative methods must be employed to reconstruct the carbon time-series. Any two measurable carbonate system parameters (DIC, TA, xCO_2, pH) can be used to calculate all other carbonate system parameters; therefore, contemporaneous *in situ* measurements of pH and xCO_2 at OSP were used to estimate DIC and TA with the program CO_2sys [*van Heuven et al.*, 2011] using constants from Lueker [*Lueker et al.*, 2000] and Dickson [*Dickson*, 1990]. Comparison of the calculated DIC and TA values with a limited number of high-quality discrete bottle samples collected near the mooring throughout the time-series (**Figure 2**) reveals unrealistic excursions and biases in the calculated DIC (e.g. differences >100 μmol kg^{-1}). Large errors in the calculated DIC and TA are the result of pH and/or xCO_2 measurement inaccuracies that significantly influence the calculations of other carbonate system parameters due to the strong covariance between the pH-xCO_2 pair. This concept has been well documented in the literature [*Dickson and Riley*, 1978; *Millero*, 2007] and has recently been revisited with regards to

autonomous marine carbonate sensors [*Cullison Gray et al.*, 2011; *Fassbender et al.*, 2014]. Due to the challenges in using the xCO_2-pH pair to calculated surface TA and DIC concentrations, an alternative method was developed.

3.1.1. Total Alkalinity Proxy

To reconstruct sea surface DIC and TA time-series at OSP a regional proxy for TA based on salinity (TA = 37 × salinity + 988) was developed. The proxy was developed using discrete TA and salinity samples from repeat hydrography cruises within the Alaska Gyre region between 1994 and 2010 (**Figure 2** large black box). Average mixed-layer TA and salinity values were computed at each station using a mixed layer depth criterion of a 0.03 kg m^{-3} density increase from the density at 10m depth [*de Boyer Montégut*, 2004]. The relationship was based on 68 distinct mixed-layer TA and salinity values yielding a statistically significant regression with an R^2 value of 0.74 (**Figure 3**). The regional TA proxy was applied to *in situ* salinity measurements from the OSP time-series yielding estimates of sea surface TA for the seven years of moored observations (**Figure 4A**). The 1σ calculation uncertainty for the TA values is ~3 μmol kg^{-1}. Discrete TA bottle samples collected in close proximity to the OSP mooring (**Figure 2** small dashed black box) between 2007 and 2012 show good agreement with the magnitude and seasonality of the predicted TA values. The mean difference between TA bottle samples and the salinity-derived TA values is 0 μmol kg^{-1}.

3.1.2 Calculating DIC

The salinity-derived TA values were paired with *in situ* measurements of xCO_2 and pH to calculate two DIC time-series using the program CO_2sys [*van Heuven et al.*, 2011] with constants

from Lueker [*Lueker et al.*, 2000] and Dickson [*Dickson*, 1990] (**Figure 4b).** While both xCO_2 and pH perform well at predicting DIC when paired with TA, the xCO_2 time-series has fewer data gaps and shows less sensor noise. Discrete DIC bottle samples collected between 2007 and 2012 during repeat hydrographic cruises near OSP agree well with the DIC values computed from the TA-xCO_2 pair (mean difference of 2 µmol kg^{-1}). The good agreement suggests that our TA proxy and DIC estimates are robust; therefore, DIC values derived from the TA-xCO_2 pair are used for the remainder of the analysis. The 1σ calculation uncertainty for DIC values derived from the TA-xCO_2 pair is ~3 µmol kg^{-1}.

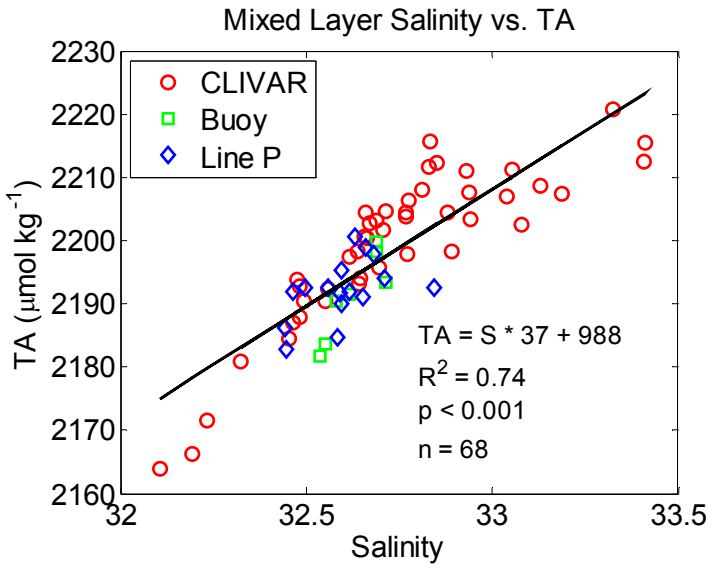

Figure 3: Mixed-layer salinity versus total alkalinity relationship derived from samples collected inside the solid lined black box in Figure 2. The symbols represent bottle sample data collected during CLIVAR and Line P cruises as well as next to the buoy during deployments.

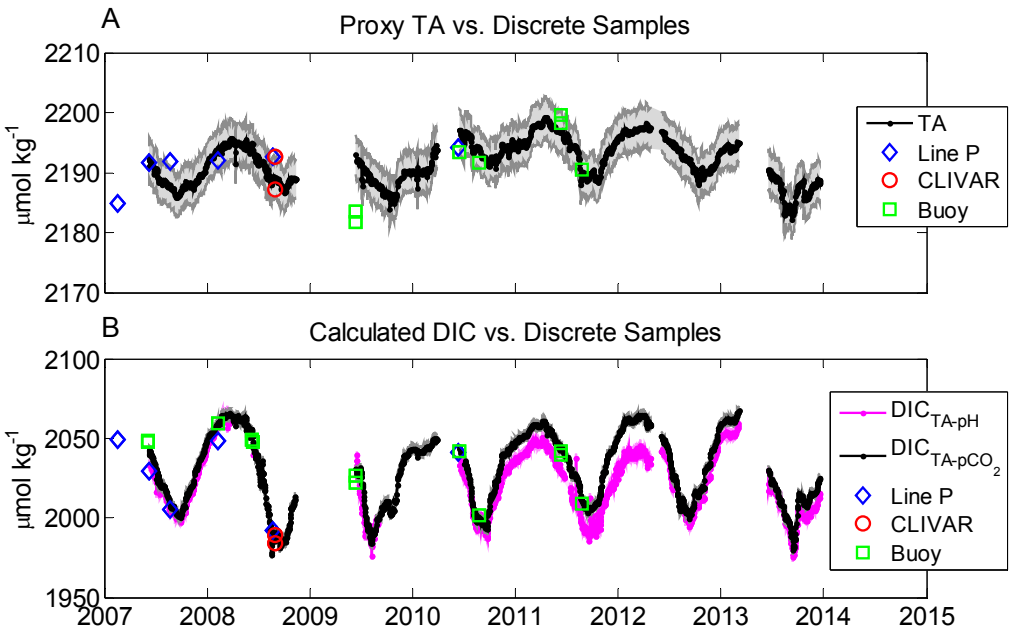

Figure 4: (**A**) TA estimates from the salinity-based proxy and (**B**) DIC values computed from the TA-pH and TA-pCO_2 pairs using the program CO_2sys. 68% uncertainty bounds are shaded. Discrete TA and DIC bottle samples collected within the dashed black box region in Figure 2 between 2007 and 2012 are shown for comparison.

3.2 Gas Exchange

Air-sea CO_2 gas exchange is estimated daily from wind speed and the difference in CO_2 partial pressure (pCO_2) between the sea surface and atmosphere (ΔpCO_2):

$$\Delta pCO_2 = pCO_{2,\,sea} - pCO_{2,\,atm} \quad (5)$$

Where CO_2 partial pressure is the product of total pressure (P) and xCO_2. Winds measured at 4m on the NOAA Station P buoy are converted to 10m winds using the relationship of *Liu et al.* (1979) and are used to compute the CO_2 piston velocity (k) with the Schmidt number relationship of *Wanninkhof*, (1992) and gas transfer parameterization of *Nightingale et al.*, (2000). The

temperature and salinity dependent CO_2 solubility constant (C) of *Weiss*, (1974) is used with the piston velocity (k) and ΔpCO_2 to compute daily air-sea CO_2 fluxes in units of mol CO_2 m^{-2} d^{-1}:

$$\left.\frac{\partial DIC}{\partial t}\right|_{Gas} = F_{t=n} = k_{t=n} \times C_{t=n} \times (\Delta pCO_{2,\,t=n}) \times 10^{-6} \quad (\mathbf{6})$$

The flux is divided by mixed layer depth and density and is multiplied by 10^6 to convert to units of μmol DIC kg^{-1} d^{-1}.

3.3 Physical Processes

Physical processes affecting the rate of change in the mixed-layer DIC and TA mass balance include the influence of advection, entrainment (and detrainment), and diffusive mixing, expressed here in terms of DIC, is:

$$\frac{\partial DIC_{Phys}}{\partial t} = -u_a \cdot \nabla DIC_a - \left(w_{-h} + \frac{\partial h}{\partial t}\right)\frac{(DIC_a - DIC_{-h})}{h} - \frac{\kappa}{h}\left.\frac{\partial DIC}{\partial z}\right|_{z=-h} \quad (\mathbf{7})$$

Where u_a and DIC_a are the vertically averaged horizontal velocity and DIC concentration within the mixed layer, and h is the mixed layer depth (**Figure 5A**). Likewise, w_{-h}, DIC_{-h}, κ, and $\partial DIC\ \partial z^{-1}$ are the vertical velocity, DIC concentration, diffusivity, and vertical concentration gradient, respectively, all evaluated at the base of the mixed layer (z=-h). The mixed layer depth is computed as the depth where density increases by 0.03 kg m^{-3} from the 10 m density [*de Boyer Montégut*, 2004].

The first term on the right hand side of (**7**) accounts for horizontal advection of DIC into and out of the OSP region. The second term accounts for entrainment and detrainment vertical velocities (**Figure 5B**) acting on DIC gradients within the mixed layer. It should be noted that if the upwelling velocity (w_{-h}) is equal and opposite sign of the mixed layer depth change ($\partial h\ \partial t^{-1}$), this term will be zero. Likewise, if the DIC concentration is vertically uniform from the surface through the base of the mixed layer, then this term would also be zero. The third term accounts for diffusive turbulent mixing at the base of the mixed layer. A monthly climatology of diffusivity (κ) was determined from the climatological heat flux out the base of the mixed layer based on a June 2007-June 2013 mixed-layer heat budget analysis (Meghan Cronin, personal communication; **Appendix A**; **Figure 5C**). Periods when the residual heat flux was positive (i.e. warming the mixed layer) were excluded, except during convective periods when the ocean was losing heat to the atmosphere, if the upward heat flux at the base of the mixed layer did not exceed the surface upward heat flux. These upward heat fluxes at the base of the mixed layer are consistent with non-local source of turbulence [*Large et al.*, 1994], and appear to occur occasionally during winter at OSP. During late winter and early spring, the mixed layer was often shallower than the isothermal layer, and acted as a "barrier layer" to diffusive mixing of heat. In these cases, the residual heat flux at the base of the mixed layer is very small and dominated by errors. Thus, periods when barrier layers were larger than 15m were excluded from the climatology.

In fall of 2008, before the mooring broke free in November, failure of subsurface conductivity-temperature-depth sensors made it challenging to compute the mixed layer depth with confidence. Estimates of mixed layer depth from an autonomous profiling glider that was sampling around the

mooring during this time were used to fill in the gaps in the mooring estimate (Noel Pelland, personal communication; **Figure 5A**).

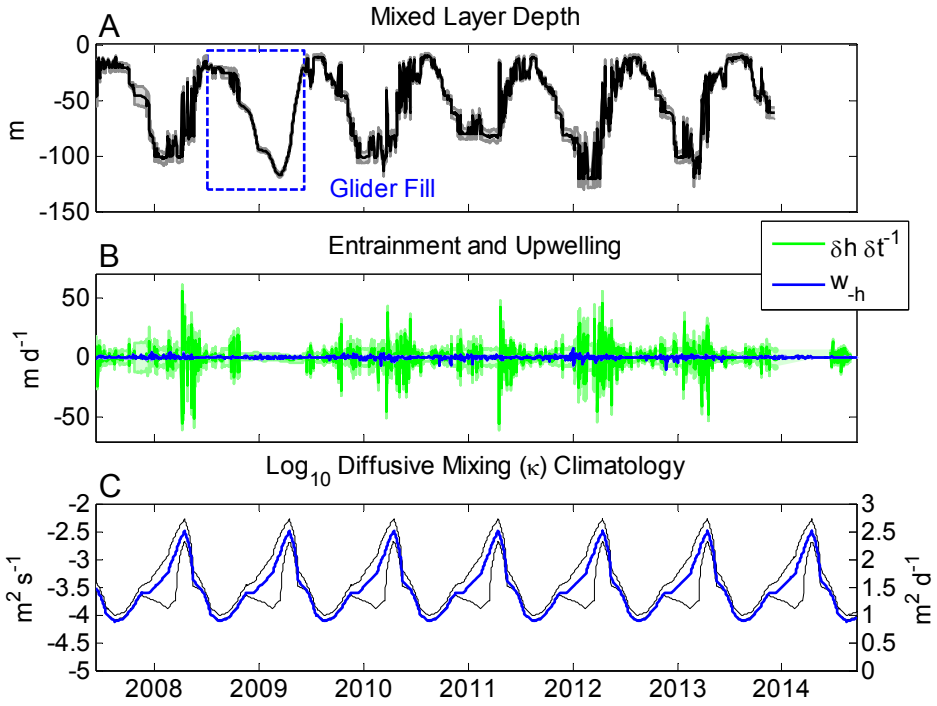

Figure 5. (**A**) Mixed layer depth time-series with error estimates shaded. The dashed blue box highlights when glider mixed layer depth estimates were used. (**B**) Ekman upwelling at the base of the mixed layer (w_{-h}) derived from wind stress curl (blue) and changes in the mixed layer depth with time ($\partial h\ \partial t^{-1}$; green), with error estimates shaded. (**C**) Time-series of diffusivity (κ), based on the monthly climatology, with error estimates.

As with the gas exchange rate, each term in (**7**) is evaluated daily. Continuous seasonal observations of horizontal and vertical DIC and TA gradients near OSP, however, do not exist, although high-quality carbon data have been collected near the mooring during repeat hydrography cruises that occurred just before or during the moored time-series. Data from these cruises were used to construct robust multiple linear regression (MLR) relationships between DIC (and TA) and measured predictor variables in both the meridional and zonal directions. The meridional MLR was developed using data from the CLIVAR Line P16 North 2006 cruise and the zonal MLR was developed using data from the CLIVAR Line P01 2007 cruise. Minimum latitude, longitude, and

depth ranges included in the MLRs were determined from maximum monthly averaged horizontal and vertical flow velocities at OSP. For the meridional regressions, oxygen and temperature were the predictor variables for DIC and silicate was the predictor variable for TA. For the zonal regressions, phosphate was the predictor variable for DIC and pressure and silicate were the predictor variables for TA. MLR regression coefficients from the meridional and zonal fits were then applied to 2013 World Ocean Atlas (WOA) monthly climatologies of the predictor variables to produce monthly DIC and TA fields. From the predicted DIC and TA fields, average mixed-layer concentrations were determined at each 2013 WOA grid location and horizontal gradients were computed in the meridional and zonal directions. Vertical concentration gradients were calculated using the meridional TA and DIC fields at WOA grids 49.5ºN, 50.5ºN, and 51.5ºN and then averaged (**Figure 6A**). The monthly gradient climatologies were linearly interpolated to daily climatologies and vertical gradients were set to zero on days when the mixed layer depth shoaled ($\partial h\, \partial t^{-1}<0$).

3.4 Evaporation-Precipitation

The influence of evaporation and precipitation (EP) on mixed-layer DIC and TA concentrations was determined using a mixed-layer salinity mass-balance where changes in salinity over time are caused by physical processes within the water column and EP. Monthly climatologies of salinity from the 2013 World Ocean Atlas were used to determine vertical and horizontal salinity gradients (**Figure 6B**) and estimate the physical component of the salinity budget:

$$\left.\frac{\partial Sal}{\partial t}\right|_{EP} = \left.\frac{\partial Sal}{\partial t}\right| - \left.\frac{\partial Sal}{\partial t}\right|_{Phys} \quad (\mathbf{8})$$

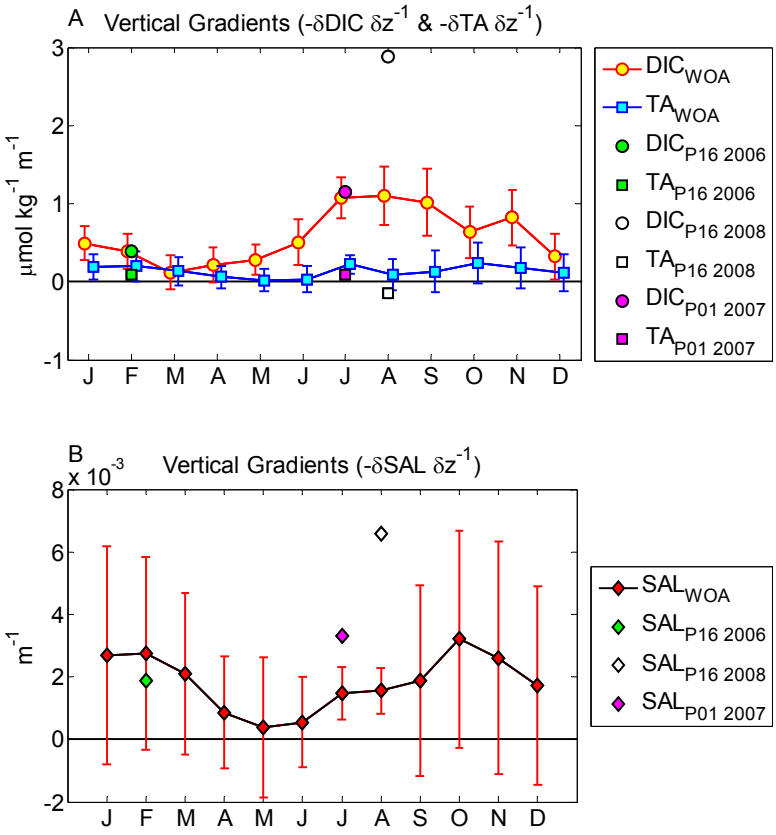

Figure 6: Monthly climatology of vertical (**A**) DIC, TA and (**B**) salinity gradients at the base of the mixed layer. Climatology values are slightly offset in each month for easier viewing. Vertical gradients observed during three CLIVAR cruises near OSP are shown for comparison.

Subtracting the physical component of the budget from the observed changes leaves the EP term. The EP term is multiplied by the DIC:salinity (and TA:salinity) ratio at the start of each deployment (*t=1*) to scale to units of μmol kg^{-1} d^{-1}:

$$\left.\frac{\partial DIC}{\partial t}\right|_{EP} = \left.\frac{\partial Sal}{\partial t}\right|_{EP} \times \left.\frac{DIC}{Sal}\right|_{t=1} \quad (9)$$

It should be noted that the TA:sainity ratio (~67.2) at the start of the deployment (t=1) is not the slope of the regional salinity-TA regression (37; **Figure 3**). The regional salinity-TA regression slope includes the influence of EP, biology, and mixing processes. The TA:sainity ratio at the start

of the deployment reflects the amount of TA and salt in the water at that time, and is equal to the slope of the dilution line relative to that starting point, making it possible to isolate the influence of EP on TA (and DIC).

3.5 NCP and $CaCO_3$ Processes

With estimates of gas exchange, mixing, and EP processes, this leaves only the biological terms (Bio), which can be estimated as a residual of the budget:

$$\left.\frac{\partial DIC}{\partial t}\right|_{Bio} = \left.\frac{\partial DIC}{\partial t}\right|_{NCP} + \left.\frac{\partial DIC}{\partial t}\right|_{CaCO_3} \quad \textbf{(10)}$$

$$\left.\frac{\partial TA}{\partial t}\right|_{Bio} = \left.\frac{\partial TA}{\partial t}\right|_{NCP} + \left.\frac{\partial TA}{\partial t}\right|_{CaCO_3} \quad \textbf{(11)}$$

NCP and calcium carbonate processes influence DIC and TA at well-known stoichiometric ratios. Production of one mole of $CaCO_3$ decreases the DIC concentration by one mole and the TA concentration by two moles. Similarly, organic matter production results in the consumption of one mole of phosphate (HPO_4^{2-}), 18 moles of H^+, and 117 moles of CO_2, causing TA to increase by 17 moles [*Anderson and Sarmiento*, 1994]. Therefore, the change in TA from organic matter production is equal to -17/117 times the change in DIC from organic matter production. These relationships make it possible to rearrange equations **10** and **11** to get two equations and two unknowns (not shown) and thus close the budget:

$$\left.\frac{\partial \mathrm{DIC}}{\partial \mathrm{t}}\right|_{\mathrm{NCP}} = \frac{\left(\left.\frac{\partial \mathrm{TA}}{\partial \mathrm{t}}\right|_{\mathrm{Bio}} - 2\times \left.\frac{\partial \mathrm{DIC}}{\partial \mathrm{t}}\right|_{\mathrm{Bio}}\right)}{\left(-2+\frac{-17}{117}\right)} \quad \textbf{(12)}$$

It should be noted that the residual also includes the accumulation of all errors in the budget. Therefore, a careful accounting of errors in the residual is performed. Manufacturer stated instrument errors were propagated through each of the calculations in this analysis using standard techniques. When computations were nonlinear or complex, a Montel Carlo approach was used in which 1,000 iterations of the computation were conducted while varying input parameters around their errors in a Gaussian manner (~3σ). The standard deviation of the 1,000 resultant values was then used as the error estimate for that parameter to be propagated in subsequent computations. Details about the error analysis, including information for variables that required data filling or more intensive error assessments, are described in **Appendix A**.

Parameterization of physical processes contributes most to uncertainties in the overall closing of the budget. Specifically, uncertainty in the vertical salinity, DIC and TA gradients at the base of the mixed layer (~19-100%; **Figure 6A, 6B**) coupled with uncertainties in the mixed layer depth (~5-13%) and turbulent diffusion (κ;~10-88%), give rise to 68% error bounds on the daily fluxes (μmol kg^{-1} d^{-1}) that are often larger than 100% (**Appendix A**). Cumulatively summing the daily fluxes over each annual deployment reduces these errors dramatically through the propagation of errors by summing in quadrature, leading to the 68% uncertainty bounds shown in **Figures 7** and **8**. Observations of the vertical salinity, DIC, TA and salinity gradients during hydrographic cruises near OSP (**Figure 6A, 6B**) give confidence to the sign, magnitude and seasonality of those computed herein, so we believe our uncertainty bounds are quite conservative.

4. Results

4.1. Mixed-Layer Budget Evaluations

The NOAA Station Papa Mooring is replaced in mid-June of each year, making June 19 a logical start date ($t=1$) for the annual mixed-layer budget evaluations. Changes in mixed-layer DIC and TA with time were computed by simply subtracting the concentration on June 19 from each time-series observation in the annual deployment, giving the total change at each time step in units of µmol kg^{-1}. Each of the other mixed-layer budget terms was computed in units of µmol kg^{-1} d^{-1}. These time dependent estimates were integrated from the start of the annual deployment through the duration of data collection in the respective year, giving a time series of cumulative mixed-layer DIC and TA changes for each process contribution in units of µmol kg^{-1} (**Figures 7A, 8A**).

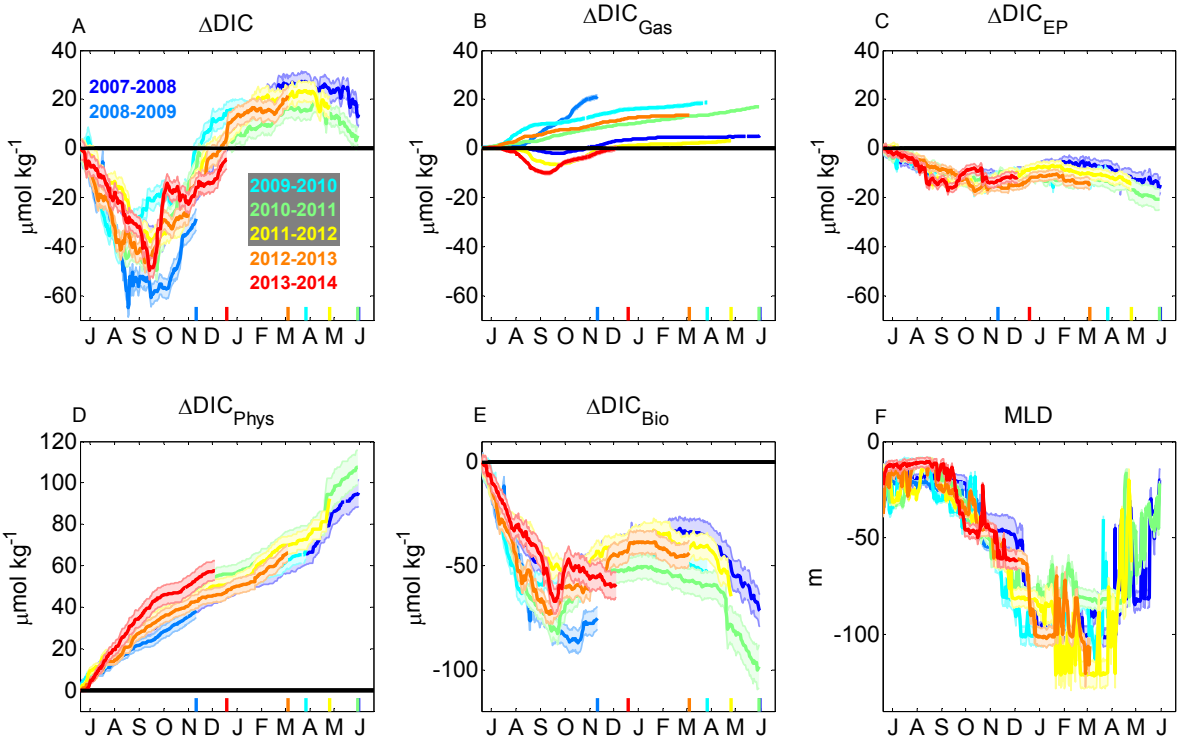

Figure 7: Results from the DIC budget analysis for individual deployment years (colors) with 68% uncertainty bounds. (**A**) Mixed-layer DIC concentration change relative to June 19 and the cumulative influences of (**B**) gas exchange, (**C**) EP, (**D**) physical processes, and (**E**) biological processes in units of µmol kg^{-1}. (**F**) Mixed layer depth. Colored lines at the bottom of each plot show the last day of observations from each mooring deployment.

Mixed-layer DIC and TA show a regular seasonal cycle of decreasing concentrations in spring and summer followed by increasing concentrations in fall and winter. The average peak-to-peak amplitude of the seasonal DIC cycle (~65 ± 3 μmol kg^{-1}) is about six times larger than that of TA (~10 ± 1 μmol kg^{-1}) and agrees with prior observations in the subarctic current system and Alaska Gyre [*Wong et al.*, 2002b]. The gas exchange contribution to mixed-layer DIC changes is variable for each year, with most years showing a net invasion of CO_2 and thus a net source of DIC to the mixed layer (~1 ± 9 μmol kg^{-1}; **Figure 7B)**. EP influences over the annual cycle act to dilute the DIC (~-18 ± 4 μmol kg^{-1}) and TA (~-19 ± 5 μmol kg^{-1}) concentrations due to net precipitation in this region (**Figures 7C, 8B)**. Higher precipitation in summer and fall combined with shallow mixed layer depths (**Figures 7F)** at this time leads to the maximum dilution occurring in fall for both parameters. Physical processes exert the dominant control on the DIC concentration, adding a significant amount of carbon to the mixed layer throughout the year (~101 ± 8 μmol kg^{-1}), primarily through diffusive mixing (~60%) and diapycnal entrainment (~40%) as horizontal advection is found to be negligible (**Figures 8C)**. For the TA budget, physical processes (~25 ± 1 μmol kg^{-1}) have a similar magnitude effect as the EP term, with diffusive mixing dominating the physical term (~60%) and entrainment (~40%) comprising the rest (**Figures 8C)**.

Summing the contributions of gas exchange, evaporation-precipitation, and physical processes and subtracting them from the observed changes in DIC and TA gives the residual biological component of the budgets (**Figures 7E, 8D)**. Biological processes remove DIC from the mixed layer over the course of the year, reducing the DIC concentration by ~85 ± 18 μmol kg^{-1}, which offsets much of the physical DIC input. Similarly, TA concentrations decline due to biological processes throughout the year, but at a much lower level (~-4 ±2 μmol kg^{-1}).

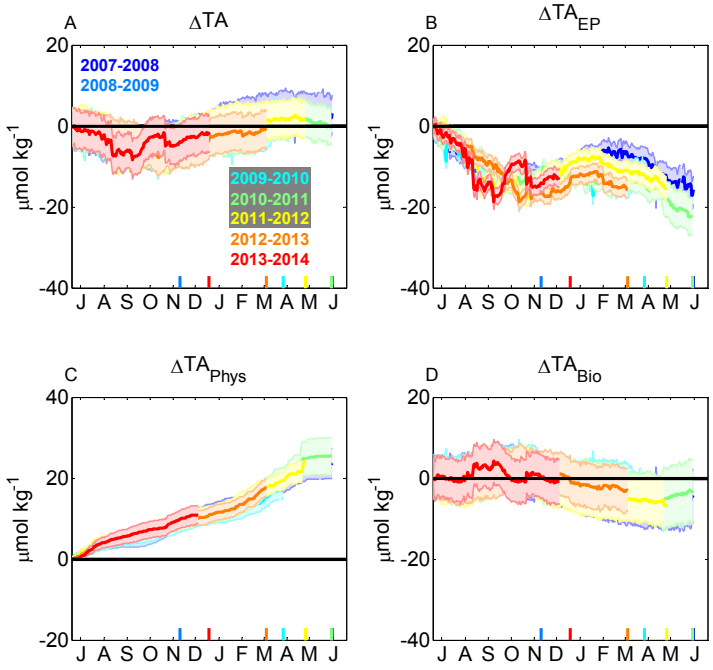

Figure 8: Results from the TA budget analysis for individual deployment years (colors) with 68% uncertainty bounds. (**A**) Mixed-layer TA concentration change relative to June 19 and the cumulative influences of (**B**) EP, (**C**) physical processes, and (**D**) biological processes in units of μmol kg^{-1}. Colored lines at the bottom of each plot show the last day of observations from each mooring deployment.

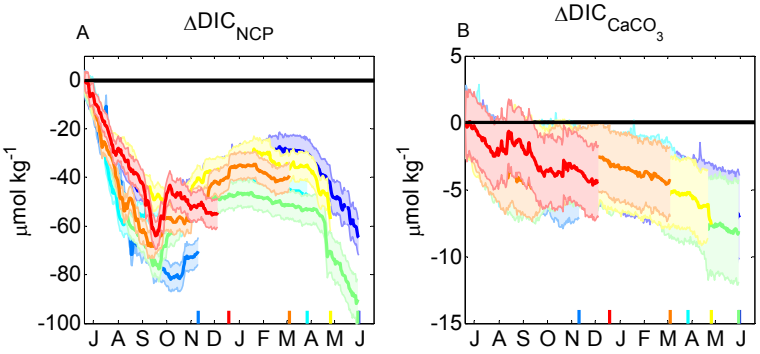

Figure 9: The cumulative influence of (**A**) NCP and (**B**) $CaCO_3$ process on the mixed-layer DIC concentrations. Colored lines at the bottom of each plot show the last day of observations in each annual mooring deployment.

4.2. NCP and $CaCO_3$

The biological DIC term was decomposed into NCP and $CaCO_3$ processes using equation **12** to close the budget and equation **10** to solve for DIC_{CaCO3} (**Figure 9**). The results show clear seasonality in the influence of organic carbon production on the mixed-layer DIC concentration. NCP causes mixed layer DIC concentrations to decline summer and spring and to increase in fall and winter. Observations over an entire annual cycle were captured during the 2007-2008 and 2010-2011 mooring deployments. During these two sampling periods, the annual net community production (aNCP) reduced mixed-layer DIC concentrations by 65 ± 8 and 90 ± 9 μmol DIC kg^{-1}, respectively. The influence of calcium carbonate production on the mixed-layer DIC concentration is much smaller than NCP and does not show a clear seasonal cycle. During the 2007-2008 and 2010-2011 mooring deployments, $CaCO_3$ production reduced mixed-layer DIC concentrations by 7 ± 3 and 8 ± 4 μmol DIC kg^{-1}, respectively.

4.3. Rates

Directly interpreting the DIC_{NCP} and DIC_{CaCO3} terms in units of concentration is not straight forward due to variability in the mixed layer depth throughout the year and between years. To address this we take the derivative of the DIC_{NCP} and DIC_{CaCO3} terms and multiply by the mixed layer depth, density, and 10^{-3} to convert to units of mmol C m^{-2} d^{-1}. The resulting values are the daily NCP and $CaCO_3$ rates (**Figure 10A-B**) which have been smoothed with a 30 day moving average to highlight seasonal variability. Negative NCP rates reflect net biological DIC consumption (autotrophy) and positive values reflect net biological DIC production (heterotrophy). Negative $CaCO_3$ production rates reflect net calcification while positive values indicate net dissolution. We integrate the daily rates (unsmoothed) and multiply by 10^{-3} to calculate

the cumulative column inventory of NCP and $CaCO_3$ in units of mol C m^{-2} (**Figure 10C-D**). Annual composites were created by averaging values from all available years at each time step, and are shown by the black lines in **Figures 10A-D** (mean monthly values for the integrated production composites and their uncertainties are given in **Appendix A**).

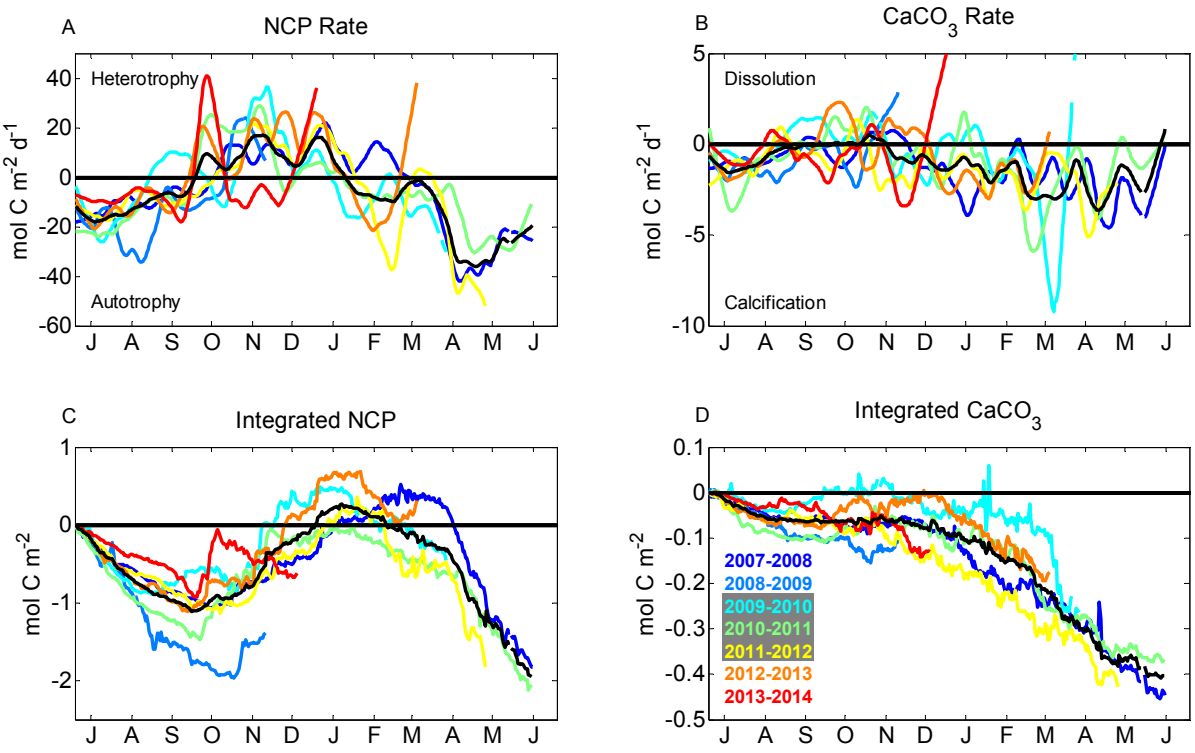

Figure 10. Daily (**A**) NCP and (**B**) $CaCO_3$ rates smoothed with a 30 day moving filter. Integrated (**B**) NCP and (**D**) $CaCO_3$. Black lines show the mean of all years.

The results show that OSP is a region of net annual autotrophy and calcification, as found by numerous prior investigators [*Wong et al.*, 2002c; *Lipsen et al.*, 2007; *Emerson and Stump*, 2010; *Emerson et al.*, 2011]. Autotrophic NCP rates begin around March and peak in April, with sustained production through September. After September, heterotrophy is observed until January of the subsequent year. $CaCO_3$ production is sustained through most of the year, with peak calcification rates in March and April and the lowest rates found in late summer and fall. A short

period of $CaCO_3$ dissolution appears during the late summer and fall; however, these values are not statistically significant. Cumulative summertime NCP results in ~1 mol C m^{-2} of production in the mixed layer from June to September (based on the composite), but this production is erased by the start of winter due to net respiration in the water column. Autotrophy resumes in spring, resulting in a mean mixed-layer aNCP of ~1.9 ± 0.5 mol C m^{-2} yr^{-1} (**Table 1**). Annual $CaCO_3$ production is estimated to be ~0.4 ± 0.2 mol C m^{-2} yr^{-1}, giving an annual particulate inorganic carbon (PIC) to particulate organic carbon (POC) ratio of 0.21 ± 0.1 based on the annual composites.

5. Discussion

Seven years of high-frequency CO_2 observations were used to compute net community production and calcium carbonate precipitation at Ocean Station Papa. The biological production at this location largely compensates for vertical mixing processes that add DIC to the mixed layer throughout the year. NCP dominates the biological component of this mixed-layer DIC draw down with $CaCO_3$ production comprising a small fraction of the annual productivity (**Figure 9A-B**).

The seasonal cycle of NCP rates (**Figure 10A**) at OSP indicates that the peak biological activity occurs in spring of each year and persists at a lower rate through summer. Our finding of significant spring production differs from prior investigations that have found low variation in primary production between spring and summer [*Wong et al.*, 1995]; however, sustained *in situ* observations from the spring season are lacking. During spring, thermal stratification coupled with the passing of storms results in rapid changes in mixed layer depth at OSP (**Figure 7F**). The use of climatological vertical carbon gradients in our budget at times when the mixed layer is rapidly

oscillating between depth levels but when net shoaling is occurring may result in overestimation of the vertical carbon input. This would cause our spring estimates to be biased towards more NCP, which may explain the larger rates seen in these months. On the other hand, primary production in a shoaling mixed layer during spring would cause the vertical carbon gradient at the base of the mixed layer to increase, which could to underestimation of the vertical carbon input. In addition, the loss of NCP below the rapidly shoaling spring mixed layer would also lead to an underestimation of spring NCP, as discussed by *Körtzinger et al.*, (2008). Without *in situ* observations of the vertical carbon gradients, it is challenging to determine how the use of climatological gradients may bias the spring production signal.

In fall, NCP rates switch from being autotrophic to heterotrophic, indicating that community respiration is larger than the gross photosynthetic production in fall and winter. This seasonal heterotrophy has been identified once previously in the Alaska Gyre region by *Chierici et al.*, (2006; **Figure 10A**) using a mixed-layer CO_2 budget approach based on ~monthly observations throughout the year 2000. Sediment trap observations spanning more than two decades suggest that particle export at OSP occurs throughout the year, with peaks in the spring and summer months [*Wong et al.*, 1999; *Timothy et al.*, 2013]. In order to have a POC flux in fall and winter but still observe heterotrophic NCP rates, the remineralization of POC and DOC in the mixed layer must exceed the POC production rate. Seasonal NCP at OSP sums to more than twice the magnitude of the winter carbon requirement for heterotrophy (~3.5 mol C m^{-2} versus ~1.25 mol C m^{-2}, respectively), which means that fall and winter heterotrophy could be fueled by local sources of carbon. Because there is continuous particle export during fall and winter [*Timothy et al.*, 2013],

it is likely that seasonal heterotrophy is primarily fueled by DOC rather than POC, as has been observed previously at BATS [*Carlson et al.*, 1994].

Prior investigators estimate that annual DOC production at OSP comprises 25-50% of the primary production [*Bishop et al.*, 1999], though there is some discrepancy among studies [*Wong et al.*, 2002c]. 50% of our aNCP estimate is equivalent to ~1 mol C m^{-2}, which accounts for nearly all of the heterotrophic signal we see in winter and is a lower limit estimate since NCP is less than the primary production. In addition, *Emerson*, (2014) suggests that less than 20% of the organic carbon remineralization in the upper pycnocline is caused by DOC degradation at OSP, indicating that little DOC export occurs in this region. Approximately 1.25 mol C m^{-2} of carbon produced from heterotrophy in a 75m mixed layer would require a DOC concentration reduction of ~16 µmol kg^{-1}. DOC concentrations at OSP were ~60 µmol kg^{-1} in the winter mixed layer during CLIVAR cruise P16 in February of 2006, and *Wong et al.*, (2002c) observed similar DOC concentrations (~65 µmol kg^{-1}) during February of 1997 that increased to ~80 µmol kg^{-1} in June of 1997 and were found to be as high as ~90 µmol kg^{-1} in May of 1995. Assuming that DOC is not building up in this region and that these observations reflect a seasonal cycle of ~15-25 µmol DOC kg^{-1} in the OSP mixed layer [*Wong et al.*, 2002c], degradation of DOC during fall and winter could explain the seasonal heterotrophy signal found herein. It should be noted, that the seasonal entrainment of lower DOC waters during the fall would also play a role in reducing the mixed-layer DOC concentration, in addition to biological consumption [*Hansell and Carlson*, 2001].

Table 1. Summer and annual mixed-layer NCP rates and aNCP estimates at Ocean Station Papa.

Method	Summer NCP rate mmol C m^{-2} d^{-1}	aNCP rate mmol C m^{-2} d^{-1}	aNCP mol C m^{-2} yr^{-1}	Reference
NO_3^- drawdown	11.8			Wong et al., 2002c
^{234}Th-^{238}U disequilibrium	8.1-9			Charette et al., 1999
O_2 mass balance	8.3-25			Emerson, 1987
O_2, Ar, N_2 mass balance	8.9-11.7			Emerson et al., 1991
In situ O_2, N_2	16.6		2.5 ± 1[a]	Emerson and Stump, 2010
O_2, Ar mass balance	13.1			Giesbrecht et al., 2012
O_2, Ar mass balance	11.2[b]			Juranek et al., 2012
DIC, TA mass balance	11.6 ± 4[c]	5.2 ± 1	1.9 ± 0.5[d]	This study
Mean ± StDev.	**12.3 ± 5**	**5.2**	**2.2 ± 0.4**	

[a]Summertime NCP rate scaled for 150 days of fixed rate production.
[b]Mean of spring and summer oxygen production rates scaled using the 1.45 O_2/C conversion.
[c]Mean of the September 20 integrated NCP from all years divided by the number of days since the start of the deployment (94) ± the standard deviation, in absolute value.
[d]Mean of annual NCP estimates for 2007-2008 and 2010-2011 deployments ± the standard deviation, in absolute value.

Variability in NCP throughout the year indicates that estimates of aNCP based on discrete or seasonal rate evaluations may be biased unless the observations happen to reflect the mean annual NCP rate. In this analysis, the full annual cycle of NCP was resolved, capturing spring and summer production as well as winter heterotrophy during the 2007-2008 and 2010-2011 deployments. Most prior NCP estimates have been conducted during the summer period and agree well with our summer NCP rates (**Table 1**). In particular, *Emerson and Stump*, (2010) used *in situ* oxygen data from the 2007-2008 OSP mooring deployment to estimate the summer NCP using a mass balance approach. They then scaled the summertime rate by 150 days of production to estimate the annual NCP, getting a value of 2.5 ± 1 mol C m^{-2} yr^{-1}. Our aNCP estimates agree within the errors (**Table 1**); however, perhaps not for the right reasons. Based on this analysis, there are approximately seven months of productivity at OSP (~210 days). If the *Emerson and Stump*, (2010) summertime rate were scaled by this longer duration of production, the aNCP would be 3.5 mol C m^{-2} yr^{-1};

significantly higher than the aNCP derived herein. This overestimation reflects the much higher summertime production rate relative to the annual production rate of 5.2 ± 0.3 mmol C m^{-2} d^{-1} derived from our aNCP estimate (**Table 1**). These findings indicate that summertime production is not necessarily a good estimator of the annual mean NCP rate and will lead to overestimation of the aNCP when scaled by the appropriate duration of the productive period.

$CaCO_3$ production at OSP begins in winter and peaks in spring, with sustained lower production in summer. A few of the fall $CaCO_3$ production estimates suggest that dissolution is occurring, which is unexpected in this region where both aragonite and calcite are saturated at the sea surface [*Feely*, 2002]. These values are not statistically significant, but suggest that $CaCO_3$ production may be very low at this time of year. The particulate inorganic carbon to particulate organic carbon ratio (PIC:POC) derived from the composite aNCP and $aCaCO_3$ is 0.21 ± 0.1. Prior PIC:POC estimates at OSP based on independent methodologies have found PIC:POC ratios ranging from 0.18 to 0.5, encompassing our estimate (**Table 2**). The global average PIC:POC ratio is ~0.075 and is significantly lower than what has been observed at OSP (**Table 2**). Thus, our findings add the growing body of evidence suggesting that the eastern subarctic pacific exhibits exceptionally high $CaCO_3$ production [*Wong et al.*, 1999, 2002c; *Lipsen et al.*, 2007; *Emerson et al.*, 2011; *Timothy et al.*, 2013]. Differences in the seasonality of NCP and $CaCO_3$ production results in seasonal PIC:POC ratio changes. Low PIC:POC ratios occur in summer and fall and are elevated in winter and spring when $CaCO_3$ production begins before NCP becomes autotrophic. Similar seasonal variability in the PIC:POC ratio was found by *Timothy et al.*, (2013) from two decades of sediment flux data from OSP, suggesting that our analysis accurately captures the seasonality of NCP and $CaCO_3$ production.

Table 2. Ocean Station Papa and global ocean PIC:POC ratio estimates.

OSP Estimate Method	**PIC:POC**	**Reference**
200m sediment traps (1982-1993)	0.5	Wong et al., 1999
50m sediment traps (1987-1997)	0.4	Wong et al., 2002c
^{14}C incubations (1998-2000)	0.25	Lipsen et al., 2007
In situ O_2, N_2, pH and pCO_2 based model (2007)	0.5	Emerson et al., 2011
50m sediment-trap-based estimate (1982-2006)	0.18	*Timothy et al.*, 2013
DIC, TA mass balance (2007-2008, 2010-2011)	0.21 ± 0.1	This study
Mean ± StDev.	**0.34 ± 0.1**	
Global Estimate Method	**PIC:POC**	**Reference**
Ocean general circulation model	0.09	Jin et al., 2006
Ocean biogeochemical-transport box model	0.06 ± 0.03	Sarmiento et al., 2002
Mean ± StDev.	**0.075 ± 0.02**	

In addition to seasonal variability in NCP at OSP, there appears to be notable summertime interannual variability. Interannual variations are somewhat smaller in winter and spring; however, there are fewer data during these periods, so further observations are needed. The largest anomaly in the time series occurred during late summer and fall of the 2008-2009 deployment when a volcanic eruption in the Aleutian Islands dispersed iron rich ash throughout the Gulf of Alaska, fueling an anomalous phytoplankton bloom [*Hamme et al.*, 2010]. Unfortunately, the mooring broke free shortly after the event so we do not have an estimate of the resulting aNCP. Another notable deviation in the time-series is the markedly lower summer production during the 2013-2014 mooring deployment relative to other years. Sea surface temperatures were ~2 ºC higher throughout the entirety of this deployment (**Figure 1A**), which may reflect a regional circulation anomaly that may have influenced NCP or altered the carbon gradients in the region. Thus this signal could be the result of low biological production or an advective process that is not captured in our methodology due to the use of climatological gradients. Unfortunately this deployment also

lacks observations through spring, so it is unclear how the anomaly may have influenced the aNCP estimate.

Although there are only two years in this analysis from which aNCP can be estimated, the interannual variability in aNCP is small (0.2 mol C m^{-2} yr^{-1}). This may be a result of the regional halocline "barrier layer" that restricts the depth of the winter mixed layer, and thus the depth over which carbon must be exported in order to contribute to aNCP. Unfortunately, this data set lacks full annual observations from years with anomalous spring and/or summer production. If higher spring/summer NCP leads to more carbon export, this could give rise to significant interannual variations in aNCP. If, however, spring/summer production were consistently re-entrained during the fall, the aNCP may be fairly constant in this region. In either case, interannual variability in the summertime organic carbon drawdown at this location due to stochastic events [*Hamme et al.*, 2010] and large scale climate variability [*Wong et al.*, 1999, 2002a; *Lipsen et al.*, 2007] makes it challenging to estimate aNCP from seasonally based NCP estimates. Our results indicate that the mixed-layer aNCP at OSP is ~1.9 ±0.5 mol C m^{-2} yr^{-1} and the $aCaCO_3$ production is ~0.4 ±0.2 mol C m^{-2} yr^{-1}. Further observations from this time-series site will fill in the data poor spring period and ultimately give a robust baseline for biologically-mediated carbon cycling that can be used to assess future changes in the biological pump and to study carbon cycle couplings with the climate system.

6. Conclusions

Net community production (NCP) and calcium carbonate ($CaCO_3$) precipitation were estimated from seven years of high-frequency moored observations at Ocean Station Papa (OSP).

Surface ocean total alkalinity and dissolved inorganic carbon time-series were derived from *in situ* observations of salinity and carbon dioxide and used to diagnostically assess the influence of gas exchange, physical processes, evaporation and precipitation, NCP, and $CaCO_3$ production on mixed-layer carbon inventories using a dual tracer mixed-layer mass balance approach. Significant seasonal variations in NCP coupled with interannual variability in summertime NCP in this region where chlorophyll levels remain low year-round and the system is known to be iron limited [*Martin and Fitzwater*, 1988], suggests that carbon cycling at OSP may be more complex than previously thought. These findings also indicate that discrete or seasonal observations of NCP may not be scalable to annual assessments and that continuous monitoring is needed to better constrain aNCP.

With a modern baseline for biological carbon cycling coming into focus at this location, continued observations will make it possible to evaluate how the biological pump is responding to ocean acidification and climate change. Our methodology relies on salinity based estimates of surface ocean TA, which integrates the influence of $CaCO_3$ processes rather than independently resolving calcification in real time. While this adds uncertainty to the TA budget, uncertainty in the DIC budget is likely minimal due to the very close agreement between our estimated DIC time-series and contemporaneous discrete bottle samples from the region. The TA budget could be improved with the aid of additional sensors that capture *in situ* calcification events. The pH and CO_2 sensors used during OSP deployments between 2007-2014 did not perform at the accuracy level required to calculate DIC and TA with confidence; however, these data have been used successfully to constrain carbonate system processes indirectly at OSP [*Emerson et al.*, 2011]. As autonomous DIC and TA sensors come online for moored application, direct observations of episodic $CaCO_3$ processes [*Wong et al.*, 1999] will improve our estimates. Until that time, the

method used herein introduces an independent estimate of carbon cycling that adds to the growing body of work at OSP.

7. Acknowledgments

The authors thank Noel Pelland for providing glider data used in this analysis as well as Steven Emerson and Seth Bushinsky for insights and constructive feedback on the original draft of this manuscript. All mooring operations were performed aboard the CCGS Tully. We are very grateful for the shiptime provided by the Line P program and efforts of the Captain, crew, science party, and PMEL Ocean Climate Stations and Carbon Program group technicians, who made this data set possible. We also thank the repeat hydrography and line P research teams for making their data around OSP publically available. This work was funded by the NOAA Climate Program Office, the NOAA Ocean Acidification Program and the NSF IGERT Program on Ocean Change.

8. Appendix A: Uncertainty Assessment

8.1. Data Filling With Buoy Sensors

Errors in the temperature and salinity measurements are based primarily upon the changes between pre- and post-deployment calibration drifts [*Freitag et al.*, 1999]. In addition, in situ calibrations are performed based upon gravitational stability considerations [*Freitag et al.*, 1999]. Numerous conductivity-temperature-depth sensors have been deployed throughout the NOAA Station Papa mooring deployment history. The largest instrumental errors for temperature and salinity sensors in the time-series history were applied to all deployments for simplicity as these measurements were not a significant source of error in the budget. During time periods when surface salinity and temperature measurements were missing, subsurface measurements (5m, 10m

and 20m) were used to fill in the gaps. To determine an error for these fill periods, daily climatologies of the difference between the subsurface and surface measurements were developed from time periods when the surface sensors were functioning. Matching year day climatology errors were used for each day that data were filled.

8.2. TA and DIC Estimates

Errors in calculated TA were derived using a Monte Carlo simulation in which the salinity values and the linear regression coefficients were varied around their uncertainties for 1,000 computation iterations. The standard deviations of the 1,000 resultant TA values at each time point were then used as the uncertainty estimates for TA. Uncertainties for calculated DIC were also derived using a Monte Carlo simulation in which TA values and *in situ* xCO_2 values were varied around their uncertainties for 1,000 computation iterations using the program CO_2Sys. The standard deviations of the 1,000 resultant DIC values at each time point were then used as the uncertainty estimates for DIC.

8.3. Gas Exchange

The buoy CO_2 and anemometer sensor errors were propagated through calculations and when wind measurements were absent, gaps were filled with 0.25 degree, 6 hourly, cross-calibrated multi-platform ocean surface winds from NASA [*Atlas et al.*, 2011]. To calculate an error for these data fill periods, the mean difference between NASA winds and buoy measured winds from April to December of 2008 (spanning the two week gap in anemometer data) was calculated. This difference was used as an estimate of the error in the NASA winds used for filling. In addition to

sensor errors that contribute to gas exchange uncertainty, we include a 30% error for the gas transfer velocity after *Nightingale et al.*, (2000).

8.4. Physical Processes

For mixed-layer transport estimates, horizontal velocity profiles within the mixed layer were determined from ADCP and current meters and averaged over the mixed layer at each time step, with sensor errors propagated through the averaging. During time periods when *in situ* current data were missing, OSCAR surface currents were used to fill in data gaps [*Bonjean and Lagerloef*, 2002]. Mean *in situ* mixed-layer flow speeds in the meridional and zonal directions were subsampled to the 5 day OSCAR time series frequency and the difference between the subsampled *in situ* data and OSCAR estimates was calculated. The mean difference over the entire deployment history was used as the error for OSCAR currents during current data fill periods.

Mixed layer depth errors were prescribed as one quarter of the vertical separation between the sensors spanning the mixed layer depth. Higher spatial resolution glider based estimates of the mixed layer depth have an error of ±2m. Errors in the mixed layer depth tendency rate ($\partial h\ \partial t^{-1}$) were calculated using standard propagation of errors, assuming errors at each time step were not correlated.

Vertical velocity error was estimated as 0.15 m day^{-1} based upon comparison with glider estimated vertical velocity (Noel Pelland, personal communication). Diffusivity errors were computed for 5-day smoothed estimates through propagation of errors, following Cronin et al. (2013). The standard error in the climatological monthly diffusivity values were then computed as

the root-mean-square of the errors for a given month, reduced by the square root of the degrees of freedom, assumed here to be the number of years in the time series for the given month.

Multiple linear regressions (MLR) were assessed using the *stepwise* function in MATLAB R2014a (The MathWorks Inc., Natick, MA, 2000) to identify significant correlations. The variance inflation factor (VIF) was used to assess coefficient error inflation due collinearity between predictor variables where VIF>10 was used as a threshold. Once ideal predictor variables were identified, the MATLAB *robustfit* function was used to fit the MLR while decreasing the weight of potential outliers.

To estimate errors in the MLR derived monthly DIC and TA gradients, differences between World Ocean Atlas 2013 (WOA) optimally interpolated fields and the data used to construct the fields within 10 degrees latitude and 15 degrees longitude of OSP were averaged at each depth level. Approximately ~100 values went into each depth average, giving depth dependent error estimates for each predictor field in the OSP region. These errors along with standard errors in the MLR regression coefficients were propagated through a Monte Carlo simulation 1,000 times to estimate the error in the predicted DIC and TA fields for each month. The resultant errors were then propagated using standard methods through the gradient and mixing computations.

Parameterization of the physical processes contributes the most to uncertainties in the overall closing of the budget. Specifically, uncertainty in the vertical salinity, DIC and TA gradients at the base of the mixed layer (~19-100%; **Tables A.1** and **A.2**) coupled with uncertainties in the mixed layer depth (~5-13%) and turbulent diffusion (κ;~10-88%), give rise to 68% error bounds on the

daily fluxes (μmol kg^{-1} d^{-1}) that are often larger than 100%. Observations of the vertical salinity, DIC, TA and salinity gradients during hydrographic cruises near OSP (**Figure 6**) give confidence to the sign, magnitude and seasonality of those computed herein, so we believe our uncertainty bounds are highly conservative. **Tables A.1** and **A.2** give the monthly mean uncertainties for each of the budget term daily fluxes as well as the vertical gradients. When the daily physical fluxes are integrated over each annual deployment (**Section 5.1**) the errors are summed in quadrature, which reduces the uncertainty substantially, giving the 68% uncertainty bounds shown in **Figures 8-10** for the physical DIC and TA terms.

8.5. Evaporation and Precipitation

Horizontal and vertical salinity gradients were computed from World Ocean Atlas (WOA) 2013 monthly salinity fields. The method described in the previous section was used to determine depth dependent errors in the WOA salinity field near OSP, which were then propagated through the salinity mixing and EP calculations.

Table A.1. Mean monthly values for the annual composites of integrated NCP and $CaCO_3$ production based on all deployment years as well as the 68% calculation uncertainties (not standard deviations).

	NCP mol C m^2	NCP mol C m^2	$CaCO_3$ mol C m^2	$CaCO_3$ mol C m^2
Month	**value**	**1σ %**	**value**	**1σ %**
6	-0.1	59.6	0.00	>100
7	-0.5	11	-0.04	75
8	-0.9	6	-0.06	45
9	-1.0	6	-0.06	54
10	-0.9	10	-0.06	75
11	-0.4	36	-0.07	96
12	0.0	>100	-0.09	>100
1	0.2	>100	-0.13	86
2	0.0	>100	-0.18	67
3	-0.2	>100	-0.27	55
4	-0.9	45.5	-0.36	56
5	-1.6	31.7	-0.40	60

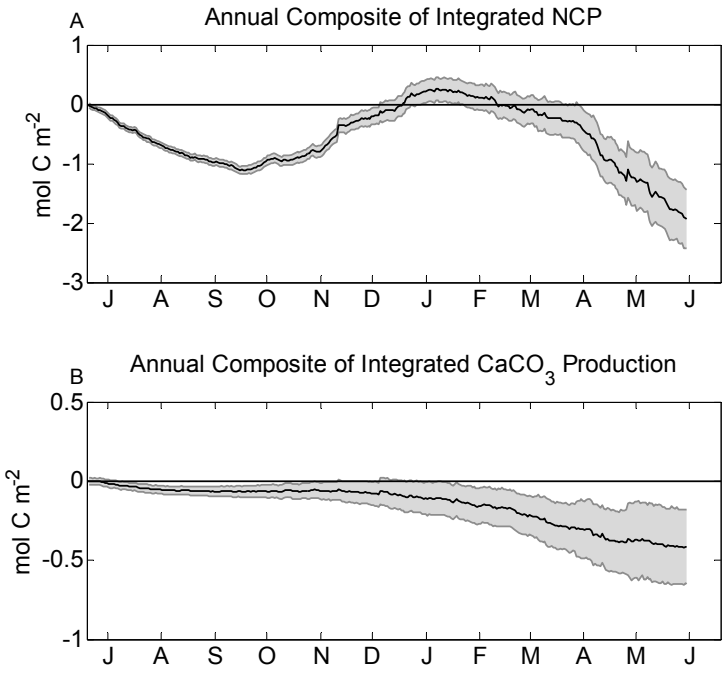

Figure A.1. Annual composites of integrated (**A**) NCP and (**B**) $CaCO_3$ production with 68% calculation uncertainties shown (not standard deviations).

Table A.2. Monthly climatology of the turbulent diffusion as well as 1σ % errors for the turbulent diffusion term, mixed layer depth, daily salinity fluxes due to EP and physical processes, and the vertical salinity gradients.

	κ	κ	MLD	Sal_{EP}	Sal_{Phys}	$\partial Sal\ \partial z^{-1}$	$(Sal_a-Sal_h)/h$
	$m^2\ d^{-1}$	$m^2\ d^{-1}$	m	d^{-1}	d^{-1}	m^{-1}	m^{-1}
Month	**values**	**% Error**	**% Error**	**% Error**	**% Error**	**% Error**	**% Error**
1	4.0E-04	61	5	>100	>100	>100	76
2	6.0E-04	79	5	>100	90	>100	67
3	1.5E-03	88	5	>100	56	>100	56
4	3.7E-03	42	6	>100	>100	>100	>100
5	5.0E-04	31	7	>100	>100	>100	>100
6	3.0E-04	12	9	>100	50	>100	>100
7	1.0E-04	12	10	>100	22	57	54
8	1.0E-04	10	13	>100	>100	48	41
9	1.0E-04	10	9	>100	>100	>100	>100
10	1.0E-04	12	8	>100	>100	>100	>100
11	3.0E-04	19	8	>100	>100	>100	>100
12	3.0E-04	34	6	>100	>100	>100	>100

Table A.3. 1σ errors for the calculated DIC and TA time series values and 1σ % errors for each daily flux term in the DIC and TA budgets. 1σ % errors on the vertical gradients are also given. For this table, μM is used as shorthand for μmol kg^{-1}.

	DIC μM*	DIC_{Gas} μM d^{-1}	DIC_{EP} μM d^{-1}	DIC_{Phys} μM d^{-1}	$\partial DIC\ \partial z^{-1}$ μM m^{-1}	$(DIC_a\text{-}DIC_h)/h$ μM m^{-1}	DIC_{Bio} μM	TA μM	TA_{EP} μM d^{-1}	TA_{Phys} μM d^{-1}	$\partial TA\ \partial z^{-1}$ μM m^{-1}	$(TA_a\text{-}TA_h)/h$ μM m^{-1}	TA_{Bio} μM
Month	**1σ**	**1σ %**	**1σ %**	**1σ %**	**1σ %**	**1σ %**	**1σ %**	**1σ**	**1σ %**	**1σ %**	**1σ %**	**1σ %**	**1σ %**
1	3.0	29	>100	74	45	19	17	3.4	>100	85	87	48	>100
2	3.0	29	>100	87	58	21	19	3.4	>100	85	99	58	>100
3	3.0	29	>100	45	>100	20	19	3.4	>100	60	>100	56	91
4	2.9	30	>100	18	>100	21	16	3.4	>100	>100	>100	>100	>100
5	2.9	30	>100	>100	67	24	13	3.4	>100	>100	>100	>100	>100
6	2.9	31	>100	7	58	45	67	3.4	>100	>100	>100	>100	>100
7	2.9	32	>100	68	24	37	21	3.4	>100	40	52	29	>100
8	2.9	33	>100	>100	34	67	12	3.4	>100	>100	>100	>100	>100
9	2.9	30	>100	40	42	73	10	3.4	>100	>100	>100	>100	>100
10	2.9	30	>100	>100	52	>100	10	3.4	>100	>100	>100	>100	>100
11	2.9	30	>100	>100	43	54	13	3.4	>100	>100	>100	>100	>100
12	2.9	29	>100	>100	90	33	15	3.4	>100	>100	>100	>100	>100

*μM in this case is shorthand for μmol kg^{-1}.

9. References

Anderson, L. A., and J. L. Sarmiento (1994), Redfield ratios of remineralization determined by nutrient data analysis, *Global Biogeochem. Cycles*, *8*(1), 65–80.

Astor, Y. M., L. Lorenzoni, R. Thunell, R. Varela, F. Muller-Karger, L. Troccoli, G. T. Taylor, M. I. Scranton, E. Tappa, and D. Rueda (2013), Interannual variability in sea surface temperature and fCO_2 changes in the Cariaco Basin, *Deep Sea Res. Part II Top. Stud. Oceanogr.*, *93*, 33–43, doi:10.1016/j.dsr2.2013.01.002.

Atlas, R., R. N. Hoffman, J. Ardizzone, S. M. Leidner, J. C. Jusem, D. K. Smith, and D. Gombos (2011), A Cross-calibrated, Multiplatform Ocean Surface Wind Velocity Product for Meteorological and Oceanographic Applications, *Bull. Am. Meteorol. Soc.*, *92*(2), 157–174, doi:10.1175/2010BAMS2946.1.

Ayers, J. M., and M. S. Lozier (2012), Unraveling dynamical controls on the North Pacific carbon sink, *J. Geophys. Res.*, *117*(C1), C01017, doi:10.1029/2011JC007368.

Bates, N. R. (2012), Multi-decadal uptake of carbon dioxide into subtropical mode water of the North Atlantic Ocean, *Biogeosciences*, *9*(7), 2649–2659, doi:10.5194/bg-9-2649-2012.

Bates, N. R., Y. M. Astor, M. J. Church, K. I. Currie, J. Dore, M. Gonaález-Dávila, L. Lorenzoni, F. Muller-Karger, J. Olafsson, and M. Santa-Casiano (2014), A Time-Series View of Changing Ocean Chemistry Due to Ocean Uptake of Anthropogenic CO_2 and Ocean Acidification, *Oceanography*, *27*(1), 126–141, doi:10.5670/oceanog.2014.16.

Bentamy, A., and D. C. Fillon (2012), Gridded surface wind fields from Metop/ASCAT measurements, *Int. J. Remote Sens.*, *33*(6), 1729–1754, doi:10.1080/01431161.2011.600348.

Bishop, J. K., S. Calvert, and M. Soon (1999), Spatial and temporal variability of POC in the northeast Subarctic Pacific, *Deep Sea Res. Part II Top. …*, *46*, 2699–2733.

Bonjean, F., and G. S. E. Lagerloef (2002), Diagnostic model and analysis of the surface currents in the tropical Pacific Ocean, *J. Phys. Ocean.*, *32*, 2938–2954.

De Boyer Montégut, C. (2004), Mixed layer depth over the global ocean: An examination of profile data and a profile-based climatology, *J. Geophys. Res.*, *109*(C12), C12003, doi:10.1029/2004JC002378.

Brix, H., N. Gruber, and C. C. D. Keeling (2004), Interannual variability of the upper ocean carbon cycle at station ALOHA near Hawaii, *Global Biogeochem. Cycles*, *18*(4), n/a–n/a, doi:10.1029/2004GB002245.

Carlson, C., H. Ducklow, and A. Michaels (1994), Annual flux of dissolved organic carbon from the euphotic zone in the northwestern Sargasso Sea, *Nature*, *371*.

Charette, M., S. B. Moran, and J. Bishop (1999), ^{234}Th as a tracer of particulate organic carbon export in the subarctic northeast Pacific Ocean, *Deep Sea Res. Part II ...*, *46*.

Chierici, M., A. Fransson, and Y. Nojiri (2006), Biogeochemical processes as drivers of surface fCO_2 in contrasting provinces in the subarctic North Pacific Ocean, *Global Biogeochem. Cycles*, *20*(1), doi:10.1029/2004GB002356.

Ciais, P. et al. (2013), Carbon and Other Biogeochemical Cycles, in *Climate Change 2013: The Physical Science Basis*, edited by V. B. and P. M. M. (eds. . Stocker, T.F., D. Qin, G.-K. Plattner, M. Tignor, S.K. Allen, J. Boschung, A. Nauels, Y. Xia, Cambridge University Press, Cambridge, United Kingdom and New York, NY, USA.

Cronin, M. F., N. a. Bond, J. Thomas Farrar, H. Ichikawa, S. R. Jayne, Y. Kawai, M. Konda, B. Qiu, L. Rainville, and H. Tomita (2013), Formation and erosion of the seasonal thermocline in the Kuroshio Extension Recirculation Gyre, *Deep Sea Res. Part II Top. Stud. Oceanogr.*, *85*, 62–74, doi:10.1016/j.dsr2.2012.07.018.

Cullison Gray, S. E., M. D. DeGrandpre, T. S. Moore, T. R. Martz, G. Friederich, and K. S. Johnson (2011), Applications of in situ pH measurements for inorganic carbon calculations, *Mar. Chem.*, *125*, 82–90, doi:10.1016/j.marchem.2011.02.005.

Dickson, A. G. (1990), Standard potential of the reaction : $AgCl_{(s)} + 1/2H_{2(g)} = Ag_{(s)} + HCl_{(aq)}$, and the standard acidity constant of the ion HSO_4^- in synthetic sea water from 273.15 to 318.15 K, *J. Chem. Thermodyn.*, (22), 113–127.

Dickson, A. G., and J. Riley (1978), The effect of analytical error on the evaluation of the components of the aquatic carbon-dioxide system, *Mar. Chem.*, *6*, 77–85, doi:10.1016/0304-4203(78)90008-7.

Dore, J., R. Lukas, D. W. Sadler, M. J. Church, and D. M. Karl (2009), Physical and biogeochemical modulation of ocean acidification in the central North Pacific., *Proc. Natl. Acad. Sci. U. S. A.*, *106*(30), 12235–40, doi:10.1073/pnas.0906044106.

Emerson, S. R. (1987), Seasonal oxygen cycles and biological new production in surface waters of the subarctic Pacific Ocean, *J. Geophys. Res. Ocean.*, *92*, 6535–6544.

Emerson, S. R. (2014), Annual net community production and the biological carbon flux in the ocean, *Global Biogeochem. Cycles*, 14–28, doi:10.1002/2013GB004680.Received.

Emerson, S. R., and C. Stump (2010), Net biological oxygen production in the ocean—II: Remote in situ measurements of O_2 and N_2 in subarctic pacific surface waters, *Deep Sea Res. Part I Oceanogr. Res. Pap.*, *57*(10), 1255–1265, doi:10.1016/j.dsr.2010.06.001.

Emerson, S. R., P. D. Quay, C. Stump, D. Wilbur, and M. Knox (1991), O_2, Ar, N_2, and ^{222}Rn in surface waters of the subarctic ocean: Net biological O_2 production, *Global Biogeochem. Cycles*, *5*(1), 49–69.

Emerson, S. R., C. L. Sabine, M. F. Cronin, R. A. Feely, S. E. Cullison Gray, and M. D. DeGrandpre (2011), Quantifying the flux of $CaCO_3$ and organic carbon from the surface ocean using in situ measurements of O_2, N_2, pCO_2, and pH, *Global Biogeochem. Cycles*, *25*(3), 1–12, doi:10.1029/2010GB003924.

Fassbender, A. J., C. L. Sabine, N. Lawrence-Slavas, E. H. De Carlo, C. Meinig, and S. M. Jones (2014), A Robust Sensor for Extended Autonomous Measurements of Surface Ocean Dissolved Inorganic Carbon., *Submitted*.

Feely, R. A. (2002), In situ calcium carbonate dissolution in the Pacific Ocean, *Global Biogeochem. Cycles*, *16*(4), 1–12, doi:10.1029/2002GB001866.

Feely, R. A. et al. (2008), *Carbon Dioxide, Hydrographic, and Chemical Data Obtained During the R/Vs Roger Revelle and Thomas G. Thompson Repeat Hydrography Cruises in the Pacific Ocean: CLIVAR CO2 Sections P16S_2005 (9 Jan. - 19 Feb. 2005) and P16N_2006 (13 Feb. - 30 Mar.)*.

Feely, R. A., C. L. Sabine, and S. R. Emerson (2011), *Carbon Dioxide, Hydrographic, and Chemical Data Obtained During the R/V Thomas Thompson "Student" Cruise TN224 in the Pacific Ocean (Aug. 26 - September 17, 2008)*.

Freeland, H. J. (2007), A short history of Ocean Station Papa and Line P, *Prog. Oceanogr.*, *75*(2), 120–125, doi:10.1016/j.pocean.2007.08.005.

Freitag, H. P., M. E. McCarty, C. Nosse, R. Lukas, M. J. McPhaden, and M. F. Cronin (1999), *COARE Seacat data: Calibrations and quality control procedures*.

Fukasawa, M., T. Kawano, A. Murata, H. Uchida, and T. Doi (2007), *Carbon Dioxide, Hydrographic, and Chemical Data Obtained During the R/V Mirai Repeat Hydrography Cruise in the Pacific Ocean: CLIVAR CO_2 Section P01 2007 (July 24 – September 3, 2007)*.

Garcia, H. E., R. A. Locarnini, T. P. Boyer, J. I. Antonov, A. V. Mishonov, O. K. Baranova, M. M. Zweng, J. R. Reagan, and D. R. Johnson (2013a), World Ocean Atlas 2013. Vol. 3: Dissolved Oxygen, Apparent Oxygen Utilization, and Oxygen Saturation, in *NOAA Atlas NESDIS 75*, edited by S. Levitus and A. Mishonov, p. 27.

Garcia, H. E., R. A. Locarnini, T. P. Boyer, J. I. Antonov, O. K. Baranova, M. M. Zweng, J. R. Reagan, and D. R. Johnson (2013b), World Ocean Atlas 2013. Vol. 4: Dissolved Inorganic Nutrients (phosphate, nitrate, silicate), in *NOAA Atlas NESDIS 76*, vol. 4, edited by S. Levitus and A. Mishonov, p. 25.

Giesbrecht, K. E., R. C. Hamme, and S. R. Emerson (2012), Biological productivity along Line P in the subarctic northeast Pacific: In situ versus incubation-based methods, *Global Biogeochem. Cycles*, *26*(3), n/a–n/a, doi:10.1029/2012GB004349.

Gledhill, D., R. Wanninkhof, and C. M. Eakin (2009), Observing ocean acidification from space, *Oceanography*, *22*(4), 48–59, doi:10.5670/oceanog.2009.96.

González-Dávila, M., J. M. Santana-Casiano, M. J. Rueda, and O. Llinás (2010), The water column distribution of carbonate system variables at the ESTOC site from 1995 to 2004, *Biogeosciences*, *7*(10), 3067–3081, doi:10.5194/bg-7-3067-2010.

Gruber, N., C. D. Keeling, and T. F. Stocker (1998), Carbon-13 constraints on the seasonal inorganic carbon budget at the BATS site in the northwestern Sargasso Sea, *Deep Sea Res. Part I Oceanogr. Res. Pap.*, *45*(4-5), 673–717, doi:10.1016/S0967-0637(97)00098-8.

Hales, B., P. G. Strutton, M. Saraceno, R. Letelier, T. Takahashi, R. A. Feely, C. L. Sabine, and F. P. Chavez (2012), Satellite-based prediction of pCO_2 in coastal waters of the eastern North Pacific, *Prog. Oceanogr.*, *103*, doi:10.1016/j.pocean.2012.03.001.

Hamme, R. et al. (2010), Volcanic ash fuels anomalous plankton bloom in subarctic northeast Pacific, *Geophys. Res. Lett.*, *37*, doi:10.1029/2010GL044629.

Hansell, D. A., and C. A. Carlson (2001), Marine Dissolved Organic Matter and the Carbon Cycle, *Oceanography*, *14*(4), 41–49.

Van Heuven, S. M. A. C., D. Pierrot, J. W. B. Rae, E. Lewis, and D. W. R. Wallace (2011), MATLAB Program Developed for CO_2 System Calculations, *ORNL/CDIAC-105b. Carbon Dioxide Inf. Anal. Center, Oak Ridge Natl. Lab. U.S. Dep. Energy, Oak Ridge, Tennessee*. Available from: http://cdiac.ornl.gov/ftp/co2sys/CO2SYS_calc_MATLAB_v1.1/ (Accessed 2 July 2014)

Jin, X., N. Gruber, J. P. Dunne, J. L. Sarmiento, and R. a. Armstrong (2006), Diagnosing the contribution of phytoplankton functional groups to the production and export of particulate organic carbon, CaCO 3 , and opal from global nutrient and alkalinity distributions, *Global Biogeochem. Cycles*, *20*(2), n/a–n/a, doi:10.1029/2005GB002532.

Johnson, K. S., W. M. Berelson, E. S. Boss, Z. Chase, H. Claustre, S. R. Emerson, N. Gruber, A. Kortzinger, M. J. Perry, and S. C. Riser (2009), Observing biogeochemical cycles at global scales with profiling floats and gliders: Prospects for a global array, , *22*, 216–225, doi:10.5670/oceanog.2009.81.

Keeling, C. D., H. Brix, and N. Gruber (2004), Seasonal and long-term dynamics of the upper ocean carbon cycle at Station ALOHA near Hawaii, *Global Biogeochem. Cycles*, *18*(4), doi:10.1029/2004GB002227.

Körtzinger, a., U. Send, R. S. Lampitt, S. Hartman, D. W. R. Wallace, J. Karstensen, M. G. Villagarcia, O. Llinás, and M. D. DeGrandpre (2008), The seasonal pCO_2 cycle at 49°N/16.5°W in the northeastern Atlantic Ocean and what it tells us about biological productivity, *J. Geophys. Res.*, *113*(C4), C04020, doi:10.1029/2007JC004347.

Large, W. G., J. C. McWilliams, and S. C. Doney (1994), Oceanic vertical mixing: A review and a model with a nonlocal boundary layer parameterization, *Rev. Geophys.*, *32*(4), 363, doi:10.1029/94RG01872.

Lauvset, S. K., N. Gruber, P. Landschützer, a. Olsen, and J. Tjiputra (2014), Trends and drivers in global surface ocean pH over the past three decades, *Biogeosciences Discuss.*, *11*(11), 15549–15584, doi:10.5194/bgd-11-15549-2014.

Lipsen, M. S., D. W. Crawford, J. Gower, and P. J. Harrison (2007), Spatial and temporal variability in coccolithophore abundance and production of PIC and POC in the NE subarctic Pacific during El Niño (1998), La Niña (1999) and 2000, *Prog. Oceanogr.*, *75*(2), 304–325, doi:10.1016/j.pocean.2007.08.004.

Liu, W. T., K. B. Katsaros, and J. A. Businger (1979), Bulk parameterization of air-sea exchanges of heat and water vapor including the molecular constraints at the interface, *J. Atmos. Sci.*, *36*.

Locarnini, R. A., A. V. Mishonov, J. I. Antonov, T. P. Boyer, H. E. Garcia, O. K. Baranova, and D. S. M. M. Zweng, C. R. Paver, J. R. Reagan, D. R. Johnson, M. Hamilton (2013), World Ocean Atlas 2013, Volume 1: Temperature, in *NOAA Atlas NESDIS 73*, edited by S. Levitus and A. Mishonov, p. 40 pp.

Lockwood, D. (2013), Impact of the marine biological pump on atmospheric CO_2 uptake in the North Pacific: a study based on basin-wide underway measurements of oxygen/argon gas ratios and pO_2, University of Washington.

Lomas, M. W., N. R. Bates, R. J. Johnson, A. H. Knap, D. K. Steinberg, and C. A. Carlson (2013), Two decades and counting: 24-years of sustained open ocean biogeochemical measurements in the Sargasso Sea, *Deep Sea Res. Part II Top. Stud. Oceanogr.*, *93*, 16–32, doi:10.1016/j.dsr2.2013.01.008.

Lueker, T. J., A. G. Dickson, and C. D. Keeling (2000), Ocean pCO_2 calculated from dissolved inorganic carbon, alkalinity, and equations for K_1 and K_2: validation based on laboratory measurements of CO_2 in gas and seawater at equilibrium, *Mar. Chem.*, *70*, 105–119, doi:10.1016/S0304-4203(00)00022-0.

Martin, J., and S. Fitzwater (1988), Iron deficiency limits phytoplankton growth in the north-east Pacific subarctic, *Nature*.

McGillicuddy, D. J., A. Robinson, D. Siegel, H. Jannasch, R. Johnson, T. Dickey, J. McNeil, A. Michaels, and A. Knap (1998), Influence of mesoscale eddies on new production in the Sargasso Sea, *Nature*, *394*, doi:10.1038/28367.

McGillicuddy, D. J. et al. (2007), Eddy/wind interactions stimulate extraordinary mid-ocean plankton blooms., *Science*, *316*(5827), 1021–6, doi:10.1126/science.1136256.

Miller, L. A., J. Christian, M. Davelaar, W. K. Johnson, and J. Linguanti (2010), *Carbon Dioxide, Hydrographic and Chemical Data Obtained During the Time Series Line P Cruises in the North-East Pacific Ocean from 1985-2010*.

Millero, F. J. (2007), The marine inorganic carbon cycle., *Chem. Rev.*, *107*, 308–341, doi:10.1021/cr0503557.

Nightingale, P. D., G. Malin, C. S. Law, A. J. Watson, S. Liss, I. Liddicoat, P. S. Liss, M. I. Liddicoat, J. Boutin, and R. C. Upstill-Goddard (2000), In situ evaluation of air-sea gas exchange parameterizations using novel conservative and volatile tracers, *Glob. Biogeochem. Cycles*, *14*(1), 373–387.

Passow, U., and C. A. Carlson (2012), The biological pump in a high CO_2 world, *Mar. Ecol. Prog. Ser.*, *470*(2), 249–271, doi:10.3354/meps09985.

Quay, P. D., and J. Stutsman (2003), Surface layer carbon budget for the subtropical N. Pacific: constraints at station ALOHA, *Deep Sea Res. Part I Oceanogr. Res. Pap.*, *50*(9), 1045–1061, doi:10.1016/S0967-0637(03)00116-X.

Rhein, M. et al. (2013), Observations: Ocean, in *Climate Change 2013: The Physical Science Basis. Contribution of Working Group I to the Fifth Assessment Report of the Intergovernmental Panel on Climate Change*, edited by V. B. and P. M. M. Stocker, T.F., D. Qin, G.-K. Plattner, M. Tignor, S.K. Allen, J. Boschung, A. Nauels, Y. Xia, Cambridge University Press, Cambridge, United Kingdom and New York, NY, USA.

Sarmiento, J. L., J. P. Dunne, A. Gnanadesikan, R. M. Key, K. Matsumoto, and R. Slater (2002), A new estimate of the $CaCO_3$ to organic carbon export ratio, *Global Biogeochem. Cycles*, *16*(4), 54–1–54–12, doi:10.1029/2002GB001919.

Send, U. (2010), A Global Boundary Current Circulation Observing Network, in *Proceedings of OceanObs'09: Sustained Ocean Observations and Information for Society*, pp. 841–853, European Space Agency.

Signorini, S. R., C. R. McClain, J. R. Christian, and C. Wong (2001), Seasonal and interannual variability of phytoplankton, nutrients, TCO_2 , pCO_2 , and O_2 in the eastern subarctic Pacific (ocean weather station Papa), *J. Geophys. Res.*, *106*(C12), 31197–31215, doi:10.1029/2000JC000343.

Sugiura, K., and S. Tsunogai (2005), Spatial and temporal variation of surface xCO_2 providing net biological productivities in the western North Pacific in June, *J. Oceanogr.*, *61*.

Sutton, A. J. et al. (2014), A high-frequency atmospheric and seawater pCO_2 data set from 14 open ocean sites using a moored autonomous system, *Earth Syst. Sci. Data Discuss.*, *7*, 385–418, doi:10.5194/essdd-7-385-2014.

Takahashi, T. (2009), Reconciling opposing views on carbon cycling in the coastal ocean, *Deep Sea Res. Part II Top. Stud. Oceanogr.*, *56*(8-10), 554–577, doi:10.1016/j.dsr2.2008.12.009.

Takahashi, T., J. G. Goddard, and D. W. Chipman (1993), Seasonal Variation of CO_2 and Nutrients in the High-Latitude surface oceans: acomparative study, *Global Biogeochem. Cycles*, *7*(4), 843–878.

Takahashi, T., S. C. Sutherland, R. A. Feely, and R. Wanninkhof (2006), Decadal change of the surface water pCO_2 in the North Pacific: A synthesis of 35 years of observations, *J. Geophys. Res.*, *111*(C7), 1–20, doi:10.1029/2005JC003074.

Takahashi, T. et al. (2009), Climatological mean and decadal change in surface ocean pCO_2, and net sea–air CO_2 flux over the global oceans, *Deep Sea Res. Part II Top. Stud. Oceanogr.*, *56*(8-10), 554–577, doi:10.1016/j.dsr2.2008.12.009.

Taylor, G. T. et al. (2012), Ecosystem responses in the southern Caribbean Sea to global climate change., *Proc. Natl. Acad. Sci. U. S. A.*, *109*(47), 19315–20, doi:10.1073/pnas.1207514109.

Timothy, D., C. Wong, J. E. Barwell-Clarke, J. S. Page, L. A. White, and R. W. Macdonald (2013), Climatology of sediment flux and composition in the subarctic Northeast Pacific Ocean with biogeochemical implications, *Prog. Oceanogr.*, *116*, 95–129, doi:10.1016/j.pocean.2013.06.017.

Wanninkhof, R. (1992), Relationship Between Wind Speed and Gas Exchange Over the Ocean, *J. Geophys. Res.*, *97*(C5), 7373–7382, doi:10.1029/92JC00188.

Weiss, R. (1974), Carbon dioxide in water and seawater: the solubility of a non-ideal gas, *Mar. Chem.*, *2*(3), 203–215, doi:10.1016/0304-4203(74)90015-2.

Winn, C. D., Y.-H. Li, F. T. Mackenzie, and D. M. Karl (1998), Rising surface ocean dissolved inorganic carbon at the Hawaii Ocean Time-series site, *Mar. Chem.*, *60*(1-2), 33–47, doi:10.1016/S0304-4203(97)00085-6.

Wolfgladrow, D., R. E. Zeebe, C. Klaas, a Kortzinger, and A. G. Dickson (2007), Total alkalinity: The explicit conservative expression and its application to biogeochemical processes, *Mar. Chem.*, *106*(1-2), 287–300, doi:10.1016/j.marchem.2007.01.006.

Wong, C., F. A. Whitney, K. Iseki, J. S. C. Page, and J. Zeng (1995), Analysis of trends in primary productivity and chlorophyll-a over two decades at Ocean Station P (50 N, 145 W) in the subarctic Northeast Pacific Ocean, *Can. Spec. Publ. Fish. Aquat. Sci.*, *121*, 107–117.

Wong, C., F. A. Whitney, D. W. Crawford, K. Iseki, R. J. Matear, W. Johnson, J. S. C. Page, and D. Timothy (1999), Seasonal and interannual variability in particle fluxes of carbon, nitrogen and silicon from time series of sediment traps at Ocean Station P, 1982–1993: relationship to changes in subarctic primary productivity, *Deep Sea Res. Part II Top. Stud. Oceanogr.*, *46*(11-12), 2735–2760, doi:10.1016/S0967-0645(99)00082-X.

Wong, C., N. A. D. Waser, Y. Nojiri, W. K. Johnson, F. A. Whitney, J. S. C. Page, and J. Zeng (2002a), Seasonal and interannual variability in the distribution of surface nutrients and dissolved inorganic carbon in the Northern North Pacific: influence of El Niño, *J. Oceanogr.*, *58*(2), 227–243.

Wong, C., N. A. D. Waser, Y. Nojiri, F. A. Whitney, J. S. C. Page, and J. Zeng (2002b), Seasonal cycles of nutrients and dissolved inorganic carbon at high and mid latitudes in the North Pacific Ocean during the Skaugran cruises: determination of new production and nutrient uptake ratios, *Deep Sea Res. Part II Top. Stud. Oceanogr.*, *49*(24-25), 5317–5338, doi:10.1016/S0967-0645(02)00193-5.

Wong, C., N. A. D. Waser, F. A. Whitney, W. Johnson, and J. S. C. Page (2002c), Time-series study of the biogeochemistry of the North East subarctic Pacific: reconciliation of the Corg/N remineralization and uptake ratios with the Redfield ratios, *Deep Sea Res. Part II Top. Stud. Oceanogr.*, *49*(24-25), 5717–5738, doi:10.1016/S0967-0645(02)00211-4.

Zweng, M. M. et al. (2013), World Ocean Atlas 2013, Volume 2: Salinity, in *NOAA Atlas NESDIS 74*, vol. 2, edited by S. Levitus and A. Mishonov, p. 39.

Chapter 3

Net community production at the Kuroshio Extension Observatory and its role in the North Pacific carbon cycle

1. Introduction

1.1 Background

The sinking of photosynthetically produced carbon that is fueled by preformed nutrients in the surface ocean is one of the primary pathways of long-term carbon dioxide removal from that atmosphere [*Falkowski*, 1998]. This vertical carbon transport, commonly referred to as the biological pump, is thought to be responsible for large atmospheric carbon dioxide (CO_2) concentration changes (~100 ppm) between glacial and interglacial periods, highlighting the important link between marine primary production and climate [*Sigman and Boyle*, 2000]. Since industrialization, increasing atmospheric CO_2 levels have led to enhanced air-sea gas exchange and ocean CO_2 uptake [*Takahashi et al.*, 2009], ocean acidification [*Doney et al.*, 2009], and ocean warming [*Lyman et al.*, 2010]. Sea surface CO_2 concentrations have tracked increasing atmospheric CO_2 levels in most locations where continuous observations are available; however, some regions are beginning to deviate from the atmospheric trend, suggesting that changes in physical and/or biological processes may be occurring [*Takahashi et al.*, 2006; *Bates et al.*, 2014; *Lauvset et al.*, 2014].

The North Pacific Ocean accounts for ~25% of the total oceanic anthropogenic CO_2 uptake annually [*Takahashi et al.*, 2009]. Much of this carbon exchange occurs across a swath of the basin at the boundary between the subtropical gyre and the subarctic region (~30ºN-45ºN; Takahashi et

al. 2002; **Figure 1**) and has been attributed to geostrophic transport of water with low dissolved inorganic carbon content from the tropics northward along the Asian continent and eastward across the basin [*Ayers and Lozier*, 2012]. While physical processes largely determine the location of CO_2 uptake, biological activity has also been found to exert a significant control on the magnitude of the ocean carbon sink in this region [*Ayers and Lozier*, 2012]. Many investigators have evaluated the role of biological activity on ocean carbon uptake in the North Pacific Ocean, particularly around the transition region between the subtropical gyre and subarctic [*Wong et al.*, 2002b; *Chierici et al.*, 2006; *Takahashi et al.*, 2009; *Ayers and Lozier*, 2012; *Lockwood*, 2013; *Yasunaka et al.*, 2013]. Observations spanning multiple decades suggest that there is higher primary production in the west and lower primary production in the east, though numerous sub regions with unique dynamics have been identified [*Favorite*, 1976; *Wong et al.*, 2002b; *Chierici et al.*, 2006]. As general insights about regional variability are coming into focus, there is more need to quantitatively define baselines for biological productivity in order to determine how ocean acidification and warming may influence the efficiency of the biological pump and thus the North Pacific carbon sink [*Doney*, 2006; *Doney et al.*, 2009].

NOAA maintains two ocean time-series moorings in the North Pacific Ocean which have each collected nearly seven years of continuous, *in situ* CO_2 measurements from the sea surface and atmospheric boundary layer. These include the NOAA Kuroshio Extension Observatory (KEO), located south of the Kuroshio Extension jet, and east of Japan, as well as the NOAA Station Papa buoy, located in the eastern subarctic Pacific on the southeastern edge of the Alaska Gyre (**Figure 1**). In effort to better constrain a modern baseline for the biological pump in these regions, we have diagnostically assessed biological controls on the mixed-layer carbon inventory during each annual

deployment using a dual tracer mixed-layer mass balance approach. Detailed results of this analysis at the NOAA Station Papa mooring can be found in *Fassbender et al.*, (in prep) Here we present results from the NOAA KEO mooring and compare these to results found at Station Papa. By considering the role of biological processes on the mixed-layer carbon inventory at these two sites, we hope to better understand the regional carbon cycle dynamics within the North Pacific.

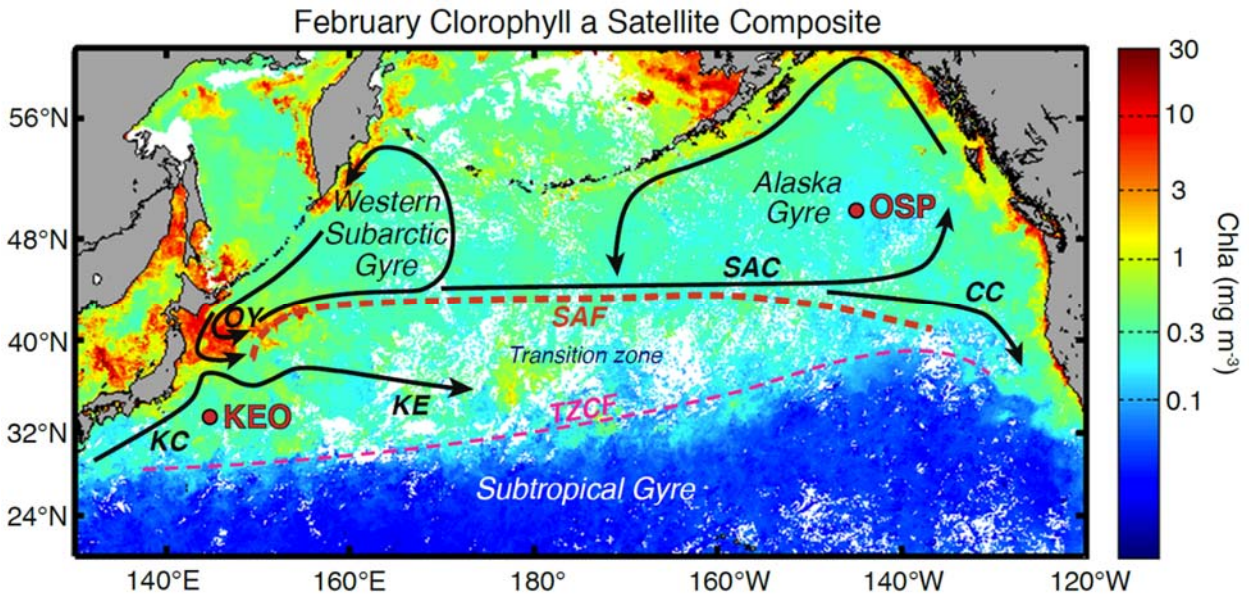

Figure 1: Map of North Pacific Ocean with the Ocean Station Papa (OSP) and the Kuroshio Extension Observatory (KEO) moorings shown. Major ocean currents including the Kuroshio Current (KE), Kuroshio Extension (KE), Oyashio Current (OY), Subarctic Current (SAC) and California Current (CC) are shown. In addition, the Western Subarctic and Alaska Gyres are depicted as well as the Subarctic Front (SAF) and Transition Zone Chlorophyll Front (TZCF). This figure is adapted from *Chierici et al.*, 2006 and *Lockwood*, 2013.

1.2 Description of KEO Study Site

The KEO mooring is located at 32.3°N, 144.6°E in a recirculation gyre just south of the Kuroshio Extension (KE) jet and east of Japan (**Figure 1**). The mooring is positioned in the center of subtropical mode water formation region where deep winter convection caused by cold air outbreaks from the Asian continent links the upper thermocline (~400m) to the atmosphere almost

annually [*Yasuda*, 2003; *Cronin et al.*, 2013; *Rainville et al.*, 2014]. Primary production at KEO is fueled by nutrients supplied during deep winter mixing. These nutrients are quickly exhausted during the spring bloom and remain near detection limits until the subsequent entrainment period [*Sukigara et al.*, 2011; *Yasunaka et al.*, 2014]. Estimates of net community production (NCP), defined here as the gross photosynthetic production minus the community respiration in the surface mixed layer, have been made in the Kuroshio-Oyashio transition zone. These range from 1.9-5.3 mol C m^{-2} yr^{-1} based on mixed-layer oxygen argon ratios [*Lockwood*, 2013], seasonal nitrate drawdown [*Wong et al.*, 2002b], and a CO_2 budgets [*Sugiura and Tsunogai*, 2005; *Chierici et al.*, 2006]; though nearly all of these estimates are north of the KEO buoy. Diatoms are thought to dominate the phytoplankton assemblage with calcium carbonate producers comprising a much smaller fraction of the annual NCP in this region [*Harrison et al.*, 2004].

The dynamic KEO mooring region oscillates between a stable state and unstable state that is thought to be modulated by large scale climate variability [*Qiu*, 2003; *Kelly et al.*, 2010; *Lin et al.*, 2014]. Unstable states are associated with southward migration of the KE jet that results in a reduced southern recirculation gyre, higher eddy activity, and negative sea surface height (SSH) anomalies. Divergent surface flow associated with this eddy activity gives rise to enhanced nutrient input and higher chlorophyll concentrations during these times [*Lin et al.*, 2014]. In the stable state, the KE jet is located farther north and the recirculation gyre is more pronounced, as evidenced by positive sea surface height (SSH) anomalies, and convergence depresses the nutricline limiting chlorophyll concentrations. This region is a strong sink for atmospheric carbon dioxide and lies in the pathway of the seasonally migrating transition zone chlorophyll front (TZCF; Ayers and Lozier 2010; Yasunaka et al. 2014, 2013). Southward migration of the TZCF in spring is due to the

convergence of horizontal Ekman nitrate flux, which stimulates primary production throughout the North Pacific transition zone; however KEO happens to reside in a region of net nitrate divergence during this time [*Ayers and Lozier*, 2010]. In addition to this unique characteristic, a recent analysis of regional carbon chemistry biomes resulted in the recirculation region just south of the KE jet getting its own designation [*Lauvset et al.*, 2014], and prior investigators have found this area to exhibit some of the highest spring NCP rates in the North Pacific Ocean [*Yasunaka et al.*, 2013]. The dynamic interplay of physics, chemistry, and biology near the KEO mooring makes this an ideal region for sustained observations to study carbon cycling.

2. Data

2.1 KEO Mooring Data

The KEO moored buoy was initiated in June 2004 at 32.3°N, 144.6°E in 5,700m depth water, south of the main jet of the Kuroshio Extension (**Figure 1**) and contributes to the global network of OceanSITES time series reference stations [*Send*, 2010]. The buoy is outfitted with a suite of meteorological, physical and biogeochemical sensors to monitor the air-sea exchanges of heat, moisture, momentum; and to monitor upper ocean temperature, salinity, oxygen and near surface currents. In 2007, a Battelle Memorial Institute MapCO_2 system that measures the mole fraction of carbon dioxide (xCO_2) in seawater and in the atmospheric boundary layer was deployed on the KEO buoy. We focus our analysis on the portion of the KEO time-series when CO_2 data are available (2007-2014) and include measurements from the buoy anemometer, current meters at 5 m, 15m, and 35 m, and multiple conductivity-temperature-depth (CTD) sensors deployed on the surface buoy and along the slack-line mooring chain to a depth of 525m. Diffusivity at the base of the mixed layer was estimated by closing the mixed-layer heat budget following Cronin et al. 2013.

The carbon budget thus relies upon numerous sensors on the mooring, each programmed to sample at different frequencies. Thus, all data have been daily averaged and centered on 12:00 Greenwich Mean Time for this analysis. Details about the specific sensors and their orientations during each deployment can be found on the Ocean Climate Stations web page (*http://www.pmel.noaa.gov/OCS/KEO/*).

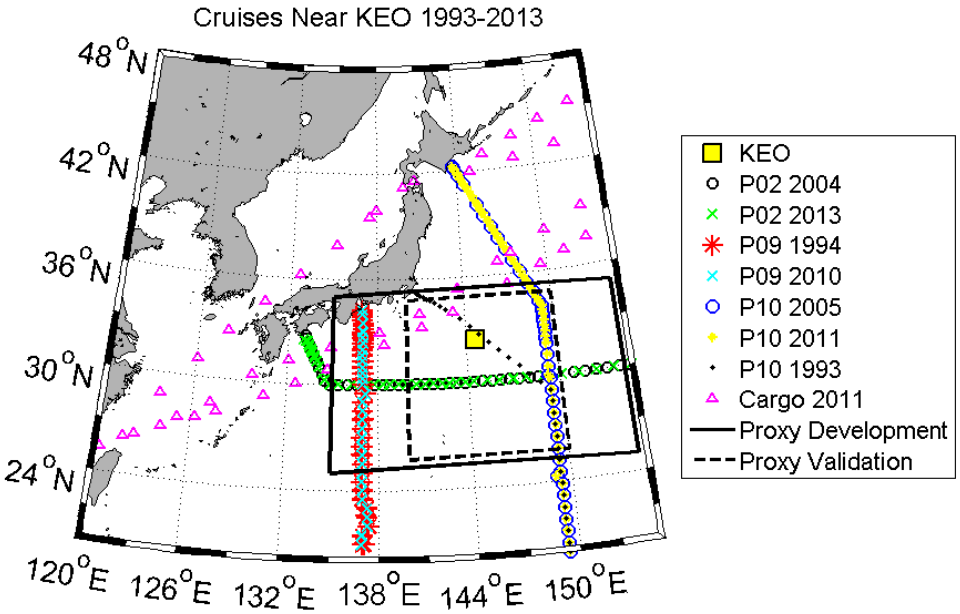

Figure 2: Map showing the NOAA KEO buoy (32.3°N, 144.6°E) and nearby station locations from select CLIVAR and WOCE repeat hydrography cruises conducted between 1993 and 2013. Samples collected from the M/V OOCL Tokyo cargo ship in 2011 are also shown (Paul Quay, unpublished). The solid lined black box surrounds stations used to develop a regional TA proxy. The dashed black box encompasses stations used for comparison with the resulting TA and DIC time-series.

2.2 Repeat Hydrography Data

Repeat hydrography cruise data that are publicly available from the Carbon Dioxide Information Analysis Center have been incorporated into the analysis. These include data from CLIVAR Line P02 in 2004 and 2013, CLIVAR/WOCE Line P09 in 2010, and CLIVAR/WOCE Line P10 in 1993, 2005, and 2011 (**Figure 2;** Kamiya et al. 2012; Swift et al. 2014; Feely et al.

2004; Murata et al. 2014; Fukasawa et al. 2005; Sabine et al. 1999). Discrete bottle samples collected near the KEO buoy (Steven Emerson, unpublished) and from the M/V OOCL Tokyo cargo ship in 2011 (Paul Quay, unpublished) as well as one degree optimally interpolated data fields from the World Ocean Atlas 2013 are also included in the analysis [*Garcia et al.*, 2013a, 2013b; *Locarnini et al.*, 2013; *Zweng et al.*, 2013]. Details about the use of these data are discussed in Sections 3.1, 3.2 and 3.4.

2.3 Satellite Data

Satellite data were used to fill in missing current meter and anemometer observations during periods of sensor malfunction or failure. This was more substantial for the current meter time-series which includes numerous short data gaps. These gaps were filled with 1/3 degree, 5 day OSCAR satellite surface currents [*Bonjean and Lagerloef*, 2002]. Periods of missing anemometer data, including one month in the fall of 2008 and five months during winter of 2010, were filled using 0.25 degree, 6 hourly, cross-calibrated multi-platform ocean surface winds from NASA [*Atlas et al.*, 2011]. Vertical velocity was estimated from the Sverdrup balance with the assumption that turbulent stress vanishes at the base of the mixed layer, using daily QuikSCAT wind stress data set prior to 2009 and ASCAT wind stress data set thereafter, and AVISO-merged anomalous Sea Surface Height (SSH) fields with the Teague et al. (1990) mean SSH field [*Bentamy and Fillon*, 2012].

3. Methods

Dissolved inorganic carbon (DIC) and Total Alkalinity (TA) are two of the four measureable carbonate system parameters used to describe the inorganic carbon chemistry of seawater. DIC is

the sum of the concentrations of carbonic acid (H_2CO_3), bicarbonate ion (HCO_3^-), carbonate ion (CO_3^{2-}), and carbon dioxide (CO_2) in aqueous solution:

$$DIC = [CO_2] + [H_2CO_3] + [HCO_3^-] + [CO_3^{2-}] \quad (\mathbf{1})$$

TA is defined as the excess of proton acceptors over proton donors and is a measure of the seawater charge balance [*Wolfgladrow et al.*, 2007].

$$TA = [HCO_3^-] + 2*[CO_3^{2-}] + [B(OH)_4^-] + [HPO_4^{2-}] + 2*[HPO_4^{3-}]\ldots + [OH^-] - [H^+] \quad (\mathbf{2})$$

In the ocean mixed layer, TA is influenced by physical transport and mixing (Phys), evaporation and precipitation (EP), and the biological processes of organic (NCP) and inorganic ($CaCO_3$) carbon production:

$$\frac{\partial TA}{\partial t} = \left.\frac{\partial TA}{\partial t}\right|_{Phys} + \left.\frac{\partial TA}{\partial t}\right|_{EP} + \left.\frac{\partial TA}{\partial t}\right|_{NCP} + \left.\frac{\partial TA}{\partial t}\right|_{CaCO_3} \quad (\mathbf{3})$$

Mixed-layer DIC is influenced by the same processes as well as air-sea carbon dioxide exchange (Gas):

$$\frac{\partial DIC}{\partial t} = \left.\frac{\partial DIC}{\partial t}\right|_{Gas} + \left.\frac{\partial DIC}{\partial t}\right|_{Phys} + \left.\frac{\partial DIC}{\partial t}\right|_{EP} + \left.\frac{\partial DIC}{\partial t}\right|_{NCP} + \left.\frac{\partial DIC}{\partial t}\right|_{CaCO_3} \quad (\mathbf{4})$$

Here we use these time-dependent mixed-layer mass-balance equations to diagnostically asses the contribution of each processes to annual changes in DIC and TA at KEO. The details of this

method are discussed more thoroughly in the *Fassbender et al.*, (in prep) analysis for the NOAA Station Papa mooring and are only briefly reviewed here.

3.1 Total Alkalinity Proxy

The simultaneous measurement of any two of the four measureable carbonate system parameters (DIC, TA, xCO_2, pH) is required to constrain seawater inorganic carbon chemistry [*Dickson and Riley*, 1978; *Millero*, 2007]. At this time, only *in situ* xCO_2 measurements are made at the KEO mooring. Without direct observations of DIC and TA, or the ability to calculate these values from a pair of *in situ* carbonate parameter measurements, an alternative approach had to be developed to estimate TA and DIC time-series. A regional salinity based TA proxy (TA = 63 × salinity + 75) was derived using data collected within 25º-35ºN and 135º-155ºE during research cruises and North Pacific cargo ship crossings (**Figure 2**). The mean mixed-layer salinity and TA values were regressed from these stations, using a mixed layer depth criterion of a 0.2ºC temperature decrease from the temperature at 10m depth [*de Boyer Montégut*, 2004]. The salinity-TA relationship was based on 59 distinct mixed-layer samples yielding a statistically significant regression with an R^2 value of 0.94 (**Figure 3**). The regional TA proxy was then applied to *in situ* salinity measurements from the KEO mooring to construct the TA time-series with a 1σ calculation uncertainty of ~7 μmol kg^{-1} (**Figure 4A**).

3.2 Calculating DIC

DIC was calculated from the TA proxy time-series and *in situ* xCO_2 measurements from the KEO mooring using the program CO_2sys [*van Heuven et al.*, 2011] with constants from Lueker et al. (2000) and Dickson (1990) (**Figure 4b).** Only a few of the discrete DIC bottle samples collected

near KEO overlap with the time-series, so a monthly DIC climatology was created from the dataset for comparison purposes. The climatology shows very good agreement with all of the discrete bottle samples collected between 2004 and 2014, indicating that our estimates accurately capture the magnitude and timing of the seasonal DIC cycle. The 1σ calculation uncertainty on the calculated DIC values is ~6 µmol kg^{-1}.

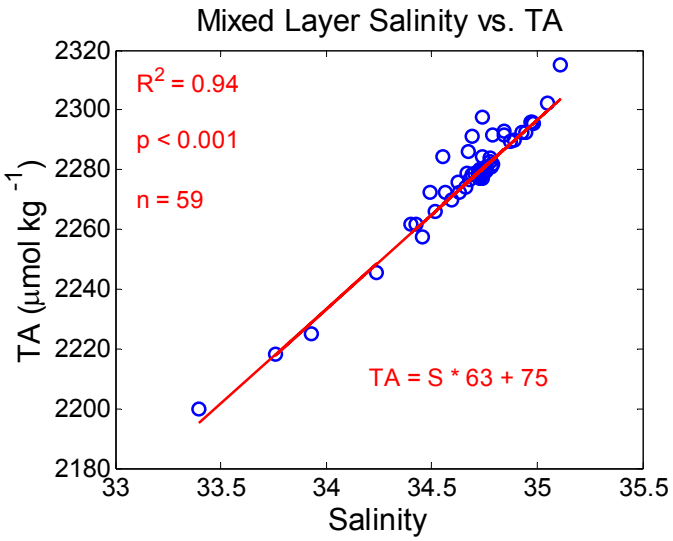

Figure 3: Mixed-layer salinity versus total alkalinity relationship derived from samples collected inside the solid lined black box in Figure 2.

3.3 Gas Exchange

Gas exchange was computed from wind speed and the difference in CO_2 partial pressure (pCO_2) between the sea surface and atmosphere (ΔpCO_2), where CO_2 partial pressure is the product of total pressure (P) and xCO_2:

$$\Delta pCO_2 = pCO_{2,\,sea} - pCO_{2,\,atm} \quad \textbf{(5)}$$

Winds measured at 4m on the KEO buoy are converted to 10m winds using the relationship of Liu et al. (1979) and are used compute the CO_2 piston velocity (k) with the Schmidt number relationship of Wanninkhof (1992) and gas transfer parameterization of Nightingale et al. (2000). The temperature and salinity dependent CO_2 solubility constant (C) of Weiss (1974) is used with the piston velocity (k) and ΔpCO_2 to compute daily air-sea CO_2 fluxes in units of mol CO_2 m^{-2} d^{-1}:

$$\left.\frac{\partial DIC}{\partial t}\right|_{Gas} = F_{t=n} = k_{t=n} \times C_{t=n} \times (\Delta pCO_{2,\,t=n}) \times 10^{-6} \quad (6)$$

The flux is divided by mixed layer depth and density, and multiplied by 10^6 to convert to units of µmol DIC kg^{-1} d^{-1}.

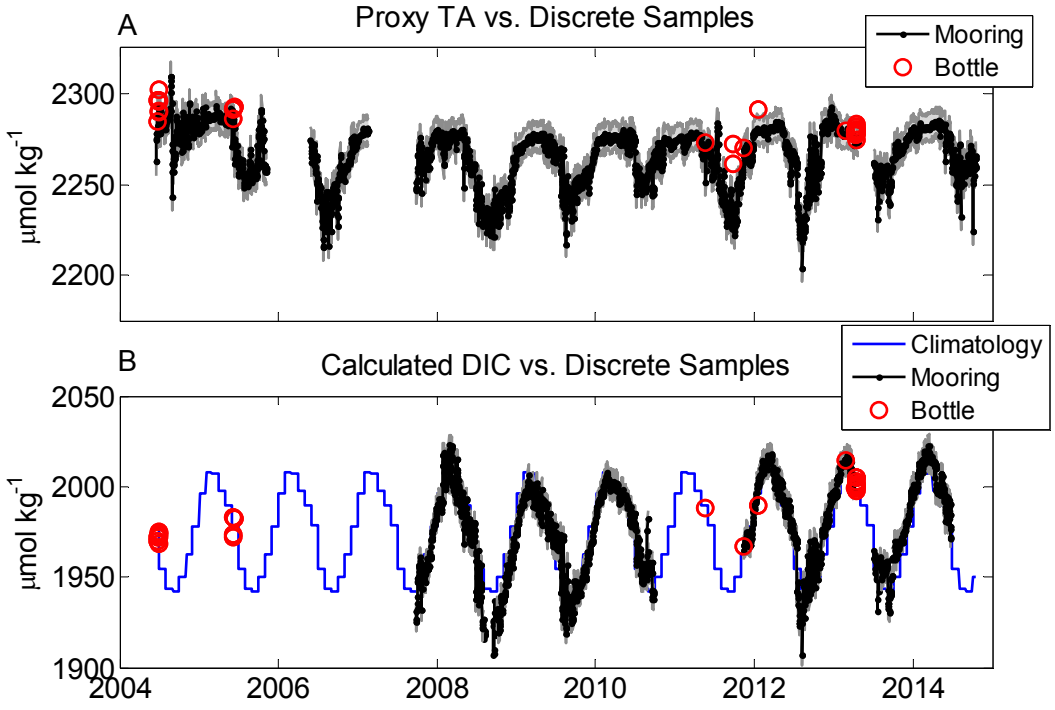

Figure 4: (**A**) Mixed-layer TA estimates from the salinity-based proxy and (**B**) DIC values computed from proxy-derived TA and *in situ* measurements of pCO_2 from the mooring using the program CO_2sys. A monthly DIC climatology derived from the all years of observations is also shown. Discrete TA and DIC bottle samples collected within the dashed black box region in Figure 2 are included for comparison.

3.4 Physical Processes

Mixed-layer DIC and TA budgets are influenced by the physical processes of advection, entrainment and detrainment, and diffusive mixing; expressed here in terms of DIC, is:

$$\frac{\partial DIC_{Phys}}{\partial t} = -u_a \cdot \nabla DIC_a - \left(w_{-h} + \frac{\partial h}{\partial t}\right)\frac{(DIC_a - DIC_{-h})}{h} - \frac{\kappa}{h}\frac{\partial DIC}{\partial z}\Big|_{z=-h} \quad (7)$$

where u_a and DIC_a are the vertically averaged horizontal velocity and DIC concentration within the mixed layer, and h is the mixed layer depth. The values w_{-h}, DIC_{-h}, κ, and $\partial DIC\ \partial z^{-1}$ are the vertical velocity, DIC concentration, diffusivity, and vertical concentration gradient all evaluated at the base of the mixed layer (h=-z). The mixed layer depth is computed as the depth where temperature decreases by 0.2ºC from the 10m temperature [*de Boyer Montégut*, 2004]. Diffusivity was estimated as the residual of the mixed-layer heat budget, evaluated for the period from June 2004-June 2009 when advection was weak [*Cronin et al.*, 2013]. In particular, the monthly climatology of heat flux across the base of the base of the mixed layer ($Q_{z=-h}$) was computed, excluding periods when advection was larger than one standard deviation. In addition, periods when $Q_{z=-h}$ was positive and greater than the surface upward heat flux, and all periods when $Q_{z=-h}$ was positive if the surface heat flux was into the ocean, were excluded. These periods were likely dominated by errors and other unresolved physics. This $Q_{z=-h}$ climatology was then divided by the climatological temperature stratification at the base of the mixed layer (estimated over the 20 m layer below the base of the mixed layer), and volumetric heat capacity of sea water. A daily time series was then computed from this monthly climatological diffusivity (**Appendix Table A.1**).

Each budget term is evaluated daily; however, continuous seasonal observations of horizontal and vertical DIC and TA gradients near KEO do not exist. To estimate monthly gradients for DIC and TA, data from repeat hydrography cruises in the region were used to develop robust multiple linear regression (MLR) relationships between DIC (and TA) and measured predictor variables in both the meridional and zonal directions. CLIVAR cruise P02 in 2013 was used for the zonal MLR construction in which temperature and oxygen were used as predictor variables for DIC and temperature and silicate were used for TA. CLIVAR cruise P10 in 2005 was used for the meridional MLR construction in which temperature and phosphate were used as predictor variables for DIC and silicate and latitude were used for TA. The regression coefficients were then applied to 2013 World Ocean Atlas (WOA) monthly climatologies of the predictor variables to produce monthly DIC and TA fields. Horizontal and vertical concentration gradients were then computed from these fields.

3.5 Evaporation-Precipitation

Mixed-layer salinity is influenced by evaporation and precipitation (EP) as well as the physical processes described in the previous section. We estimate the influence of physical processed using gradients derived from the WOA 2013 salinity fields in the meridional and zonal directions and equation **7**. Subtracting the physical contribution to the salinity budget from the observed change in salinity with time gives the EP term:

$$\left.\frac{\partial Sal}{\partial t}\right|_{EP} = \left.\frac{\partial Sal}{\partial t}\right| - \left.\frac{\partial Sal}{\partial t}\right|_{Phys} \quad \textbf{(8)}$$

The EP term is multiplied by the DIC:salinity and TA:salinity ratio at the start of the deployment (*t=1*) to scale to units of μmol kg^{-1} d^{-1}:

$$\left.\frac{\partial DIC}{\partial t}\right|_{EP} = \left.\frac{\partial Sal}{\partial t}\right|_{EP} \times \left.\frac{DIC}{Sal}\right|_{t=1} \quad (9)$$

3.6 NCP and $CaCO_3$ Processes

With estimates of gas exchange, physical, and EP processes, only the biological terms (NCP and $CaCO_3$) must be solved for, leaving two equations and four unknowns:

$$\left.\frac{\partial DIC}{\partial t}\right|_{Bio} = \left.\frac{\partial DIC}{\partial t}\right|_{NCP} + \left.\frac{\partial DIC}{\partial t}\right|_{CaCO_3} \quad (10)$$

$$\left.\frac{\partial TA}{\partial t}\right|_{Bio} = \left.\frac{\partial TA}{\partial t}\right|_{NCP} + \left.\frac{\partial TA}{\partial t}\right|_{CaCO_3} \quad (11)$$

DIC and TA are influenced by NCP and $CaCO_3$ processes at well-known stoichiometric ratios [*Anderson and Sarmiento*, 1994], making it possible rearrange equations **10** and **11** to get two equations and two unknowns (not shown) and thus close the budget:

$$\left.\frac{\partial \mathrm{DIC}}{\partial \mathrm{t}}\right|_{\mathrm{NCP}} = \frac{\left(\left.\frac{\partial \mathrm{TA}}{\partial \mathrm{t}}\right|_{\mathrm{Bio}} - 2 \times \left.\frac{\partial \mathrm{DIC}}{\partial \mathrm{t}}\right|_{\mathrm{Bio}}\right)}{\left(-2 + \frac{-17}{117}\right)} \quad (12)$$

The above methodology relies upon closing the DIC and TA budgets. Because the residual also contains the accumulation of all errors in the analysis, a careful accounting of uncertainties is necessary. Manufacturer stated instrument errors were propagated through each of the calculations

in this analysis using standard error propagation techniques. When computations were nonlinear or complex, a Montel Carlo approach was used in which input parameters for a given calculation were stochastically varied around their uncertainties in a Gaussian manner (~3σ) for 500 iterations of the calculation. The standard deviation of the 500 resultant values was then used as the uncertainty estimate for the calculated parameter. Readers are referred to **Appendix** as well as *Fassbender et al.*, (in prep) for details about the uncertainty in each budget term.

The largest uncertainty in the budget analysis comes from parameterization of the physical processes, and primarily from determination of vertical gradients at the base of the mixed layer (**Figure A.1**). Uncertainties in the gradients coupled with uncertainties in the mixed layer depth (~6-16%) and turbulent diffusion (~20-92%) give rise to 68% error bounds on the daily physical flux terms (μmol kg^{-1} d^{-1}) that are often larger than 100% (**Appendix Tables A.1**, **A.2**). Cumulatively summing the daily fluxes over each annual deployment reduces these errors dramatically through the propagation of errors by summing in quadrature, leading to the 68% uncertainty bounds shown in **Figures 5** and **6**. We believe that our uncertainty assessment is highly conservative as hydrographic cruise data in the region agree with the sign and general seasonality of the vertical salinity, DIC and TA gradients derived herein.

4. Results

4.1 Mixed-Layer Budget Evaluations

The KEO mooring was replaced in September or October of each year, making October 1 a logical start date (*t=1*) for the annual mixed-layer budget evaluations. The total change in mixed-layer DIC and TA with time is calculated by subtracting the concentration on October 1 from all

subsequent measurements made during the deployment. This yields a time-series of the cumulative mixed-layer DIC and TA change with time in units of µmol kg^{-1}. Each of the process specific budget terms, computed in units of µmol kg^{-1} d^{-1}, was integrated in time from the start of the deployment through the duration of data collection, giving the cumulative mixed-layer DIC and TA changes for each process in units of µmol kg^{-1} (**Figures 5, 6; Table 1)**.

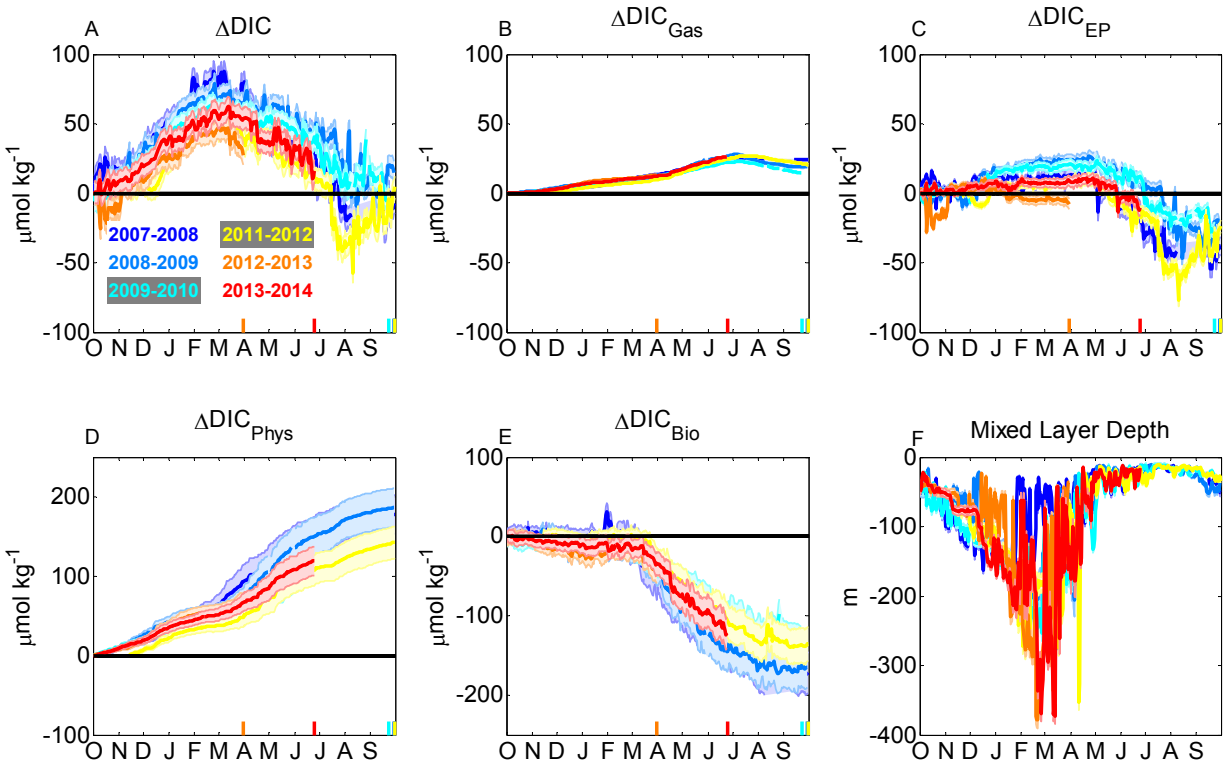

Figure 5: Results from the DIC budget analysis for individual KEO deployment years (colors) with 68% uncertainty bounds. (**A**) Mixed-layer DIC concentration change relative to October 1 and the cumulative influences of (**B**) gas exchange, (**C**) EP, (**D**) physical processes, and (**E**) biological processes in units of µmol kg^{-1}. (**F**) Mixed layer depth. Colored lines at the bottom of each plot show the last day of observations in each annual mooring deployment.

The amplitude of seasonal mixed-layer DIC change at KEO is ~97 ± 21 µmol kg^{-1}. The DIC concentration increases from August through February each year and begins to decline in March. The region is undersaturated with respect to CO_2 throughout the year excluding a few months at

the end of summer, causing net CO_2 gas invasion that adds ~20 ± 4 μmol DIC kg^{-1} to the mixed layer annually. KEO is in a region of high seasonal evaporation and precipitation. During fall and winter, cold, dry air from the Asian continent moves over the Kuroshio Current region picking up heat and moisture, causing evaporation [*Kelly et al.*, 2010]. In spring and early summer, heavy precipitation brings excess freshwater to the region leading to net annual precipitation that dilutes mixed-layer DIC by ~-28 ± 7 μmol kg^{-1}.

Physical mixing processes dominate the mixed-layer budget, adding ~162 ± 24 μmol kg^{-1} primarily through the vertical process of entrainment (~34%) and diffusive mixing (~64%). Horizontal advection of DIC was found to be small, though warm core eddies that spin off of the Kuroshio Extension are occasionally advected into the KEO mooring region [*Yasuda*, 2003], as evidenced by periods of very high current speeds (~100 cm s^{-1}) that switch meridional and zonal directions as the eddy passes. The negligible role of advection in our budget is surprising, and is likely due to the fact that our methodology does not resolve intermittent carbon gradients induced by eddies. However, there is no correlation between the DIC time-series and mixed-layer current speed, which may indicate that warm core eddies do not influence the DIC budget significantly through advection, though high frequency variability in the TA and DIC time series may be evidence of some advective transport (**Figure 4**). Additionally, the KEO mooring is located in the recirculation gyre, just south of the Kuroshio jet. As such, its properties are somewhat homogenous in comparison to the highly advective region of the KE jet.

Subtracting the Gas, EP and Physical budget components from the observed mixed-layer DIC changes gives the residual biological term (Bio). This term is similar in magnitude to the physical

budget term, showing the dramatic influence of biology (~-151 ± 20 µmol kg^{-1}) on mixed-layer DIC concentration from March through September of each year.

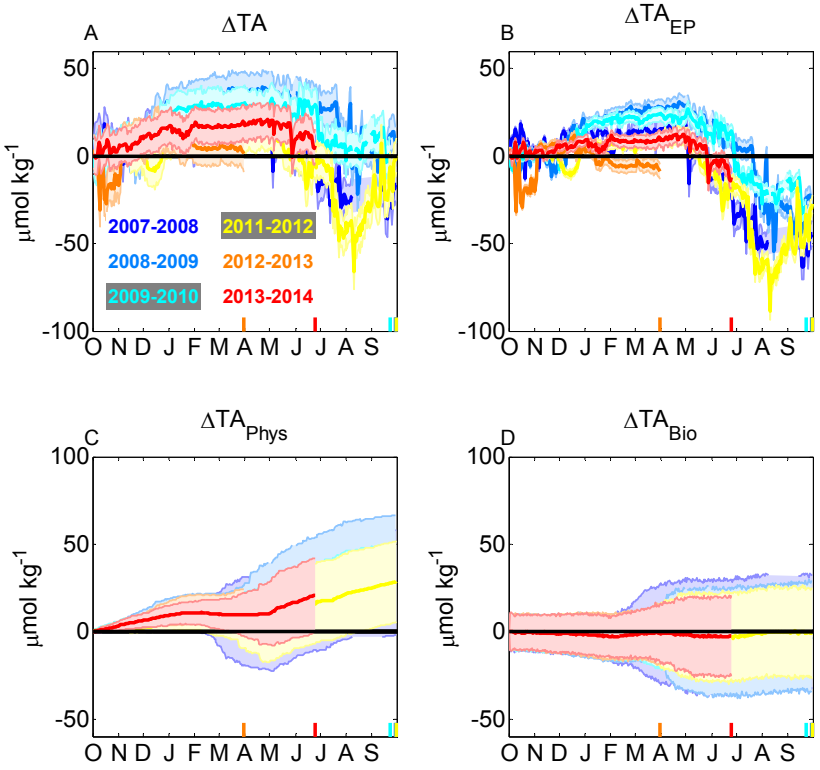

Figure 6: Results from the TA budget analysis for individual KEO deployment years (colors) with 68% uncertainty bounds. (**A**) Mixed-layer TA concentration change relative to October 1 and the cumulative influences of (**B**) EP, (**C**) physical processes, and (**D**) biological processes in units of µmol kg^{-1}. Colored lines at the bottom of each plot show the last day of observations in each annual mooring deployment.

The seasonal cycle of mixed-layer TA is similar to that of DIC but is about 60% of the magnitude (~61 ± 17 µmol TA kg^{-1}; **Table 2**). TA concentrations increase from August through February and decline abruptly in June or July as the rainy season starts. Net precipitation dilutes mixed-layer TA concentrations by ~-33 ± 8 µmol kg^{-1}, which is similar in magnitude to the physical component of the TA budget (~32 ± 5 µmol kg^{-1}), indicating that TA is primarily controlled by these two processes, which is most notable in summer when the mixed layer depth is shallow. Subtracting the EP and physical budget components from the observed mixed-layer TA

changes gives the residual biological TA term, which is small (~-1 ± 1 μmol kg^{-1}) and indistinguishable from zero (**Figure 6D**).

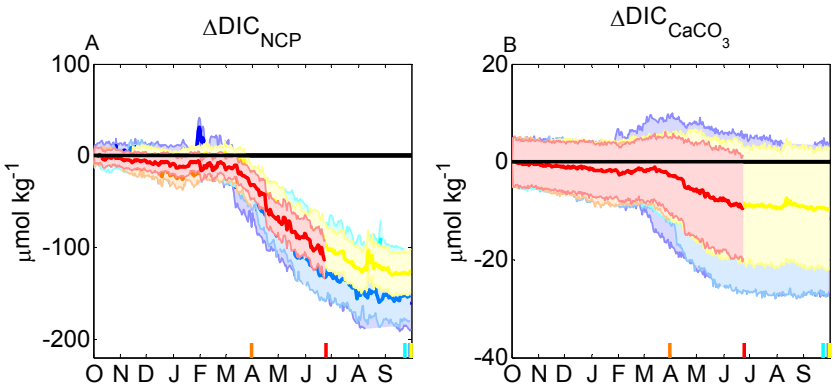

Figure 7: The cumulative influence of (**A**) NCP and (**B**) $CaCO_3$ process on the mixed-layer DIC concentrations. Colored lines at the bottom of each plot show the last day of observations in each annual mooring deployment.

4.2 NCP and $CaCO_3$

The biological DIC term is decomposed into NCP and $CaCO_3$ processes using equation **12** to close the budget and **10** to solve for DIC_{CaCO3} (**Figure 7**). The results show that NCP dominates the biological mixed-layer DIC drawdown (~-140 ± 19 μmol kg^{-1}) at KEO, with $CaCO_3$ process contributing minimally (~-11 ± 3 μmol kg^{-1}). Similarly high DIC concentration drawdowns (-160 μmol kg^{-1}) associated with aNCP have been observed north of the KE jet in the Oyashio region off Hokkaido, highlighting the importance of biology in carbon cycling throughout the region [*Ono et al.*, 2005]. While the annual impact of NCP is large, there is no discernable influence of NCP on the mixed-layer DIC budget in fall and winter. Only in March is there a sudden decrease in mixed-layer DIC due to organic carbon production, as well as a much smaller accompanying draw down of DIC due to calcification. After June, there is little change in the NCP and $CaCO_3$ production.

In addition to seasonality, the NCP at KEO is variable between years while the $CaCO_3$ production appears consistent. To evaluate these differences quantitatively, seasonal and interannual variability in the mixed layer depth must be taken into consideration. This was accomplished by computing the derivatives of the DIC_{NCP} and DIC_{CaCO3} terms and multiplying by the mixed layer depth, density, and 10^{-3} to convert to units of mmol C m^{-2} d^{-1}. The resulting daily NCP and $CaCO_3$ rates are shown in **Figure 8A-B** and have been smoothed with a 30 day moving average to highlight monthly variations. Negative NCP rates reflect net biological DIC consumption (autotrophy) and positive values reflect net biological DIC production (heterotrophy). Negative $CaCO_3$ production rates reflect net calcification while positive values indicate net dissolution. We calculate the cumulative column inventory of NCP with time by integrating the unsmoothed daily rates and multiplying by 10^{-3} to scale to units of mol C m^{-2} (**Figure 8C-D**). Averages are computed at each time step to give a mean rate and cumulative column inventory, shown by the black lines in **Figures 8A-D**. The last cumulative NCP value for each deployment represents the annual NCP and represents an upper limit on the surface ocean carbon export annually. These values and the associated uncertainty estimates are given in **Table 3** and range from -2.2 ± 3.7 to -11.0 ± 3.1 mol C m^2 yr^{-1} for deployments where observations were collected over the entire annual cycle (2007-2008, 2008-2009, 2009-2010, 2011-2012). The average aNCP (-4.5 ± 2.2 mol C m^2 yr^{-1}) listed in **Table 3** excludes the 2007-2008 deployment during which a cyclonic eddy surrounding the mooring lead to anomalously high aNCP values, which will be discussed later. Annual $CaCO_3$ production values from the four full year deployments range from -0.2 ± 2.1 to -0.9± 1.5 mol C m^2 yr^{-1} with a mean $aCaCO_3$ value of -0.4 ± 1.1 mol C m^2 yr^{-1} (excluding 2007-2008). This gives a mean annual particulate inorganic carbon

to organic carbon ratio of 0.1 ± 0.3, which is similar to the global average [*Sarmiento et al.*, 2002; *Jin et al.*, 2006].

5. Discussion

5.1 Controls on NCP at KEO

The results of this analysis indicate that the KEO mooring is located in a region of high annual NCP with a large range of interannual variability (~50%). There is almost no NCP in late summer at the KEO mooring, likely due to nutrient limitation in this region, as evidenced by nitrate concentrations lower than 1 μmol kg^{-1} during the summer CLIVAR cruises P09 in 2010 and P02 in 2004 [*Feely et al.*, 2004; *Kamiya et al.*, 2012] and a recent evaluation of seasonal nutrient drawdown in this region [*Yasunaka et al.*, 2014]. As the mixed layer deepens from September to December there is little change in the cumulative NCP. Further deepening from ~125m in January to ~300m in February causes the cumulative NCP increase to ~1 mol C m^{-2}, reflecting net heterotrophy; however, this is not statistically significant (**Appendix Figure A.2A**). As the mixed layer shoals in March, organic carbon production causes the cumulative NCP to decline from ~1 mol C m^{-2} to ~-3 mol C m^{-2} by the end of May (in the composite), reaching NCP rates of ~-60 mmol C m^{-2} d^{-1} (**Figure 8A**). Similarly high daily NCP rates have been found by other investigators during the spring bloom in this region [*Sugiura and Tsunogai*, 2005; *Lockwood*, 2013; *Yasunaka et al.*, 2013]; however, the extremely high rates (<-200 mmol C m^{-2} d^{-1}) and aNCP (-11.1 ± 3.1 mol C m^{-2}) observed during the 2007-2008 deployment are, to the best of our knowledge, unprecedented in this region. There is little NCP after June as the mixed layer thermally stratifies and nutrients become limiting.

Table 1. Results from the DIC budget analysis at Station Papa and the Kuroshio Extension Observatory. Deployments with observations covering the entire year (highlighted in grey and blue) are included in the mean and standard deviation calculations.

	DIC Seasonal Amp.		ΔDIC_{Total}		ΔDIC_{Gas}		ΔDIC_{EP}		ΔDIC_{Phys}		ΔDIC_{NCP}		ΔDIC_{CaCO3}		Maximum MLD	
	($\mu mol\ kg^{-1}$)		($\mu mol\ kg^{-1}$)		($\mu mol\ kg^{-1}$)		($\mu mol\ kg^{-1}$)		($\mu mol\ kg^{-1}$)		($\mu mol\ kg^{-1}$)		($\mu mol\ kg^{-1}$)		(m)	
Year	**Papa**	**KEO**	**Papa**	**KEO**	**Papa**	**KEO**	**Papa**	**KEO**	**Papa**	**KEO**	**Papa**	**KEO**	**Papa**	**KEO**	**Papa**	**KEO**
2007-2008	65	116	14	-7	5	24	-15	-38	96	178	-65	-160	-7	-12	103	172
2008-2009	65	88	-29	15	21	19	-13	-25	38	186	-71	-152	-4	-12	56	278
2009-2010	66	71	22	-2	19	15	-11	-26	68	140	-48	-121	-6	-10	113	253
2010-2011	68		6	0	17		-21		107		-90		-8		84	
2011-2012	62	111	17	4	3	21	-14	-24	91	143	-57	-126	-7	-10	121	352
2012-2013	68	72	21	28	14	13	-15	-8	66	67	-40	-41	-4	-4	120	378
2013-2014	50	63	-4	16	0	26	-12	-10	58	119	-55	-112	-4	-9	62	373
Mean	65	97	10	3	11	20	-18	-28	101	162	-77	-140	-8	-11	94	264
StDev.	3	21	6	9	9	4	4	7	8	24	18	19	1	1	14	74

Table 2. Results from the TA budget analysis at Station Papa and the Kuroshio Extension Observatory. Deployments with observations covering the entire year (highlighted in grey and blue) are included in the mean and standard deviation calculations.

	TA Seasonal Amp.		ΔTA_{Total}		ΔTA_{EP}		ΔTA_{Phys}		ΔTA_{NCP}		ΔTA_{CaCO3}	
	($\mu mol\ kg^{-1}$)		($\mu mol\ kg^{-1}$)		($\mu mol\ kg^{-1}$)		($\mu mol\ kg^{-1}$)		($\mu mol\ kg^{-1}$)		($\mu mol\ kg^{-1}$)	
Year	**Papa**	**KEO**	**Papa**	**KEO**	**Papa**	**KEO**	**Papa**	**KEO**	**Papa**	**KEO**	**Papa**	**KEO**
2007-2008	10	60	3	-16	-16	-44	24	28	9	23	-15	-23
2008-2009	6	61	-4	7	-14	-29	9	39	10	22	-9	-25
2009-2010	10	40	2	0	-12	-30	18	32	7	18	-11	-20
2010-2011	9		0		-22		26		13		-16	
2011-2012	10	81	2	0	-15	-27	23	29	8	18	-14	-19
2012-2013	8	50	-1	1	-16	-9	18	12	6	6	-8	-8
2013-2014	9	22	-2	6	-13	-12	11	21	8	16	-8	-19
Mean	10	61	1	-2	-19	-33	25	32	11	20	-15	-22
StDev.	1	17	2	10	5	8	1	5	3	3	1	3

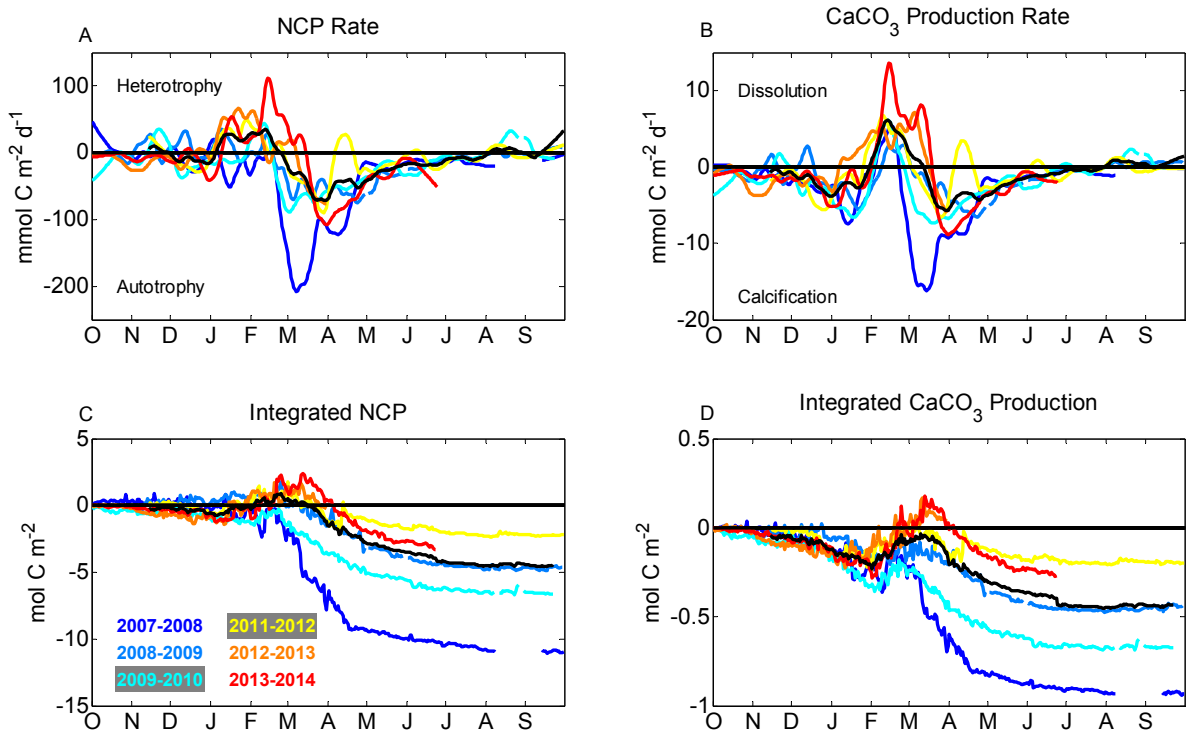

Figure 8. Daily (**A**) NCP and (**B**) $CaCO_3$ rates smoothed with a 30 day moving filter. Integrated (**B**) NCP and (**D**) $CaCO_3$ rates. Black lines show the mean of all years.

Interannual variability in the aNCP at KEO is approximately 50% of the mean value, and the magnitude of aNCP is highly anticorrelated (R^2 = -0.88, $p<0.001$) with the depth of the winter mixed layer, highlighting the importance of vertical processes in this region. The amount of NCP achievable in the mixed layer is largely the function of two processes. The first is the extent of overlap between nutrient and light availability. Deeper winter mixing results in higher nutrient concentrations throughout the mixed layer; however, the ability of phytoplankton to utilize these nutrients depends on the duration of light availability that overlaps with nutrient availability, and, thus, the rate of spring mixed-layer shoaling. Second, the depth of winter mixing influences the amount of carbon able to escape the surface ocean annually. If NCP in the photic zone were constant, interannual variability in the winter mixed-layer depth would alter the overall aNCP simply by re-entraining different amounts of carbon exported from the photic zone each year. A

balance between these dynamics at KEO, where there is a large amount of variability in the maximum winter mixed layer depth (264 ± 74 m), leads to the strong relationship between vertical processes and aNCP.

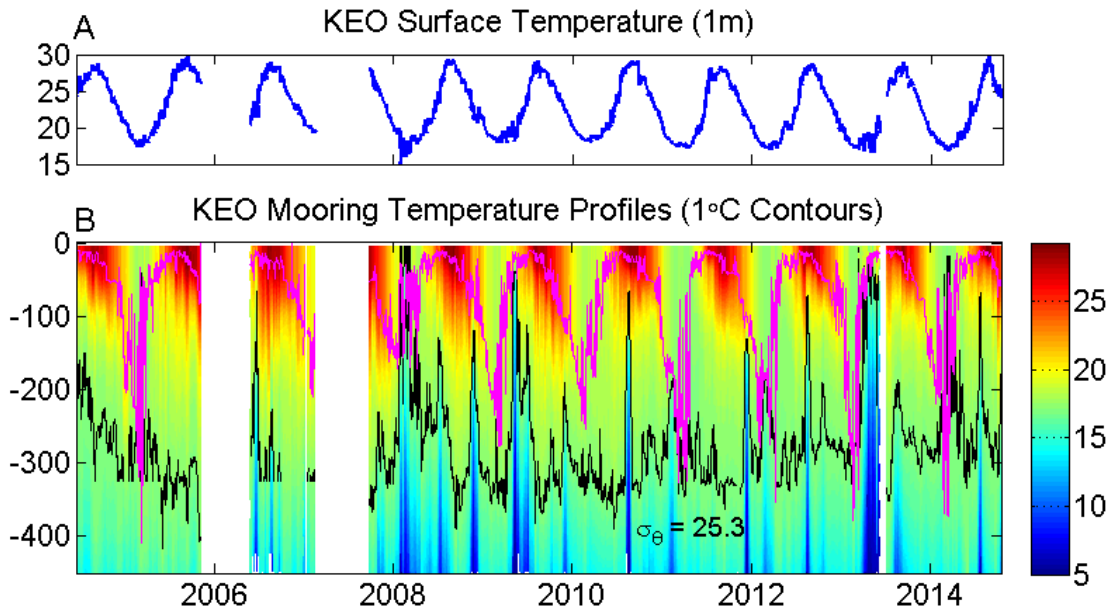

Figure 9. (**A**) Sea surface (1m) temperature and (**B**) subsurface temperature profiles at KEO mooring from 2004 to 2014. The 25.3 sigma theta (σ_θ) surface is contoured in black and mixed layer depth is shown in magenta.

The 2007-2008 deployment is an excellent example of the vertical controls on aNCP at KEO. During this deployment, the winter mixed layer was notably shallower than other deployments (**Table 1**), and winter sea surface temperatures were the coldest in the entire 10 year time-series (**Figures 9A**). Vertical temperature profiles from the mooring indicate that deep, cold waters from >400m were ventilating at the sea surface during winter of 2007-2008 creating a strong vertical temperature gradient (**Figure 9B**). Thus, even though there was a relatively shallow thermal mixed layer, the waters that were entrained came from much deeper within the mode water layer than usual. Nutrient concentrations increase with depth in this region [*Garcia et al.*, 2013b], so the high nutrient input combined with enhanced light availability in the shallow mixed layer likely fueled

the anomalous production observed in this year. In addition to high nutrient and light availability, carbon only had to escape the top 172m of the water column to contribute to aNCP during this year, whereas in all other years carbon had to escape at least the top ~250m of the water column due to deeper winter entrainment (**Table 1**). Therefore, the winter mixed layer depth is an important consideration in the interpretation of interannual variability in aNCP.

The Kuroshio Extension (KE) region is known to oscillate between two states that are thought to be controlled by anomalies in wind stress curl in the northeast Pacific Ocean that are correlated with the Pacific Decadal Oscillation (PDO; Qiu 2003; Kelly et al. 2010). Fluctuations between these states occur on decadal time scales and have recently been linked to variably in NCP [*Lin et al.*, 2014]. During negative PDO phases, the KE jet is weakened and located south of its mean position. This destabilizes the southern recirculation gyre and leads to higher eddy activity that is associated with higher chlorophyll concentrations and NCP as a result of enhanced nutrient supply [*Lin et al.*, 2014]. To assess the influence of eddy activity on the aNCP estimates derived herein, AVISO-merged weekly sea surface height anomalies (SSHa) near 145ºE and 32ºN were evaluated. During the spring productive periods of 2008 and 2013 SSH was low relative to the other deployment years (**Figure 10**; *Teague et al.*, 1990). SSHa maps confirmed the presence of cyclonic eddies centered near the KEO mooring during February of 2008, at the start of the spring bloom, as well as in April of 2013, at the tail end of the spring bloom. This confirms that the anomalous production during 2008 was likely fueled by enhanced nutrient supply from a cyclonic eddy centered at KEO that overlapped in timing with the seasonal spring bloom and which led to unusually shallow mixed layer depths. In 2013, the cyclonic eddy appeared after the peak productive period and deep waters do not appear to have breached the mixed layer or to have

influenced the aNCP, though data are lacking after July 2013 (**Figure 9B**; **Table 3**). We exclude the 2007-2008 deployment from our average NCP and $CaCO_3$ production estimates due to the irregular conditions observed during this year.

Table 3. Annual NCP and $CaCO_3$ production at Station Papa and the Kuroshio Extension Observatory for each deployment year. Deployments with observations covering the entire year (highlighted in grey and blue) are included in the means. The error estimate for the mean is shown, not the standard deviation.

	NCP mol C m^{-2} yr^{-1}		$CaCO_3$ mol C m^{-2} yr^{-1}		NCP mol C m^{-2} yr^{-1}		$CaCO_3$ mol C m^{-2} yr^{-1}	
Year	**Papa**	**Error**	**Papa**	**Error**	**KEO**	**Error**	**KEO**	**Error**
2007-2008	-1.8	0.8	-0.4	0.4	-11.0	3.1	-0.9	1.5
2008-2009	-1.4	0.3	-0.1	0.2	-4.6	4.3	-0.4	2.1
2009-2010	-0.4	0.6	-0.3	0.3	-6.6	3.3	-0.7	1.6
2010-2011	-2.1	0.6	-0.4	0.3				
2011-2012	-1.8	0.8	-0.4	0.4	-2.2	3.7	-0.2	2.1
2012-2013	0.3	0.5	-0.2	0.3	-0.2	4.2	0.0	2.1
2013-2014	-0.6	0.3	-0.1	0.2	-3.3	4.3	-0.3	2.5
Mean	-1.9	0.5	-0.4	0.2	-4.5	2.2	-0.4	1.1

Coccolithophores have been observed near the Kuroshio Extension as well as the Western Subarctic Gyre but are believed to comprise a small fraction of the NCP [*Harrison et al.*, 2004]. The $CaCO_3$ production analysis herein is not statistically significant due to computational uncertainties; however, the results suggest that $CaCO_3$ production at KEO is largest in spring. There appears to be a period of dissolution during winter, which is surprising. The depth at which the calcium carbonate polymorph aragonite becomes thermodynamically unstable, commonly referred to as the aragonite saturation horizon, is located at ~700m [*Feely*, 2002]; well below the isothermal mode water layer. Thus, a $CaCO_3$ dissolution signal may be due to noise in the computation, or possibly due to the dissolution of more soluble high-magnesian calcites, dissolution of aragonite or calcite within biologically mediated microenvironments with elevated CO_2 levels [*Milliman et al.*, 1999], or may be a signal transported from coastal regions [*Chen*,

2002]. Calcification is observed from March through June and stagnates shortly after, likely due to nutrient limitation that also limits NCP at this time of year.

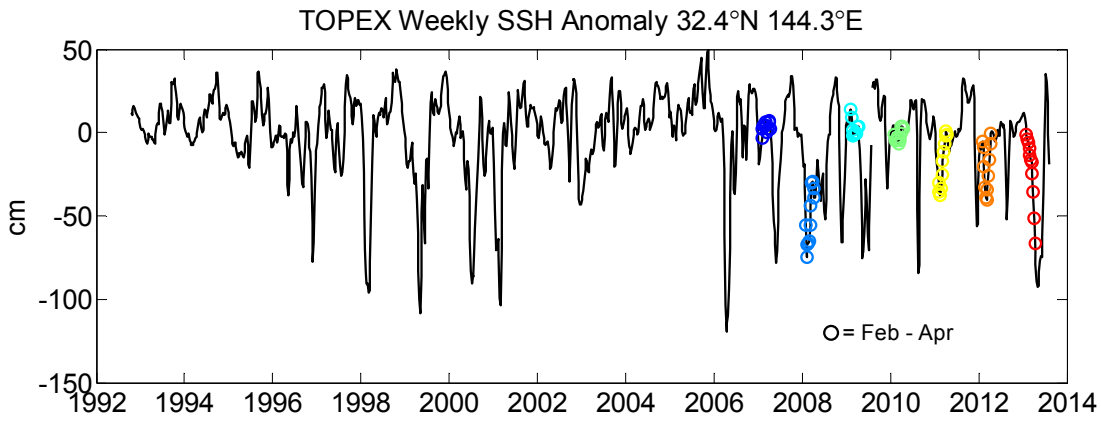

Figure 10. Weekly sea surface height anomalies (SSHa) at 144.3ºC and 32.4ºN from the AVISO-merged satellite product. The spring productive period at KEO (February through April) is highlighted for each year by the colored circles.

5.2 Comparison of KEO and OSP

Ocean Station Papa is located at 50°N, 145°W in the eastern subarctic Pacific Ocean in a high nutrient low chlorophyll region. Observations from this location date back to the 1950's and continue through present via hydrographic cruises that occur 2-3 times per year [*Freeland*, 2007]. Productivity at Ocean Station Papa (OSP) follows seasonal irradiance [*Timothy et al.*, 2013] and is ultimately limited by iron availability [*Martin and Fitzwater*, 1988; *Boyd et al.*, 2004], which may be relieved by numerous processes [*Harrison et al.*, 2004], including: seasonal entrainment, eddy iron transport, advection of iron rich Alaska Stream waters, and dry deposition. This region is known for occasional high concentrations of calcifying phytoplankton [*Wong et al.*, 2002a; *Lipsen et al.*, 2007], which are generally most abundant near the end of spring and can dominate the phytoplankton community causing particulate inorganic to organic carbon ratios to exceed one [*Wong et al.*, 2002c; *Lipsen et al.*, 2007; *Emerson et al.*, 2011; *Timothy et al.*, 2013]. Sea surface

CO_2 concentrations are generally below atmospheric levels at OSP, making this region a sink for atmospheric CO_2 (**Figure 11A**).

The same dual tracer mixed-layer budget analysis was conducted at the NOAA Station Papa mooring (**Table 1**). The mean aNCP at OSP was ~1.9 ± 0.5 mol C m^{-2} yr^{-1}, and agreed well with prior estimates [*Takahashi et al.*, 1993; *Wong et al.*, 1995, 2002a, 2002c; *Emerson and Stump*, 2010; *Giesbrecht et al.*, 2012; *Juranek et al.*, 2012]. Interannual variability in aNCP was found to be low [*Fassbender et al.*, in prep]; however, seasonal anomalies associated with stochastic events [*Hamme et al.*, 2010] and climate variability have been observed [*Wong et al.*, 2002a; *Lipsen et al.*, 2007]. NCP is largest in spring and summer and continues at lower levels through winter as evidenced by sediment trap studies [*Wong et al.*, 1999; *Harrison et al.*, 2004; *Timothy et al.*, 2013], though chlorophyll concentrations are consistently low throughout the year [*Wong et al.*, 1995]. This region is not known for having a spring bloom; however, prior studies [*Bishop et al.*, 1999; *Chierici et al.*, 2006] and our recent analysis [*Fassbender et al.*, in prep] suggest that spring production may contribute significantly to the annual NCP. There is a strong seasonality to the NCP at OSP due to heterotrophy that occurs in fall and winter, likely caused by the remineralization of dissolved organic carbon (DOC) remaining in the water column after spring and summer production [*Fassbender et al.*, in prep]. The depth of winter entrainment is constrained by the halocline "barrier layer" in the region, leading to low interannual variability in the winter mixed-layer depth (~14m). The mean a$CaCO_3$ production was estimated to be ~0.4 ± 0.2 mol C m^{-2} yr^{-1}, giving an annually integrated PIC:POC production ratio of 0.21 ± 0.1, which is similar to comparable multi-years estimates at this site [*Wong et al.*, 2002c; *Timothy et al.*, 2013]. The contrast between sustained, low production observed at OSP and the vigorous spring production

found near KEO make these regions ideal places to study the interplay of physics, chemistry, and biology on regional carbon cycling.

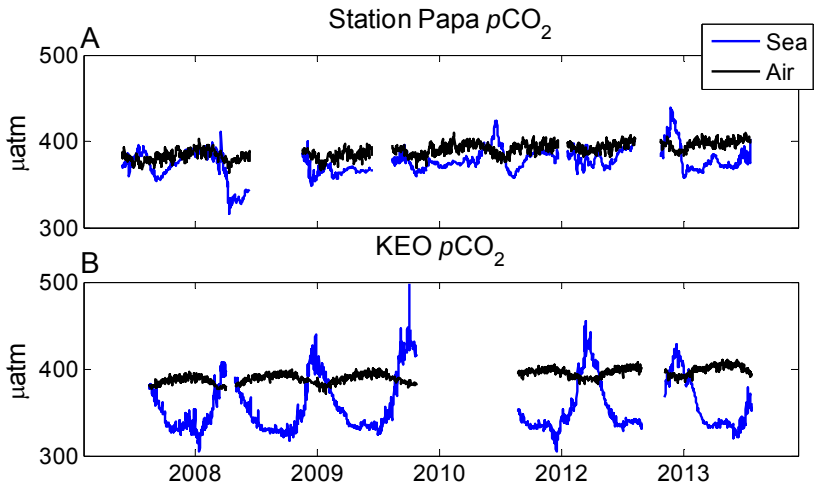

Figure 11: The partial pressure of carbon dioxide (pCO_2) in seawater and the atmospheric boundary layer at NOAA Station Papa and the Kuroshio Extension Observatory.

KEO and OSP exhibit clear seasonal DIC and TA cycles with the highest concentrations in winter due to the entrainment of deeper waters. DIC concentrations are ~50 µmol kg^{-1} higher at OSP than KEO but the seasonal DIC change at OSP (~65 ± 3 µmol kg^{-1}) is lower than that at KEO (~97 ± 21 µmol kg^{-1}; **Table 1**). TA concentrations are ~80 µmol kg^{-1} higher at KEO than at OSP and the seasonal TA cycle at KEO (~61 ± 17 µmol kg^{-1}) is six times larger than at OSP (~10 ± 1 µmol kg^{-1}; **Table 2**). Physical processes dominate the mixed-layer DIC budgets at both locations with NCP being the secondary contributor at each site (**Table 4**). EP and gas exchange play similar roles in terms of percentage of carbon change at each site, with calcium carbonate contributing least in both locations. OSP is known for occasionally high coccolithophore abundances as well as the presence of pteropods and foraminifera [*Wong et al.*, 1999], and although OSP and KEO have the same magnitude of annual $CaCO_3$ production (**Table 3**), it comprises a much larger fraction of the aNCP at OSP (~20%) than at KEO (~10%). The larger contribution of $CaCO_3$

processes at OSP is not surprising as a linear regression of mixed-layer TA versus salinity near the OSP mooring yields a line with a slope of 37, while at KEO this line has a slope of 63 (**Figure 3**). The freshwater dilution line for both regions has a slope of ~66. Since the slope of the TA-salinity relationship at KEO is nearly equal to the dilution-line slope, this suggests that TA variations in this region are almost entirely caused by EP and physical processes. At OSP, the significant deviation in slope of TA-salinity relationship from the dilution-line slope suggests that $CaCO_3$ processes must play an important role in the TA variability at this location, in addition to the influences of EP and physical processes.

Table 4. Mean percentage contribution of each process to the annual mixed-layer DIC transformation at KEO and OSP. The total mixed-layer DIC transformation is the sum of absolute values of the mean annual process contributions in Table 1. Standard deviations are also given in percent relative to the total mixed-layer DIC transformation.

	KEO	**OSP**
	%	**%**
ΔDIC_{Gas}	5 ± 1	5 ± 4
ΔDIC_{EP}	8 ± 2	8 ± 2
ΔDIC_{Phys}	45 ± 7	47 ± 4
ΔDIC_{NCP}	39 ± 5	36 ± 8
ΔDIC_{CaCO3}	3 ± 0	4 ± 0
Total	**100 ± 15**	**100 ± 18**

Though both regions have strikingly similar percentage contributions from the process that influence the mixed-layer DIC concentration, they differ in terms of which processes exhibit the highest interannual variability (**Table 4**). There is no interannual variability in the $CaCO_3$ term, and EP variability has the same percentage contribution in both regions. At KEO, the process with the highest interannual variability is the physical budget term (7%) followed by the NCP term (5%), suggesting that these two processes largely compensate for each other. This leads to very small interannual variations on the gas exchange term (1%), which will be discussed further later

on. At OSP, the largest interannual variability is in the NCP term (8%) with half this amount of variability in the physical processes term (4%) and gas exchange (4%). Therefore, it appears that variability in the biological component of the budget at OSP is somewhat decoupled from the physical carbon input, and gas exchange makes up the difference. These dissimilarities between OSP and KEO may be due to the differing limitations on primary production. Near KEO, macronutrient limitation is relieved seasonally through entrainment and the ability of phytoplankton to utilize all available nutrients may be the result of ample iron supply from coastal water mass mixing and areal dust input from the Gobi Desert [*Harrison et al.*, 2004]. At OSP, iron limitation is relieved seasonally through entrainment, but iron can also be infused into the system through eddy transport, advection of iron rich shelf waters and areal deposition [*Boyd et al.*, 2004; *Whitney et al.*, 2005]. These alternative limiting nutrient supply mechanisms allow biological production at OSP to become decoupled from the physical component of the budget, which may be responsible for the larger interannual variability in gas exchange. This suggest that dynamic carbon cycle regions such as KEO, may, in some cases, be more stable in terms of annual air-sea CO_2 gas exchange than other regions that display more modest seasonality in DIC.

The influence of biological activity on carbon uptake in these two regions is clearly reflected in the seasonal CO_2 response to mixed-layer DIC and temperature changes (**Figure 12**). At KEO, deep convective mixing brings high carbon content waters to the surface in winter and NCP in spring reduces the mixed-layer DIC concentration significantly. Precipitation from late spring through summer is responsible for the further DIC dilution after the spring bloom (**Figure 5C**). Sea surface CO_2 concentrations show the exact opposite seasonal cycle, plummeting in winter and increasing rapidly after spring, allowing the region to become a weak source of CO_2 to the atmosphere in summer (**Figure 11B**). Using the relationship between CO_2 and temperature

described by Takahashi et al. (1993), sea surface CO_2 concentrations were normalized to the mean sea surface temperature. The results show that CO_2 concentrations at KEO would follow the DIC seasonal cycle in the absence of large seasonal temperature changes (**Figure 9A**). Thus, cooling in winter is responsible for reducing CO_2 concentrations by over 60 µatm and warming in summer has the reverse effect. In spring, biological activity increases the air-sea ΔCO_2 slightly; however, there is an offset in timing between peak biological activity (March-April) and maximum seawater CO_2 concentrations (August-September). The mixed-layer DIC reduction by spring NCP is not enough to counter the effect of summer warming on sea surface CO_2 concentrations; therefore, the seasonal cycle of seawater CO_2 at KEO is almost entirely driven by the temperature influence on seawater inorganic carbon chemistry. This thermodynamic control, rather than a physical mixing or biological control, explains the very small range of interannual variability in the DIC_{Gas} term (**Table 4**) and suggests that high aNCP in this region is not responsible for the strong anthropogenic CO_2 uptake.

At OSP, CO_2 concentrations are fairly constant year round; however, removing the influence of temperature on CO_2 gives rise to a large seasonal cycle (>100 µatm) that is aligned with mixed-layer DIC changes. The large amplitude of the temperature normalized CO_2 reflects the low buffer capacity of these waters [*Sabine et al.*, 2004], where the change in CO_2 for a given change in DIC is 50% larger at OSP than at KEO. Seasonal temperature changes at OSP (~9ºC) are smaller than those at KEO (~12ºC), and the observed sea surface CO_2 is often 180º out of phase with temperature. This is due to the larger influence of DIC on CO_2 than temperature at OSP, giving phytoplankton the upper hand since they can modify DIC, while temperature cannot. Mixed-layer DIC concentrations decrease at OSP during spring and summer due to NCP and precipitation, and

increase in winter due to entrainment of carbon rich waters. The overlap in timing between the productive season and warming as well as the entrainment period and cooling results in sea surface CO_2 levels that show little seasonality, as has been observed previously [*Takahashi et al.*, 1993, 2002]. The ability of biology to efficiently modify sea surface CO_2 by reducing the mixed-layer DIC concentration is an effect of the low buffer capacity of old, North Pacific waters. This, in combination with allochthonous iron supply may explain the larger interannual variability in gas exchange at OSP versus KEO.

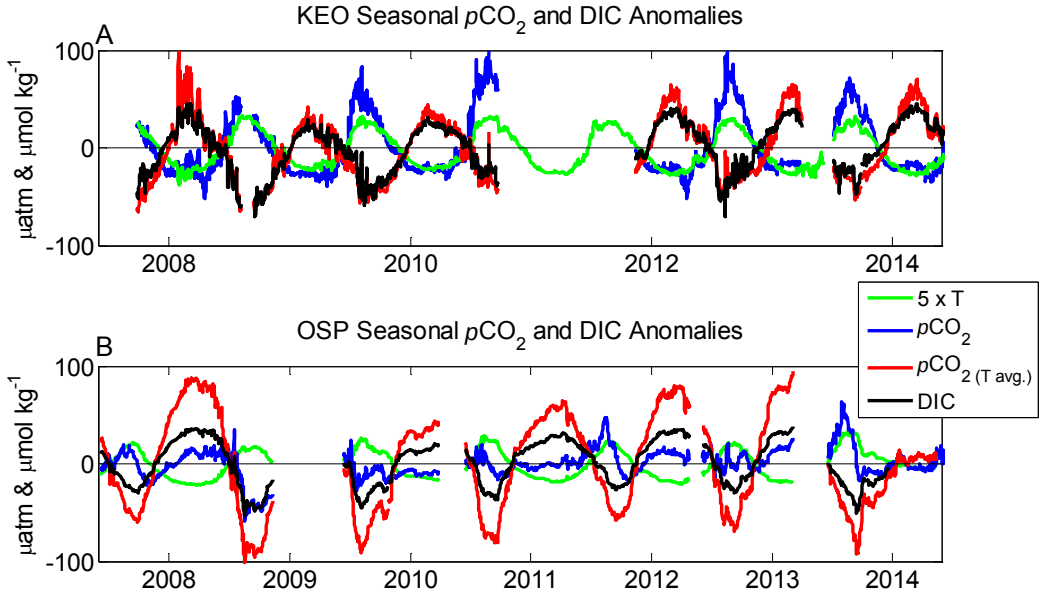

Figure 12. Seasonal anomalies calculated by subtracting the respective mean value from the time-series of temperature, pCO_2 and DIC. The temperature anomalies were multiplied by 5 for viewing. The anomalies for pCO_2 that has been normalized to the mean sea surface temperature are also shown (T avg.).

The interplay of physical, biological and chemical processes results in complex carbon cycling that gives rise to the observed net air-sea CO_2 exchange throughout the global ocean [*Takahashi et al.*, 2009]. At KEO, CO_2 gas exchange was primarily controlled by effect of seasonal temperature variability on CO_2 solubility. This means that alterations in the functionality of the biological pump may not have a large impact on anthropogenic CO_2 sink strength of the immediate

region, though downstream effects may be important. At OSP, biological activity does play an important role in air-sea CO_2 gas exchange. In particular, the decoupling of iron supply and vertical processes at OSP allows for larger interannual variability in seasonal biological carbon drawdown [*Hamme et al.*, 2010]. In addition, the low buffer capacity of the water makes it 50% easier for biology to reduce the sea surface CO_2 level than at KEO; therefore, variability in biological DIC consumption at OSP leads to notable variability in the seawater CO_2 content and thus in air-sea CO_2 gas exchange. Therefore, changes in the functionality or timing of biological processes in this region could have a significant influence on atmospheric CO_2 uptake. The seven years of *in situ* observations from both KEO and OSP suggest that stochastic events, such as the 2007-2008 cold event at KEO and the 2008-2009 anomalous iron enrichment at OSP [*Hamme et al.*, 2010], can rapidly change the balance of mixed-layer DIC controls and result in very different carbon cycling. Continued *in situ* observations from these time-series site will make it possible to learn more about the physical, chemical and biological drivers of regional carbon cycling and better assess how ocean warming and acidification may influence ocean carbon uptake.

6. Conclusions

Net community production (NCP) and calcium carbonate ($CaCO_3$) precipitation were estimated from seven years of high-frequency moored observations at the Kuroshio Extension Observatory using a mixed-layer, mass-balance approach. KEO exhibits a large seasonal cycle in mixed-layer NCP with no discernable production from July through February followed by a strong spring bloom. Extremely high levels of NCP were found during the 2007-2008 deployment year when a cyclonic eddy was centered near the mooring during the spring productive period, which enhanced nutrient supply as well as light availability by restricting the mixed layer depth.

Excluding the anomalous 2007-2008 deployment year, the mean annual NCP at KEO was found to be 4.5 ± 2.2 mol C m^{-2} yr^{-1} and interannual variability in the aNCP was slightly smaller than seasonal variations. NCP at OSP also showed significant seasonality with net heterotrophy occurring in fall and winter, and autotrophy in spring and summer. The mean aNCP at OSP was -1.9 ± 0.5 mol C m^{-2} yr^{-1} and seasonal variability was found to be substantially larger than interannual variability [*Fassbender et al.*, in prep]. These findings agree well with prior observations of NPC in the Alaska gyre and in the Western Subarctic gyre and Kuroshio-Oyashio transition region [*Wong et al.*, 2002b; *Harrison et al.*, 2004; *Sugiura and Tsunogai*, 2005; *Emerson and Stump*, 2010; *Yasunaka et al.*, 2013; *Lin et al.*, 2014]. Annual $CaCO_3$ production in both regions was -0.4 mol C m^{-2} yr^{-1}, though it was not statistically significant at KEO. The larger relative influence of $CaCO_3$ production at OSP was clearly reflected in the regional TA-salinity relationship, indicating that the TA-salinity relationship is a useful first order assessment of $CaCO_3$ importance in the open ocean.

The mixed-layer DIC budgets in both regions were primarily controlled by the competing effects of vertical diapycnal processes and NCP. Although NCP at KEO is twice that observed at OSP, it occurs during a few months in spring that do not overlap with peak seasonal warming and has little influence on air-sea CO_2 exchange. At OSP, productivity during spring and summer overlaps with seasonal warming and plays a significant role in maintaining seawater CO_2 below or near the atmospheric level during summer. In addition, the lower buffer capacity of waters near OSP relative to those is in the subtropical gyre near KEO allows biology to be 50% more effective at lowering seawater CO_2. Low buffer capacity water found throughout the subarctic region may

therefore help to explain why biological processes play a more dominant role than temperature in maintaining the North Pacific carbon sink region [*Ayers and Lozier*, 2012].

An important consideration in our methodology is the use of climatological gradients for estimation of horizontal and vertical processes, primarily during the dynamic spring detrainment period when storms are prevalent in both regions. Our uncertainty assessment is extremely conservative and in some cases our final aNCP estimates have errors larger than 100%. Even so, these uncertainties do not capture errors as associated with environmental conditions that deviate from the climatological mean state. Continuous *in situ* monitoring of vertical gradients through the use of profiling moorings or floats will significantly reduce the uncertainty in this component of the budget as well as in the mixed layer depth, which contributed largely to our uncertainties.

The NOAA Kuroshio Extension Observatory and Station Papa moorings are nearing a decade of continuous sea surface and atmospheric boundary layer CO_2 measurements. In these locations, the atmosphere and ocean interior are linked seasonally through isopycnal outcropping; therefore, carbon cycling in these regions sets the carbon characteristics of waters that will spend decades to centuries transiting the ocean interior. The rapid response of biology to stochastic environmental forcing at both KEO and OSP speaks to the importance of continuous in situ observations that can capture episodic ecosystem transitions and their influence on carbon export. Long-term, high-frequency (<daily) observations from these time-series sites, and others [*Sutton et al.*, 2014], will be vital to the study of carbon cycle responses to ocean change from both persistent forcing as well as oscillations in the climate system.

7. Acknowledgements

The authors thank Paul Quay and Steven Emerson for sharing unpublished datasets that contributed to this analysis. We thank the PMEL Ocean Climate Stations and Carbon Program groups that made this data set possible. This work was funded by the NOAA Climate Program Office, the NOAA Ocean Acidification Program and the NSF IGERT Program on Ocean Change.

8. Appendix A: Uncertainty Assessment

The uncertainty assessment for this analysis follows the approach of *Fassbender et al.*, (in prep) and details can be found therein. Here we include a table with the monthly mean uncertainties for each daily flux term in the KEO budget analysis (**Table A.1**). The gradient uncertainties are large due to the conservative nature of our computational error accounting and result in daily flux uncertainties larger than 100%, in some cases. Comparison of the estimated gradients used for this analysis and those observed during repeat hydrography cruises near KEO are shown in **Figure A.1**. In the process of integrating the daily fluxes over each annual deployment (**Section 5.1**) the errors are summed in quadrature. This reduces the uncertainty substantially, giving the 68% uncertainty bounds shown in **Figures 5-6** for the physical DIC and TA terms.

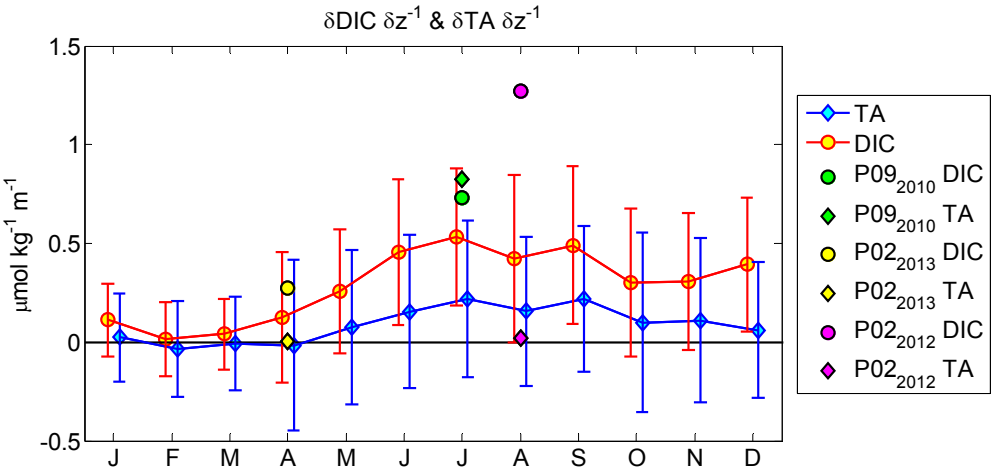

Figure A.1. Monthly climatology of vertical DIC and TA gradients at the base of the mixed layer with 68% uncertainty bounds. Climatology values are slightly offset in each month for easier viewing. Vertical DIC and TA gradients observed during three CLIVAR cruises near KEO mooring are shown for comparison. Uncertainties in these gradients are primarily from computational errors that accumulate through the prediction of monthly DIC and TA fields (**Section 3.4**).

Table A.1. The monthly climatology of turbulent diffusion as well as 1σ % errors for the turbulent diffusion term, mixed layer depth, daily salinity fluxes due to EP and physical processes, and the vertical salinity gradients.

	κ	κ	MLD	Sal_{EP}	Sal_{Phys}	$\partial Sal\ \partial z^{-1}$	$(Sal_a-Sal_b)/h$
	$m^2\ d^{-1}$	$m^2\ d^{-1}$	MLD	d^{-1}	d^{-1}	m^{-1}	m^{-1}
Month	**values**	**% Error**	**% Error**	**% Error**	**% Error**	**% Error**	**% Error**
1	5.2E-03	67	6	>100	92	>100	>100
2	8.8E-03	79	7	>100	36	>100	>100
3	1.6E-02	68	7	>100	36	>100	73
4	6.2E-03	67	9	>100	18	>100	>100
5	1.1E-03	46	10	11	36	74	46
6	4.0E-04	56	12	>100	60	57	38
7	3.0E-04	20	14	62	>100	12	20
8	2.0E-04	24	12	61	99	8	23
9	2.0E-04	36	13	5	>100	67	86
10	5.0E-04	29	16	>100	>100	>100	64
11	9.0E-04	72	13	91	>100	>100	>100
12	2.5E-03	92	6	>100	>100	>100	>100

Table A.2. 1σ errors for the calculated DIC and TA time series values and 1σ % errors for each daily flux term in the DIC and TA budgets. 1σ % errors on the vertical gradients are also given. For this table, µM is used as shorthand for µmol kg^{-1}.

	DIC	DIC_{Gas}	DIC_{EP}	DIC_{Phys}	$\partial DIC\ \partial z^{-1}$	$(DIC_a\text{-}DIC_h)/h$	DIC_{Bio}	TA	TA_{EP}	TA_{Phys}	$\partial TA\ \partial z^{-1}$	$(TA_a\text{-}TA_h)/h$	TA_{Bio}
	µM	µM d^{-1}	µM d^{-1}	µM d^{-1}	µM m^{-1}	µM m^{-1}	µM	µM	µM d^{-1}	µM d^{-1}	µM m^{-1}	µM m^{-1}	µM
Month	**1σ**	**1σ %**	**1σ %**	**1σ %**	**1σ %**	**1σ %**	**1σ %**	**1σ**	**1σ %**	**1σ %**	**1σ %**	**1σ %**	**1σ %**
1	5.8	28	>100	80	>100	67	>100	7.3	>100	>100	>100	>100	36
2	5.8	28	>100	83	>100	76	>100	7.3	>100	>100	>100	>100	57
3	5.8	28	>100	58	>100	69	>100	7.3	>100	99	>100	>100	>100
4	5.8	29	>100	31	>100	>100	35	7.3	>100	>100	>100	>100	>100
5	5.7	28	11	>100	>100	69	26	7.3	11	>100	>100	>100	>100
6	5.7	26	>100	79	79	71	22	7.3	>100	84	>100	>100	>100
7	5.6	13	63	56	66	84	18	7.3	62	>100	>100	>100	>100
8	5.6	29	61	96	>100	>100	16	7.3	61	>100	>100	>100	>100
9	5.6	21	5	73	81	>100	16	7.3	4	>100	>100	>100	>100
10	5.6	23	>100	>100	>100	71	>100	7.3	>100	>100	>100	>100	>100
11	5.7	29	93	96	>100	49	>100	7.3	90	>100	>100	>100	75
12	5.7	28	>100	80	88	>100	>100	7.3	>100	>100	>100	>100	51

*µM is shorthand for µmol kg^{-1} in this table.

Table A.3. Mean monthly values for the annual composites of integrated NCP and $CaCO_3$ production based on all deployment years as well as the 68% calculation uncertainties (not standard deviations).

	NCP	NCP	$CaCO_3$	$CaCO_3$
	mol C m^2	mol C m^2	mol C m^2	mol C m^2
Month	**value**	**1σ %**	**value**	**1σ %**
10	-0.1	>100	-0.02	>100
11	-0.3	>100	-0.05	>100
12	-0.4	>100	-0.08	>100
1	-0.4	>100	-0.17	>100
2	0.4	>100	-0.13	>100
3	-0.2	>100	-0.08	>100
4	-2.1	98	-0.24	>100
5	-3.2	63	-0.34	>100
6	-3.8	53	-0.39	>100
7	-4.4	50	-0.44	>100
8	-4.5	49	-0.45	>100
9	-4.5	48	-0.44	>100

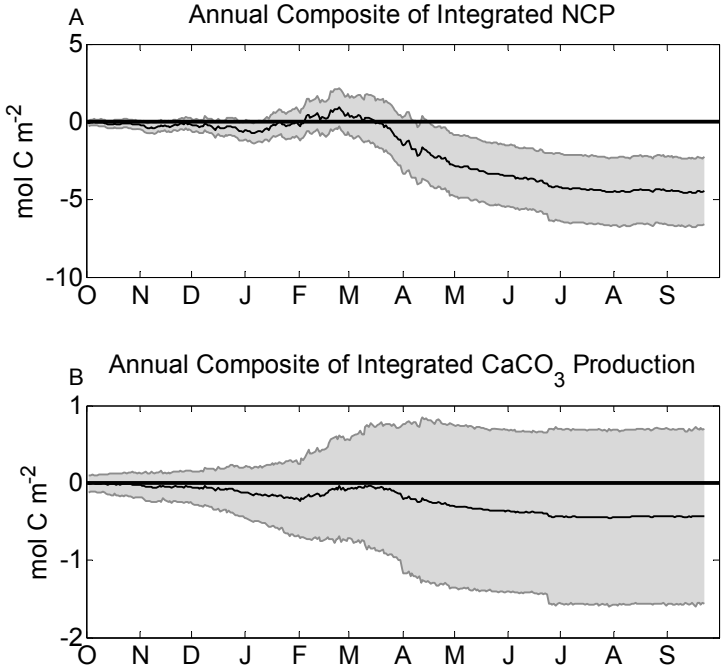

Figure A.2. Annual composites of integrated (**A**) NCP and (**B**) $CaCO_3$ production with 68% calculation uncertainties shown (not standard deviations).

9. References

Anderson, L. A., and J. L. Sarmiento (1994), Redfield ratios of remineralization determined by nutrient data analysis, *Global Biogeochem. Cycles*, *8*(1), 65–80.

Atlas, R., R. N. Hoffman, J. Ardizzone, S. M. Leidner, J. C. Jusem, D. K. Smith, and D. Gombos (2011), A Cross-calibrated, Multiplatform Ocean Surface Wind Velocity Product for Meteorological and Oceanographic Applications, *Bull. Am. Meteorol. Soc.*, *92*(2), 157–174, doi:10.1175/2010BAMS2946.1.

Ayers, J. M., and M. S. Lozier (2010), Physical controls on the seasonal migration of the North Pacific transition zone chlorophyll front, *J. Geophys. Res.*, *115*(C5), 1–11, doi:10.1029/2009JC005596.

Ayers, J. M., and M. S. Lozier (2012), Unraveling dynamical controls on the North Pacific carbon sink, *J. Geophys. Res.*, *117*(C1), C01017, doi:10.1029/2011JC007368.

Bates, N. R., Y. M. Astor, M. J. Church, K. I. Currie, J. Dore, M. Gonaález-Dávila, L. Lorenzoni, F. Muller-Karger, J. Olafsson, and M. Santa-Casiano (2014), A Time-Series View of Changing Ocean Chemistry Due to Ocean Uptake of Anthropogenic CO_2 and Ocean Acidification, *Oceanography*, *27*(1), 126–141, doi:10.5670/oceanog.2014.16.

Bentamy, A., and D. C. Fillon (2012), Gridded surface wind fields from Metop/ASCAT measurements, *Int. J. Remote Sens.*, *33*(6), 1729–1754, doi:10.1080/01431161.2011.600348.

Bishop, J. K., S. Calvert, and M. Soon (1999), Spatial and temporal variability of POC in the northeast Subarctic Pacific, *Deep Sea Res. Part II Top. …*, *46*, 2699–2733.

Bonjean, F., and G. S. E. Lagerloef (2002), Diagnostic model and analysis of the surface currents in the tropical Pacific Ocean, *J. Phys. Ocean.*, *32*, 2938–2954.

Boyd, P. W. et al. (2004), The decline and fate of an iron-induced subarctic phytoplankton bloom., *Nature*, *428*(6982), 549–53, doi:10.1038/nature02437.

De Boyer Montégut, C. (2004), Mixed layer depth over the global ocean: An examination of profile data and a profile-based climatology, *J. Geophys. Res.*, *109*(C12), C12003, doi:10.1029/2004JC002378.

Chen, C. A. (2002), Shelf- vs . dissolution-generated alkalinity above the chemical lysocline, , *49*, 5365–5375.

Chierici, M., A. Fransson, and Y. Nojiri (2006), Biogeochemical processes as drivers of surface fCO_2 in contrasting provinces in the subarctic North Pacific Ocean, *Global Biogeochem. Cycles*, *20*(1), doi:10.1029/2004GB002356.

Cronin, M. F., N. a. Bond, J. Thomas Farrar, H. Ichikawa, S. R. Jayne, Y. Kawai, M. Konda, B. Qiu, L. Rainville, and H. Tomita (2013), Formation and erosion of the seasonal thermocline in the Kuroshio Extension Recirculation Gyre, *Deep Sea Res. Part II Top. Stud. Oceanogr.*, *85*, 62–74, doi:10.1016/j.dsr2.2012.07.018.

Dickson, A. G. (1990), Standard potential of the reaction : $AgCl_{(s)} + 1/2H_{2(g)} = Ag_{(s)} + HCl_{(aq)}$, and the standard acidity constant of the ion HSO_4^- in synthetic sea water from 273.15 to 318.15 K, *J. Chem. Thermodyn.*, (22), 113–127.

Dickson, A. G., and J. Riley (1978), The effect of analytical error on the evaluation of the components of the aquatic carbon-dioxide system, *Mar. Chem.*, *6*, 77–85, doi:10.1016/0304-4203(78)90008-7.

Doney, S. C. (2006), Plankton in a warmer world, *Nature*, *444*, doi:10.1029/2003GB002134.

Doney, S. C., V. J. Fabry, R. A. Feely, and J. a. Kleypas (2009), Ocean acidification: the other CO_2 problem., *Ann. Rev. Mar. Sci.*, *1*(1), 169–92, doi:10.1146/annurev.marine.010908.163834.

Emerson, S. R., and C. Stump (2010), Net biological oxygen production in the ocean—II: Remote in situ measurements of O_2 and N_2 in subarctic pacific surface waters, *Deep Sea Res. Part I Oceanogr. Res. Pap.*, *57*(10), 1255–1265, doi:10.1016/j.dsr.2010.06.001.

Emerson, S. R., C. L. Sabine, M. F. Cronin, R. A. Feely, S. E. Cullison Gray, and M. D. DeGrandpre (2011), Quantifying the flux of $CaCO_3$ and organic carbon from the surface ocean using in situ measurements of O_2, N_2, pCO_2, and pH, *Global Biogeochem. Cycles*, *25*(3), 1–12, doi:10.1029/2010GB003924.

Falkowski, P. G. (1998), Biogeochemical Controls and Feedbacks on Ocean Primary Production, *Science (80-.).*, *281*(5374), 200–206, doi:10.1126/science.281.5374.200.

Fassbender, A. J., C. L. Sabine, and M. F. Cronin (n.d.), Net community production and calcification from seven years of NOAA Station Papa Mooring measurements., *In prep.*

Favorite, F. (1976), Oceanography of the subarctic Pacific region, 1960-71, *Bull Int North Pac Fish Comm*, *33*, 1–187.

Feely, R. A. (2002), In situ calcium carbonate dissolution in the Pacific Ocean, *Global Biogeochem. Cycles*, *16*(4), 1–12, doi:10.1029/2002GB001866.

Feely, R. A., A. G. Dickson, D. A. Hansell, and C. A. Carlson (2004), *Carbon Dioxide, Hydrographic, and Chemical Data Obtained During the R/V Melville Cruise in the Pacific Ocean on CLIVAR Repeat Hydrography Sections P02_2004 (15 June - 27 August, 2004).*

Freeland, H. J. (2007), A short history of Ocean Station Papa and Line P, *Prog. Oceanogr.*, *75*(2), 120–125, doi:10.1016/j.pocean.2007.08.005.

Fukasawa, M., T. Kawano, A. Murata, F. Shibata, M. Kitada, T. Ohama, and Y. Ishikawa (2005), *Carbon Dioxide, Hydrographic, and Chemical Data Obtained During the R/V Mirai Repeat Hydrography Cruise in the Pacific Ocean: CLIVAR CO_2 Section P10_2005 (25 May - 2 July, 2005)*.

Garcia, H. E., R. A. Locarnini, T. P. Boyer, J. I. Antonov, A. V. Mishonov, O. K. Baranova, M. M. Zweng, J. R. Reagan, and D. R. Johnson (2013a), World Ocean Atlas 2013. Vol. 3: Dissolved Oxygen, Apparent Oxygen Utilization, and Oxygen Saturation, in *NOAA Atlas NESDIS 75*, edited by S. Levitus and A. Mishonov, p. 27.

Garcia, H. E., R. A. Locarnini, T. P. Boyer, J. I. Antonov, O. K. Baranova, M. M. Zweng, J. R. Reagan, and D. R. Johnson (2013b), World Ocean Atlas 2013. Vol. 4: Dissolved Inorganic Nutrients (phosphate, nitrate, silicate), in *NOAA Atlas NESDIS 76*, vol. 4, edited by S. Levitus and A. Mishonov, p. 25.

Giesbrecht, K. E., R. C. Hamme, and S. R. Emerson (2012), Biological productivity along Line P in the subarctic northeast Pacific: In situ versus incubation-based methods, *Global Biogeochem. Cycles*, *26*(3), n/a–n/a, doi:10.1029/2012GB004349.

Hamme, R. et al. (2010), Volcanic ash fuels anomalous plankton bloom in subarctic northeast Pacific, *Geophys. Res. Lett.*, *37*, doi:10.1029/2010GL044629.

Harrison, P. J., F. A. Whitney, and A. Tsuda (2004), Nutrient and plankton dynamics in the NE and NW gyres of the subarctic Pacific Ocean, *J. Oceanogr.*, *60*, 93–117.

Van Heuven, S. M. A. C., D. Pierrot, J. W. B. Rae, E. Lewis, and D. W. R. Wallace (2011), MATLAB Program Developed for CO_2 System Calculations, *ORNL/CDIAC-105b. Carbon Dioxide Inf. Anal. Center, Oak Ridge Natl. Lab. U.S. Dep. Energy, Oak Ridge, Tennessee*. Available from: http://cdiac.ornl.gov/ftp/co2sys/CO2SYS_calc_MATLAB_v1.1/ (Accessed 2 July 2014)

Jin, X., N. Gruber, J. P. Dunne, J. L. Sarmiento, and R. a. Armstrong (2006), Diagnosing the contribution of phytoplankton functional groups to the production and export of particulate organic carbon, CaCO 3 , and opal from global nutrient and alkalinity distributions, *Global Biogeochem. Cycles*, *20*(2), n/a–n/a, doi:10.1029/2005GB002532.

Juranek, L. W., P. D. Quay, R. A. Feely, D. Lockwood, D. M. Karl, and M. J. Church (2012), Biological production in the NE Pacific and its influence on air-sea CO_2 flux: Evidence from dissolved oxygen isotopes and O_2/Ar, *J. Geophys. Res.*, *117*(C5), C05022, doi:10.1029/2011JC007450.

Kamiya, H., M. Ishii, and T. Nakano (2012), *Carbon Dioxide, Hydrographic, and Chemical Data Obtained During the R/V Ryofu Maru Repeat Hydrography Cruise in the Pacific Ocean: CLIVAR CO_2 Section P09_2010 (6 July - 22 August, 2010).*

Kelly, K. a., R. J. Small, R. M. Samelson, B. Qiu, T. M. Joyce, Y.-O. Kwon, and M. F. Cronin (2010), Western Boundary Currents and Frontal Air–Sea Interaction: Gulf Stream and Kuroshio Extension, *J. Clim.*, *23*(21), 5644–5667, doi:10.1175/2010JCLI3346.1.

Lauvset, S. K., N. Gruber, P. Landschützer, a. Olsen, and J. Tjiputra (2014), Trends and drivers in global surface ocean pH over the past three decades, *Biogeosciences Discuss.*, *11*(11), 15549–15584, doi:10.5194/bgd-11-15549-2014.

Lin, P., F. Chai, H. Xue, and P. Xiu (2014), Modulation of decadal oscillation on surface chlorophyll in the Kuroshio Extension, *J. Geophys. Res. Ocean.*, *119*(1), 187–199, doi:10.1002/2013JC009359.

Lipsen, M. S., D. W. Crawford, J. Gower, and P. J. Harrison (2007), Spatial and temporal variability in coccolithophore abundance and production of PIC and POC in the NE subarctic Pacific during El Niño (1998), La Niña (1999) and 2000, *Prog. Oceanogr.*, *75*(2), 304–325, doi:10.1016/j.pocean.2007.08.004.

Liu, W. T., K. B. Katsaros, and J. A. Businger (1979), Bulk parameterization of air-sea exchanges of heat and water vapor including the molecular constraints at the interface, *J. Atmos. Sci.*, *36*.

Locarnini, R. A., A. V. Mishonov, J. I. Antonov, T. P. Boyer, H. E. Garcia, O. K. Baranova, and D. S. M. M. Zweng, C. R. Paver, J. R. Reagan, D. R. Johnson, M. Hamilton (2013), World Ocean Atlas 2013, Volume 1: Temperature, in *NOAA Atlas NESDIS 73*, edited by S. Levitus and A. Mishonov, p. 40 pp.

Lockwood, D. (2013), Impact of the marine biological pump on atmospheric CO_2 uptake in the North Pacific: a study based on basin-wide underway measurements of oxygen/argon gas ratios and pO_2, University of Washington.

Lueker, T. J., A. G. Dickson, and C. D. Keeling (2000), Ocean pCO_2 calculated from dissolved inorganic carbon, alkalinity, and equations for K_1 and K_2: validation based on laboratory measurements of CO_2 in gas and seawater at equilibrium, *Mar. Chem.*, *70*, 105–119, doi:10.1016/S0304-4203(00)00022-0.

Lyman, J. M., S. A. Good, V. V Gouretski, M. Ishii, G. C. Johnson, M. D. Palmer, D. M. Smith, and J. K. Willis (2010), Robust warming of the global upper ocean., *Nature*, *465*(7296), 334–7, doi:10.1038/nature09043.

Martin, J., and S. Fitzwater (1988), Iron deficiency limits phytoplankton growth in the north-east Pacific subarctic, *Nature*.

Millero, F. J. (2007), The marine inorganic carbon cycle., *Chem. Rev.*, *107*, 308–341, doi:10.1021/cr0503557.

Milliman, J. D., P. J. Troy, W. M. Balch, A. K. Adams, Y.-H. Li, and F. T. Mackenzie (1999), Biologically mediated dissolution of calcium carbonate above the chemical lysocline?, *Deep Sea Res. Part I Oceanogr. Res. Pap.*, *46*(10), 1653–1669, doi:10.1016/S0967-0637(99)00034-5.

Murata, A., Y. Kumamoto, H. Uchida, M. Aoyama, K.Sasaki, and T. Aono (2014), *Carbon Dioxide, Hydrographic, and Chemical Data Obtained During the R/V Mirai Repeat Hydrography Cruise in the Pacific Ocean: CLIVAR CO_2 Section P10_2011 (20 December - 9 February, 2011)*.

Nightingale, P. D., G. Malin, C. S. Law, A. J. Watson, S. Liss, I. Liddicoat, P. S. Liss, M. I. Liddicoat, J. Boutin, and R. C. Upstill-Goddard (2000), In situ evaluation of air-sea gas exchange parameterizations using novel conservative and volatile tracers, *Glob. Biogeochem. Cycles*, *14*(1), 373–387.

Ono, T., H. Kasai, T. Midorikawa, Y. Takatani, K. Saito, M. Ishii, Y. W. Watanabe, and K. Sasaki (2005), Seasonal and Interannual Variation of DIC in Surface Mixed Layer in the Oyashio Region: A Climatological View, *J. Oceanogr.*, *61*(6), 1075–1087, doi:10.1007/s10872-006-0023-0.

Qiu, B. (2003), Kuroshio Extension variability and forcing of the Pacific decadal oscillations: Responses and potential feedback, *J. Phys. Oceanogr.*, (2002), 2465–2482.

Rainville, L., S. R. Jayne, and M. F. Cronin (2014), Variations of the North Pacific Subtropical Mode Water from Direct Observations, *J. Clim.*, *27*(8), 2842–2860, doi:10.1175/JCLI-D-13-00227.1.

Sabine, C. L., R. M. Key, M. Hall, and A. Kozyr (1999), *Carbon Dioxide, Hydrographic, and Chemical Data Obtained During the R/V Thomas G. Thompson Cruise in the Pacific Ocean (WOCE Section P10, October 5 - November 10, 1993)*.

Sabine, C. L. et al. (2004), The oceanic sink for anthropogenic CO_2, *Science*, *305*(5682), 367–71, doi:10.1126/science.1097403.

Sarmiento, J. L., J. P. Dunne, A. Gnanadesikan, R. M. Key, K. Matsumoto, and R. Slater (2002), A new estimate of the $CaCO_3$ to organic carbon export ratio, *Global Biogeochem. Cycles*, *16*(4), 54–1–54–12, doi:10.1029/2002GB001919.

Send, U. (2010), A Global Boundary Current Circulation Observing Network, in *Proceedings of OceanObs'09: Sustained Ocean Observations and Information for Society*, pp. 841–853, European Space Agency.

Sigman, D. M., and E. A. Boyle (2000), Glacial/interglacial variations in atmospheric carbon dioxide, *Nature*, *407*(6806), 859–869.

Sugiura, K., and S. Tsunogai (2005), Spatial and temporal variation of surface xCO_2 providing net biological productivities in the western North Pacific in June, *J. Oceanogr.*, *61*.

Sukigara, C., T. Suga, T. Saino, K. Toyama, D. Yanagimoto, K. Hanawa, and N. Shikama (2011), Biogeochemical evidence of large diapycnal diffusivity associated with the subtropical mode water of the North Pacific, *J. Oceanogr.*, *67*(1), 77–85, doi:10.1007/s10872-011-0008-5.

Sutton, A. J. et al. (2014), A high-frequency atmospheric and seawater pCO_2 data set from 14 open ocean sites using a moored autonomous system, *Earth Syst. Sci. Data Discuss.*, *7*, 385–418, doi:10.5194/essdd-7-385-2014.

Swift, J. et al. (2014), *Carbon Dioxide, Hydrographic, and Chemical Data Obtained During the R/V Melville Cruise in the Pacific Ocean on GO-SHIP Repeat Hydrography Sections P02_2013 (21 March - 1 June, 2013)*.

Takahashi, T., J. G. Goddard, and D. W. Chipman (1993), Seasonal Variation of CO_2 and Nutrients in the High-Latitude surface oceans: acomparative study, *Global Biogeochem. Cycles*, *7*(4), 843–878.

Takahashi, T., S. C. Sutherland, C. Sweeney, A. Poisson, N. Metzl, B. Tilbrook, N. R. Bates, R. Wanninkhof, R. A. Feely, and C. L. Sabine (2002), Global sea–air CO_2 flux based on climatological surface ocean pCO_2, and seasonal biological and temperature effects, *Deep Sea Res. Part II Top. Stud. Oceanogr.*, *49*(9-10), 1601–1622, doi:10.1016/S0967-0645(02)00003-6.

Takahashi, T., S. C. Sutherland, R. A. Feely, and R. Wanninkhof (2006), Decadal change of the surface water pCO_2 in the North Pacific: A synthesis of 35 years of observations, *J. Geophys. Res.*, *111*(C7), 1–20, doi:10.1029/2005JC003074.

Takahashi, T. et al. (2009), Climatological mean and decadal change in surface ocean pCO_2, and net sea–air CO_2 flux over the global oceans, *Deep Sea Res. Part II Top. Stud. Oceanogr.*, *56*(8-10), 554–577, doi:10.1016/j.dsr2.2008.12.009.

Teague, W. J., M. J. Carron, and P. J. Hogan (1990), A Comparison Between the Generalized Digital Environmental Model and Levitus climatologies, *J. Geophys. Res.*, *95*(C5), 7167, doi:10.1029/JC095iC05p07167.

Timothy, D., C. Wong, J. E. Barwell-Clarke, J. S. Page, L. A. White, and R. W. Macdonald (2013), Climatology of sediment flux and composition in the subarctic Northeast Pacific Ocean with biogeochemical implications, *Prog. Oceanogr.*, *116*, 95–129, doi:10.1016/j.pocean.2013.06.017.

Wanninkhof, R. (1992), Relationship Between Wind Speed and Gas Exchange Over the Ocean, *J. Geophys. Res.*, *97*(C5), 7373–7382, doi:10.1029/92JC00188.

Weiss, R. (1974), Carbon dioxide in water and seawater: the solubility of a non-ideal gas, *Mar. Chem.*, *2*(3), 203–215, doi:10.1016/0304-4203(74)90015-2.

Whitney, F. A., W. R. Crawford, and P. J. Harrison (2005), Physical processes that enhance nutrient transport and primary productivity in the coastal and open ocean of the subarctic NE Pacific, *Deep Sea Res. Part II Top. Stud. Oceanogr.*, *52*(5-6), 681–706, doi:10.1016/j.dsr2.2004.12.023.

Wolfgladrow, D., R. E. Zeebe, C. Klaas, a Kortzinger, and A. G. Dickson (2007), Total alkalinity: The explicit conservative expression and its application to biogeochemical processes, *Mar. Chem.*, *106*(1-2), 287–300, doi:10.1016/j.marchem.2007.01.006.

Wong, C., F. A. Whitney, K. Iseki, J. S. C. Page, and J. Zeng (1995), Analysis of trends in primary productivity and chlorophyll-a over two decades at Ocean Station P (50 N, 145 W) in the subarctic Northeast Pacific Ocean, *Can. Spec. Publ. Fish. Aquat. Sci.*, *121*, 107–117.

Wong, C., F. A. Whitney, D. W. Crawford, K. Iseki, R. J. Matear, W. Johnson, J. S. C. Page, and D. Timothy (1999), Seasonal and interannual variability in particle fluxes of carbon, nitrogen and silicon from time series of sediment traps at Ocean Station P, 1982–1993: relationship to changes in subarctic primary productivity, *Deep Sea Res. Part II Top. Stud. Oceanogr.*, *46*(11-12), 2735–2760, doi:10.1016/S0967-0645(99)00082-X.

Wong, C., N. A. D. Waser, Y. Nojiri, W. K. Johnson, F. A. Whitney, J. S. C. Page, and J. Zeng (2002a), Seasonal and interannual variability in the distribution of surface nutrients and dissolved inorganic carbon in the Northern North Pacific: influence of El Niño, *J. Oceanogr.*, *58*(2), 227–243.

Wong, C., N. A. D. Waser, Y. Nojiri, F. A. Whitney, J. S. C. Page, and J. Zeng (2002b), Seasonal cycles of nutrients and dissolved inorganic carbon at high and mid latitudes in the North Pacific Ocean during the Skaugran cruises: determination of new production and nutrient uptake ratios, *Deep Sea Res. Part II Top. Stud. Oceanogr.*, *49*(24-25), 5317–5338, doi:10.1016/S0967-0645(02)00193-5.

Wong, C., N. A. D. Waser, F. A. Whitney, W. Johnson, and J. S. C. Page (2002c), Time-series study of the biogeochemistry of the North East subarctic Pacific: reconciliation of the Corg/N remineralization and uptake ratios with the Redfield ratios, *Deep Sea Res. Part II Top. Stud. Oceanogr.*, *49*(24-25), 5717–5738, doi:10.1016/S0967-0645(02)00211-4.

Yasuda, I. (2003), Hydrographic Structure and Variability in the Kuroshio-Oyashio Transition Area, *J. Oceanogr.*, *59*, 389–402.

Yasunaka, S., Y. Nojiri, S. Nakaoka, T. Ono, H. Mukai, and N. Usui (2013), Monthly maps of sea surface dissolved inorganic carbon in the North Pacific: Basin-wide distribution and seasonal variation, *J. Geophys. Res. Ocean.*, *118*(8), 3843–3850, doi:10.1002/jgrc.20279.

Yasunaka, S., Y. Nojiri, S. Nakaoka, T. Ono, F. A. Whitney, and M. Telszewski (2014), Mapping of sea surface nutrients in the North Pacific: Basin-wide distribution and seasonal to interannual variability, *J. Geophys. Res. Ocean.*, n/a–n/a, doi:10.1002/2014JC010318.

Zweng, M. M. et al. (2013), World Ocean Atlas 2013, Volume 2: Salinity, in *NOAA Atlas NESDIS 74*, vol. 2, edited by S. Levitus and A. Mishonov, p. 39.

Chapter 4

A robust sensor for extended autonomous measurements of surface ocean dissolved inorganic carbon

Andrea J. Fassbender[a,*], Christopher L. Sabine[b], Noah Lawrence-Slavas[b], Eric H. De Carlo[c], Christian Meinig[b], Stacy Maenner Jones[b]

[a]School of Oceanography, University of Washington, Seattle, Washington, USA; [b]Pacific Marine Environmental Laboratory, National Oceanic and Atmospheric Administration, Seattle, Washington, USA; [c]School of Ocean and earth Science and Technology, University of Hawai'i at Mānoa, Honolulu, HI, USA.

1. Abstract

Ocean carbon monitoring efforts have increased dramatically in the past few decades in response to the need of better marine carbon cycle characterization. Autonomous pH and carbon dioxide (CO_2) sensors capable of yearlong deployments are now commercially available; however, due to their strong covariance, this is the least desirable pair of the four measurable carbonate system parameters to measure for high-quality, *in situ*, carbon cycle studies. An alternative parameter must be measured with either pH or CO_2 in order to achieve the accuracy necessary to resolve changes in the anthropogenic carbon inventory of the surface ocean. In response to this need, we have developed a robust surface ocean dissolved inorganic carbon (DIC) sensor capable of extended (>year) field deployments with a measurement accuracy of ±5 μmol kg^{-1}. Results from the first two field tests indicate that DIC sensor measurements are ~90% more accurate than estimates of DIC calculated from contemporaneous and collocated measurements of pH and CO_2. The improved accuracy provided by this robust new sensor now makes it possible to conduct the

high-quality, extended duration, *in situ* observations needed to quantitatively evaluate marine carbon cycling.

2. Introduction

The marine biogeochemical cycles are among the more difficult components of the climate system to characterize and thus project the impacts on, and feedbacks from, climate change. This difficulty largely derives from the challenges in developing robust autonomous marine sensors with the endurance and accuracy needed for long-term observational efforts that can resolve environmental variability at the scale needed for synthesis and modeling work [*Schuster et al.*, 2009]. In the past few decades, increased emphasis on understanding the marine carbon cycle and its feedback mechanisms has led to greater demand for autonomous marine carbon sensors. While advancements have been made in the development of some sensors, there remains a need for the development of additional sensors that provide greater insight into the carbon system than those currently in existence.

To accurately describe the inorganic carbon chemistry of seawater, two of the four measurable carbonate system parameters must be measured simultaneously. The four carbonate system parameters that have been routinely measured from ships are: dissolved inorganic carbon (DIC), total alkalinity (TA), partial pressure of carbon dioxide (pCO_2) and pH. Measurement of any two of these parameters in seawater makes it possible to calculate all other carbonate system parameters using equilibrium constants, temperature, pressure, and salinity [*Dickson et al.*, 2007; *van Heuven et al.*, 2011].

Technological advances over the past decade have led to the development of commercially available autonomous carbon dioxide (CO_2) and pH sensors that are capable of extended deployments on moored platforms. The new sensors have been particularly helpful in further elucidating short-term linkages between CO_2 and primary production and the importance of episodic events in biological carbon uptake and export [*McGillicuddy et al.*, 1998, 2007; *Karl et al.*, 2003; *Hales et al.*, 2006; *Hamme et al.*, 2010; *Evans et al.*, 2011]. Long-term, dual parameter carbon cycle observations from autonomous platforms will be essential in the development and ground truthing of satellite products that may ultimately resolve the current spatiotemporal gaps in ocean carbon monitoring capabilities [*Friedrich and Oschlies*, 2009; *Gledhill et al.*, 2009; *Hales et al.*, 2012]. Unfortunately, because of the strong covariance between pH and CO_2, this pair is the least desirable for constraining seawater carbonate chemistry [*Dickson and Riley*, 1978; *Millero*, 2007; *Cullison Gray et al.*, 2011]. To achieve the accuracy necessary for climate-quality carbon cycle studies at time series locations, an alternative carbonate system parameter must be measured in addition to either pH or CO_2.

We have developed an accurate autonomous DIC sensor that has the endurance required for extended deployments on moorings. DIC is a particularly desirable parameter to characterize because it integrates all of the processes that influence the marine carbonate system and has a larger magnitude response to photosynthesis and respiration than TA and reflects gas exchange, which TA does not. A number of analytical methods have been utilized for the direct determination of DIC in natural and marine waters [*Schuster et al.*, 2009; *Wang et al.*, 2013]. Our method includes nearly complete conversion of DIC to CO_2 by acidification, followed by equilibration of the CO_2 in the acidified liquid sample with a closed loop of air, which is quantified using non-dispersive

infrared (NDIR) spectrophotometry. NDIR spectrophotometry has been utilized by numerous investigators in similar laboratory and ship based techniques [*Broecker and Takahashi*, 1966; *Wong*, 1970; *Goulden*, 1976; *Salonen*, 1981; *Goyet and Snover*, 1993; *Goyet*, 1994; *O'Sullivan and Millero*, 1998; *Hales et al.*, 2004; *Kaltin et al.*, 2005; *Bandstra et al.*, 2006] but has not previously been adapted for an autonomous mooring based DIC sensor. In addition, the NDIR approach is suitable for autonomous operation on a mooring [*Schuster et al.*, 2009] and has the added benefit of being the core technology used in the Moored Autonomous pCO_2 ($MAPCO_2$) system that was originally developed at the Monterey Bay Aquarium Research Institute, improved upon at the Pacific Marine Environmental Laboratory (PMEL) and is now commercially manufactured by Battelle Memorial Institute [*Sutton et al.*, 2014].

To the best of our knowledge, there have been three published field tests of other autonomous DIC sensors [*Sayles and Eck*, 2009; *Liu et al.*, 2013; *Wang et al.*, 2013]. These sensors represent substantial progress towards *in situ* DIC monitoring; however, excluding the 56 day field test described by Sayles and Eck (2009), deployments have thus far been limited to eight days or less. The sensor we have developed is capable of 2,920 *in situ* analyses, which is equivalent to a three-hourly sampling frequency over the course of 365 days. Two-way Iridium satellite communication is used to telemeter data back to the laboratory after every two DIC sample measurements allowing for near real-time data delivery and in-situ modifications to instrument parameters, such as sampling frequency, in response to changing environmental conditions. Here we describe this novel Moored Autonomous DIC (MADIC) system and present results from a one month test deployment in Seattle, Washington and a seven month field test near Honolulu, Hawaii.

3. Methods

3.1. Principle

Dissolved inorganic carbon (DIC) refers to the sum of the concentrations of carbonic acid (H_2CO_3), bicarbonate ion (HCO_3^-), carbonate ion (CO_3^{2-}), and carbon dioxide (CO_2) in aqueous solution. Because it is impossible to measure the concentration of each of these molecular species individually, our sensor converts DIC into the CO_2 molecular form by acidifying ~1mL of seawater to a pH of ~3.5. CO_2 in the acidified liquid sample escapes to the gas phase as air, previously stripped of CO_2, is bubbled through the liquid in a recirculating loop. Once equilibrium is reached, CO_2 in the gas phase is measured. The concentration of CO_2 in the gas phase is used with Henry's Law and the Ideal Gas Law to determine the number of moles of carbon in the liquid and gas phases. These numbers are summed and divided by the mass of the injected sample to give the seawater DIC concentration in units of moles per unit mass.

3.2. Measurement Procedure

The DIC measurement method relies on infrared detection of the mole fraction of CO_2 in air, denoted xCO_2, in units of parts per million (ppm). At the start of each sample measurement, the infrared detector (Li-820) performs a two point calibration at 0ppm xCO_2 and at a higher xCO_2 value near 1000ppm; dependent on the calibration gas used. Calibration prior to each measurement is required because the Li-820 response is temperature dependent and the sensor's temperature stabilization mechanism is disabled to reduce power consumption. For the zero calibration, air inside the system is re-circulated in the Zero Loop through CO_2-scrubbing soda lime (**Figure 1A**). The air pump is turned off after 30 seconds of circulation, allowing the system to return to atmospheric pressure, and the detector is zeroed. For the high xCO_2 calibration, a compressed

calibration gas is flushed through the Li-820 optical chamber in the Span Pathway (**Figure 1B**). Gas flow is turned off after 30 seconds, the system returns to atmospheric pressure and the detector's calibration function is initiated.

After the Li-820 is calibrated, acid is pumped through a calibrated-volume (~200µL) tubing loop on a ten-port valve until the loop has been flushed and filled. The acid is then injected into an equilibration chamber and air is bubbled through the acid and recirculated in the Zero Loop until all of the CO_2 is stripped from the acid and air. Seawater from the ocean surface is pumped through a copper-nickel housed 150µm intake filter, where it mixes with tributyl tin from an anti-biofoulant puck, and into a ~1mL calibrated-volume tubing loop on the ten-port valve. The sample tubing loop is thoroughly flushed (~30 volumes) with seawater before the sample is collected and injected into the equilibration chamber where it mixes with the acid. As the seawater and acid mix inside of the equilibration chamber, the pH falls to ~3.5 causing DIC in solution to shift from being mostly bicarbonate to mostly (>99%) CO_2. This rapid transformation of nearly all DIC into the CO_2 form causes CO_2 to escape from the solution into the gas phase. Air inside the instrument that was previously stripped of CO_2 is bubbled through the acidified mixture and recirculated in the Equilibration Loop (**Figure 1C**) for ~5 minutes to facilitate the transfer of CO_2 from the liquid into the gas phase. At the conclusion of this process, CO_2 in the gas phase has reached equilibrium with CO_2 in the acidified liquid sample, and only a small fraction (~1.4%) of the DIC originating from the seawater sample remains in solution, primarily as CO_2. Once equilibrium has been reached, the air circulation pump is turned off and the xCO_2 of the gas phase is measured by the Li-820 at atmospheric pressure. The acidified sample is then ejected from the equilibration

chamber through the Evacuation Pathway (**Figure 1D**). Air in the system is stripped of CO_2 before the system is put into an idle rest state until the next sample measurement.

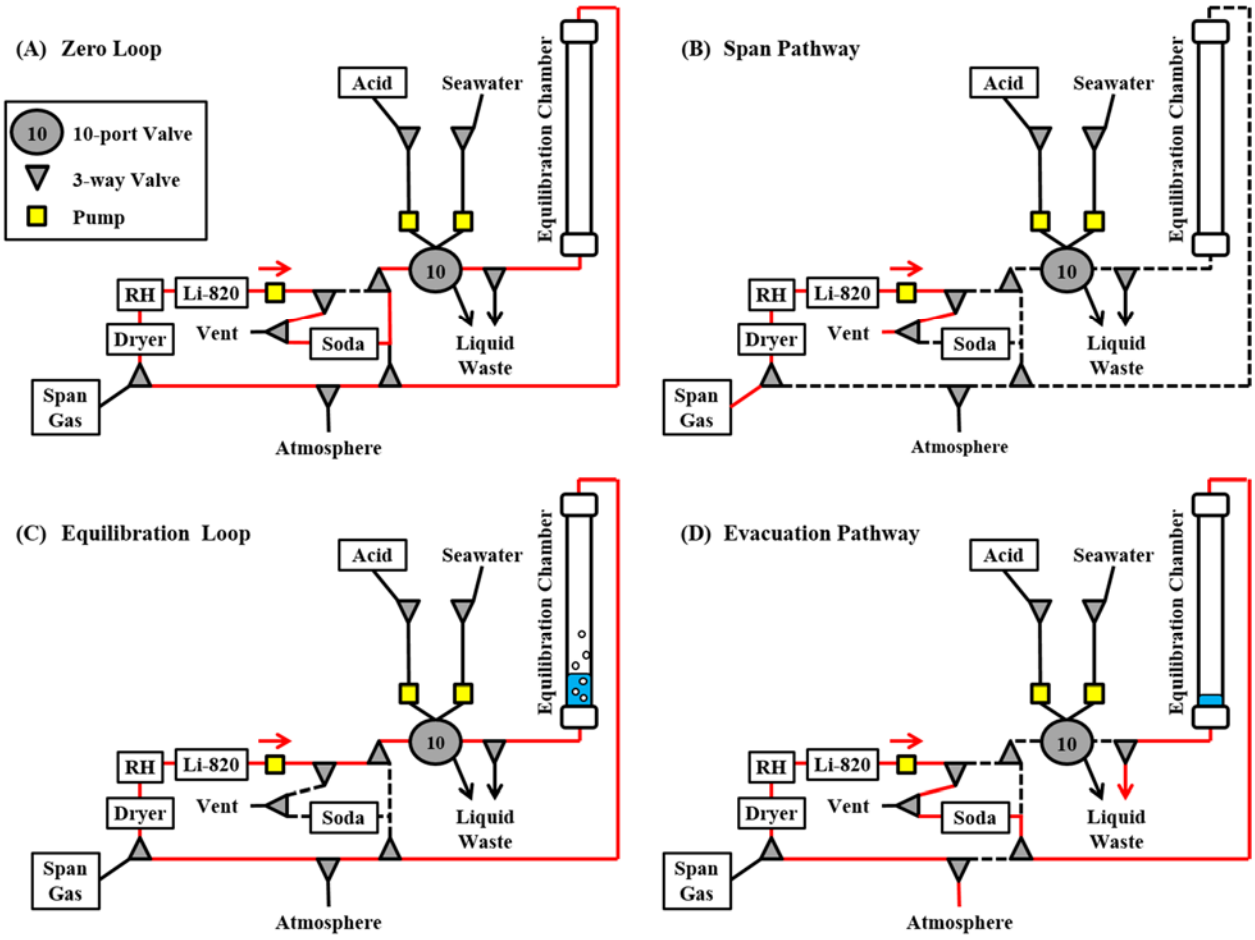

Figure 1. Diagrams of the DIC instrument (**A**) Zero Loop, (**B**) Span Pathway, (**C**), Equilibration Loop (**D**) and Evacuation Pathway with gas pathways highlighted in red. A silica gel dryer (Dryer), relative humidity sensor (RH), infrared gas analyzer (Li-820), and two soda lime columns (Soda) can be found along the air flow pathways. Liquid and air flows are controlled by multiple 3-way solenoid latching valves, a ten-port valve, and three diaphragm pumps. Liquids are pumped into the Equilibration Chamber where air is bubbled through the liquid during specific sequences of the measurement cycle. Components housed within the instrument are enclosed in solid boxes in the diagram, while waste and external materials are not.

3.3. Calculation of DIC

The sample DIC concentration is calculated by summing the number of moles of CO_2 in the gas and liquid phases at equilibrium and dividing by the mass of the injected sample. The Ideal Gas Law is used to determine the number of moles of CO_2 in the gas phase (n_{gas}). Because CO_2 is not an ideal gas, we calculate the fugacity of CO_2 (fCO_2; atm), which is a parameter that takes into account intermolecular interactions that occur between non-ideal gas molecules (**Eq. 1**). This correction relies on the temperature dependent virial coefficients B and δ, the ideal gas constant (R), and Li-820 measurements of temperature (T), pressure (P), and xCO_2 [*Dickson et al.*, 2007]. The Ideal Gas Law may then be applied using fCO_2, R, T, and the laboratory calibrated Equilibration Loop Volume (V_{eq}) to determine the number of moles of CO_2 in the gas phase (**Eq. 2**).

$$fCO_2 = xCO_2 \times P \times \exp[((B + 2\times\delta) \times P) / (R\times T)] \quad \textbf{Eq. 1}$$

$$n_{gas} = (fCO_2 \times V_{eq}) / (R\times T) \quad \textbf{Eq. 2}$$

Henry's Law is used to calculate the concentration of CO_2 ($[CO_2]$; mol kg^{-1}) in the acidified liquid sample at equilibrium with the gas phase (**Eq. 3**). Henry's constant (K_H; mol kg^{-1} atm^{-1}) is dependent on temperature and salinity [*Weiss*, 1974], so measurements from an external conductivity temperature depth (CTD) recorder are used along with temperature readings from a thermometer housed inside the base of the equilibration chamber to compute K_H for each sample measurement. The number of moles of CO_2 in the liquid phase (n_{liquid}) is equal to the product of $[CO_2]$ and the mass of liquid (kg) in the equilibration chamber (**Eq. 4**). The mass of liquid in the

equilibrator is derived from empirically determined sample and acid loop volumes (v_{sample}, v_{acid}; m^3) and calculations of *in situ* seawater and acid density (σ_{sw}, σ_{acid}; $kg\,m^{-3}$).

$$[CO_2] = K_H \times fCO_2 \quad \textbf{Eq. 3}$$

$$n_{liquid} = (\sigma_{sw} \times v_{sample} + \sigma_{acid} \times v_{acid}) \times [CO_2] \quad \textbf{Eq. 4}$$

The seawater DIC concentration (mol kg^{-1}) is determined by summing the moles of carbon in the liquid and gas phases and dividing by the mass of the injected sample (Eq. 5).

$$DIC = (n_{gas} + n_{liquid}) / (\sigma_{sw} \times v_{sample}) \quad \textbf{Eq. 5}$$

3.4. Laboratory Calibration

The primary sensing device on the MADIC system, the Li-820, is calibrated *in situ* before every sample run. In addition, three sensor volumes are measured in the laboratory prior to deployment. These include the sample addition volume (v_{sample}), acid addition volume (v_{acid}), and gas volume of the Equilibration Loop (V_{eq}). To make repeatable volume additions of acid and seawater to the equilibration chamber for each sample measurement, a ten-port valve with fixed volume tubing-loops and two distinct flow pathways is utilized (see Supporting Information). Sample and acid addition volumes are determined gravimetrically in the laboratory.

The volume of the Equilibration Loop (V_{eq}) is determined by connecting the loop to a Ruska high-speed digital pressure controller (Ruska Series 7250xi) and injecting a discrete volume of air from a NIST traceable calibrated Hamilton gastight syringe (Hamilton Gastight model 1025TLL).

The injection causes pressure in the airtight Equilibration Loop to increase and the Ideal Gas Law can be used to determine the loop volume from this pressure change. Although air is not an ideal gas mixture, it behaves nearly identical to an ideal gas near a pressure of 1atm and temperature of 25°C, hence a correction is unnecessary.

3.5. System Components and Reagents

The MADIC system was modified from the PMEL MAPCO$_2$ design [*Sutton et al.*, 2014] to meet the DIC measurement methodology requirements, and is nearly identical in size, weight and mounting platform requirements. System components include an infrared gas analyzer, relative humidity and temperature sensor and a 10-port valve that controls acid and sample addition volumes. Approximately 750mL of 8.5% phosphoric acid is housed within the instrument for sample acidification. Pumps and 3-way latching solenoid valves are used to control fluid and gas flow during different measurement sequences. A CTD, compressed gas cylinder (traceable to World Meteorological Organization standards), battery pack, and antenna are mounted on the buoy and data are transmitted to PMEL after every two measurements through two way Iridium satellite communication. Detailed information about the system components and acid storage can be found in the Supporting Information.

3.6. Instrument Accuracy

DIC sensor accuracy is highly dependent on laboratory calibration. The volumes v_{sample}, v_{acid} and V_{eq} were determined to accuracies of ±0.34%, ±0.69%, and ±0.32% respectively. Sensitivity of the DIC calculation to these errors was determined using a Monte Carlo approach (n=1000).

The calculation is most sensitive to the v_{sample} and V_{eq} accuracies, which result in theoretical DIC calculation uncertainties of ±6.5 μmol kg^{-1}.

The DIC sensor was accuracy tested in the laboratory by running replicate samples of seawater poisoned with mercuric chloride that was previously analyzed for DIC to ±2 μmol kg^{-1} via coulometry. The reference seawater was measured every three hours for three days (n = 23) yielding a standard deviation of ±5 μmol kg^{-1}. The primary source of measurement error during laboratory testing came from inconsistent volumes of liquid being retained in the equilibration chamber between samples. The residual liquid droplets influence V_{eq} and the overall liquid volume between samples, resulting in a combined error that is less than the theoretical DIC error.

4. Results and Discussion

4.1. *Field Testing – Seattle Aquarium*

The MADIC sensor was first field tested in waters from Washington State's productive Puget Sound estuary using a flow-through system housed in the pump room of the Seattle Aquarium (see Supporting Information). Water from ~12m depth was pumped through a 150μm mesh filter before entering the flow-through system. The DIC sensor, a Seabird Electronics 16plus V2 SeaCAT CTD recorder and a Sami-2 pH unit collected samples every three hours while a wall mounted General Oceanics CO_2 gas analyzer 7000 took xCO_2 measurements every two minutes over the course of one month. 20 discrete bottle samples were collected throughout the deployment and analyzed for DIC to an accuracy of ±2 μmol kg^{-1} via coulometry at PMEL and are considered to be the highest quality data in this analysis.

In situ DIC measurements are shown in **Figure 2A** with bottle sample values overlain. The mean difference between MADIC measurements and bottle samples was -6±11 μmol kg^{-1}, indicating that there was not a statistically significant measurement bias. The Sami-2 pH and General Oceanics CO_2 gas analyzer 7000 sensors have manufacturer stated accuracies of ±0.003 pH units and ~±4 μatm (±1%) respectively. *In situ* measurements of pH and xCO_2 (**Figure 2B, 2C**) were used to calculate DIC concentrations with the program CO_2sys [*van Heuven et al.*, 2011] using constants from *Lueker et al.*, (2000) and *Dickson*, (1990). The calculated DIC values (**Figure 2A)** have a range of over 300 μmol kg^{-1}; significantly larger than the range observed by the MADIC sensor and bottle samples. The average difference between the calculated DIC values and the bottle samples is 52±93 μmol kg^{-1}.

The notable bias in calculated DIC values may be caused by different residence times in the pH and xCO_2 sensor flow-through systems. Due to the very strong co-variance of the pH-xCO_2 pair, the calculated DIC is extremely sensitive to any difference in sampling rates between the two sensors, particularly during rapid changes in seawater carbonate chemistry [*Cullison Gray et al.*, 2011]. To evaluate the utility of coupling the measured DIC with the other commercially available autonomous sensors, *in situ* DIC and pH values were used to calculate xCO_2 and the DIC-xCO_2 pair was used to calculate pH for comparison with the measurements. The calculated xCO_2 and pH values (**Figure 2B, 2C**) show good agreement with the respective measured values, indicating that calculations of pH and xCO_2 from DIC paired with either of these parameters can reproduce the environmental conditions well, even when considering the flow through system limitations. This highlights the value of directly measuring DIC.

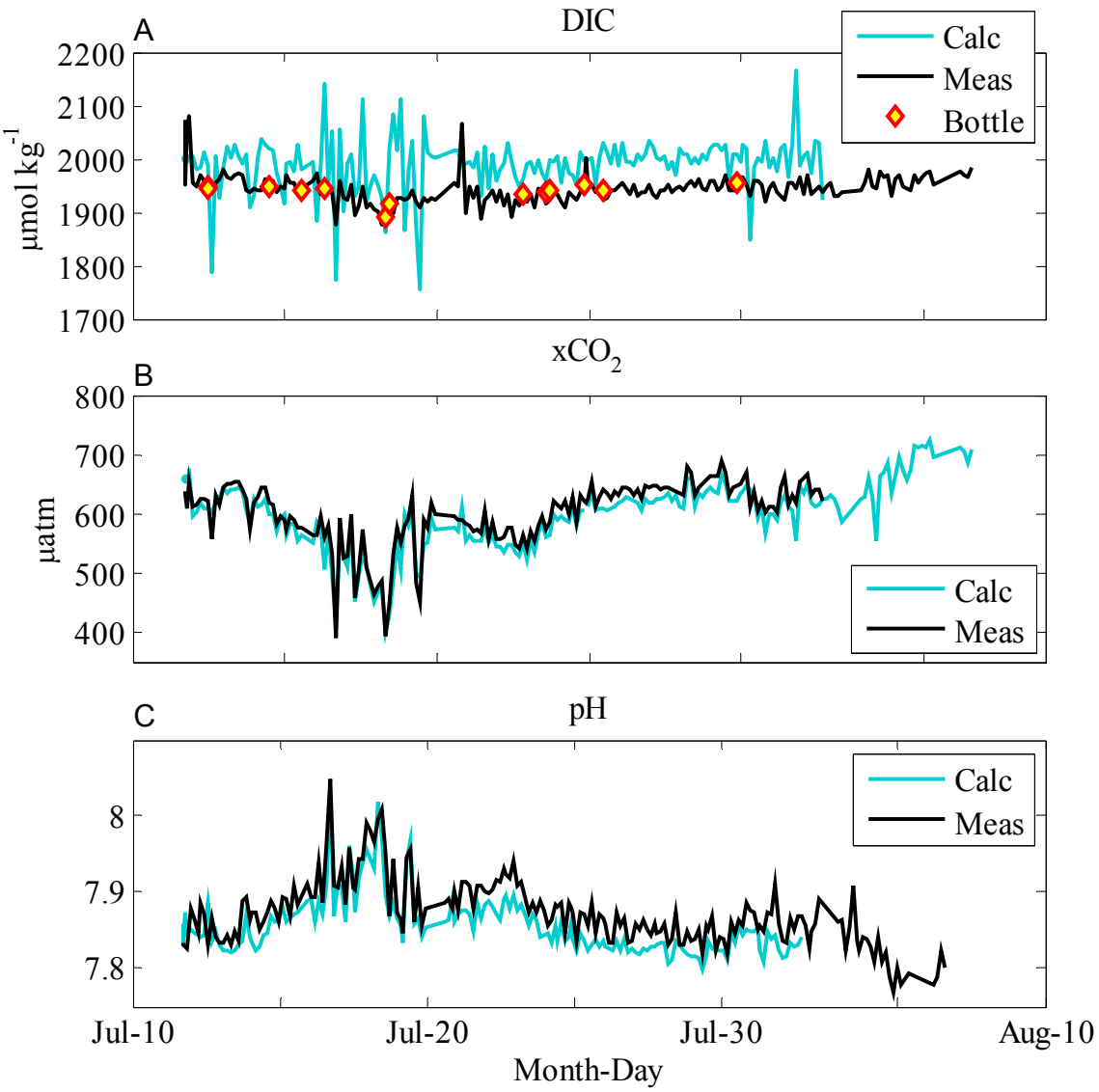

Figure 2. Results from the Seattle Aquarium deployment for **(A)** DIC (µmol kg^{-1}), **(B)** xCO_2 (µatm) interpolated onto the DIC sample times, and **(C)** pH. Black lines in each panel show in situ sensor measurements (Meas). Teal lines in each panel are values calculated (Calc) from the other two measured parameters using the program CO_2sys. Yellow diamonds in subplot **A** show discrete bottle sample DIC concentrations measured via coulometry to an accuracy of ±2 µmol kg^{-1}.

4.2. Field Testing – Honolulu, HI

After successful testing in an estuarine environment, the DIC sensor was deployed in a fringing reef environment outside of Kewalo Harbor in Honolulu, HI on October 31, 2013. The MADIC buoy was deployed ~400m from shore in ~13.5m of water and ~25m from an existing MAPCO_2

buoy operated by the University of Hawaii and PMEL. A Seabird Electronics 16plus V2 SeaCAT CTD recorder and a Sami-2 pH unit were mounted on the buoy bridle. *In situ* measurements were taken every three hours for seven months and were timed synchronously with the neighboring $MAPCO_2$ buoy measurements. The buoy and sensors were left unattended for the entire seven month duration of this completely autonomous field test.

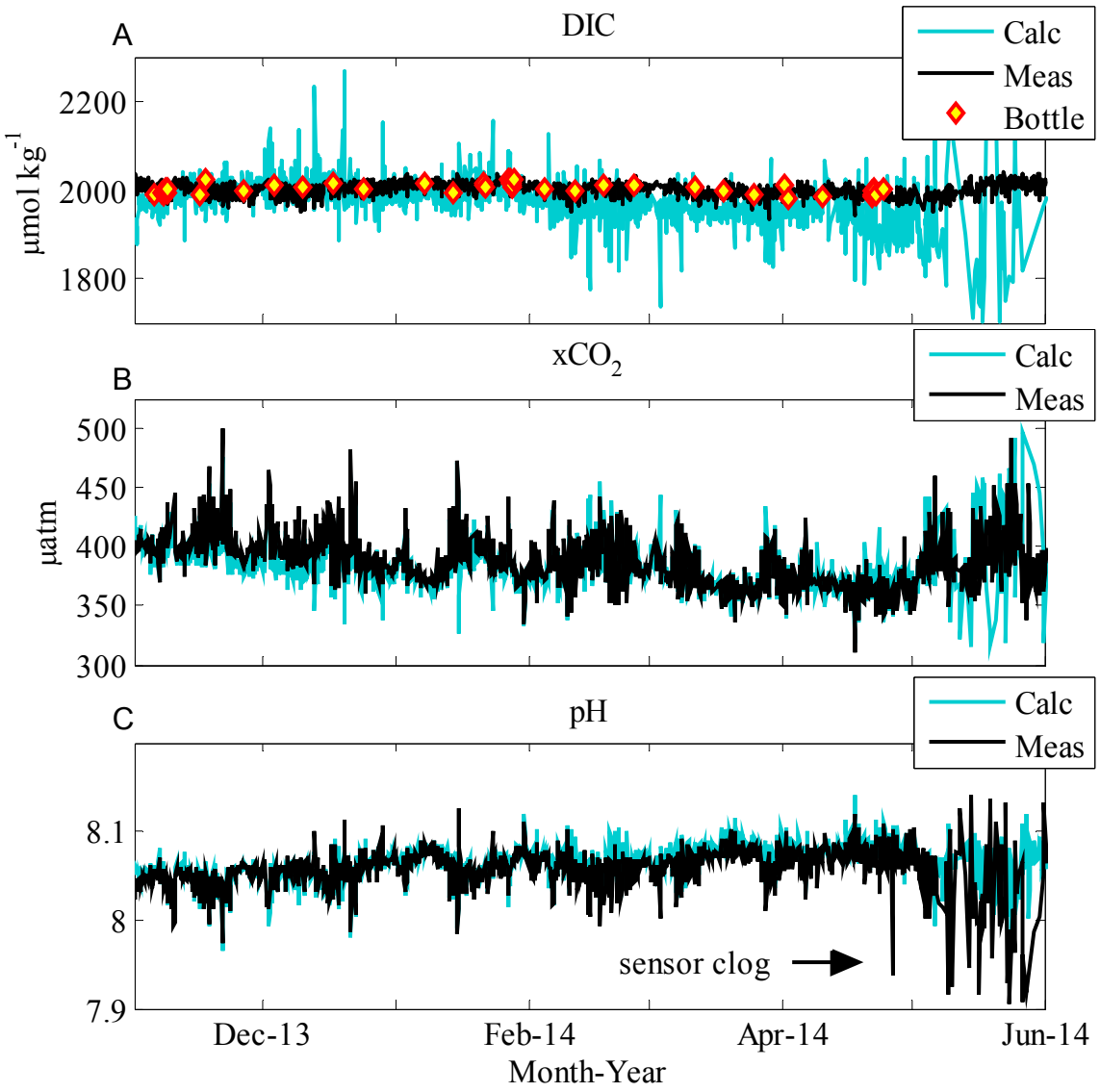

Figure 3. Results from the Honolulu deployment for **(A)** DIC (µmol kg^{-1}), **(B)** xCO_2 (µatm), and **(C)** pH. Black lines in each panel show in situ sensor measurements (Meas). Teal lines in each panel are values calculated (Calc) from the other two measured parameters using the program CO_2sys. Yellow diamonds in subplot **A** show discrete bottle sample DIC concentrations measured via coulometry to an accuracy of ±2-3 µmol kg^{-1}.

Throughout the deployment, 51 discrete bottle samples were collected next to the $MAPCO_2$ buoy and analyzed for DIC concentration via coulometry at the University of Hawaii to an accuracy of ±2-3 μmol kg^{-1}. Early in the DIC sensor deployment, the Licor-820 source lamp began to fail, causing the xCO_2 measurements to drift over time. The data were de-trended using a linear least squares regression to account for this drift and a small non-linear temperature correction was applied (average influence of 1.4ppm). The resulting DIC measurements and discrete bottle sample concentrations are shown in **Figure 3A**. The mean difference between the DIC sensor measurements and bottle samples is -1±11 μmol kg^{-1}, indicating that the MADIC sensor did not show a statistically significant measurement bias throughout the deployment.

The deployment location was selected for three reasons. Stable seawater carbon chemistry conditions in this region were ideal for testing sensor stability over time [*Drupp et al.*, 2013]. The near shore deployment location made it possible to collect discrete bottle samples via kayak twice per month, with three additional higher frequency (every three hours for 24 hours) sample collection periods. Finally, colocation of the existing $MAPCO_2$ buoy provided an ideal opportunity to measure three carbonate system parameters continuously over a seven month period for thorough evaluation of the MADIC sensor field performance.

The Sami-2 pH sensor has a manufacturer stated accuracy of ±0.003 pH units and the $MAPCO_2$ system has a field accuracy of ±2 μatm [*Sutton et al.*, 2014]. *In situ* measurements of pH and xCO_2 (**Figure 3B, 3C**) were used to calculate DIC concentrations with the program CO_2sys [*van Heuven et al.*, 2011] using constants from *Lueker et al.*, (2000) and *Dickson*, (1990). The calculated DIC

values (**Figure 3A**) range over 400 μmol kg^{-1}, well beyond the range of DIC concentrations determined from the MADIC sensor and bottle samples. The average difference between the calculated DIC values and the bottle samples is -21±37 μmol kg^{-1}. To determine if these errors were due to sensor malfunction, *in situ* DIC and pH (xCO_2) values were used to calculate xCO_2 (pH) for comparison with the sensor measurements.

The good agreement between calculated and measured values for xCO_2 and pH (**Figure 3B, 3C**) suggests that both sensors were performing well throughout the deployment and that the large errors in calculated DIC are not from sensor malfunction. A sustained decrease in the calculated DIC values begins when the measured and calculated pH values start to deviate. This suggests that Sami-2 pH sensor measurements may have been biased low during the second half of the deployment, likely due to bio-fouling near the sensor intake, which was covered in growth upon sensor recovery. Higher-frequency errors in calculated DIC may have been caused by differences in the water being sampled by the pH and xCO_2 sensors, which were mounted on buoys ~25m apart. Very small differences in seawater carbon characteristics due to horizontal heterogeneity can cause pH and xCO_2 to become uncorrelated [*Cullison Gray et al.*, 2011], leading to DIC calculation errors >100 μmol kg^{-1}. It is possible that better results could be achieved by mounting the sensors on the same buoy; however, it is also likely that this would not result in climate-quality computations of DIC. Improving the accuracy of pH and xCO_2 sensors and fine tuning sampling protocols for simultaneous measurement timing and duration may eventually make it possible to achieve high-quality calculated DIC estimates [*Johnson et al.*, 2009]; however, the challenge of further improving autonomous pH and xCO_2 sensor accuracies has limited the utility of this pair for carbon cycle analyses thus far. Direct measurement of DIC with either xCO_2 or pH would

eliminate the need for such challenging sensor advances while producing the quality of data needed to accurately constrain the carbonate system.

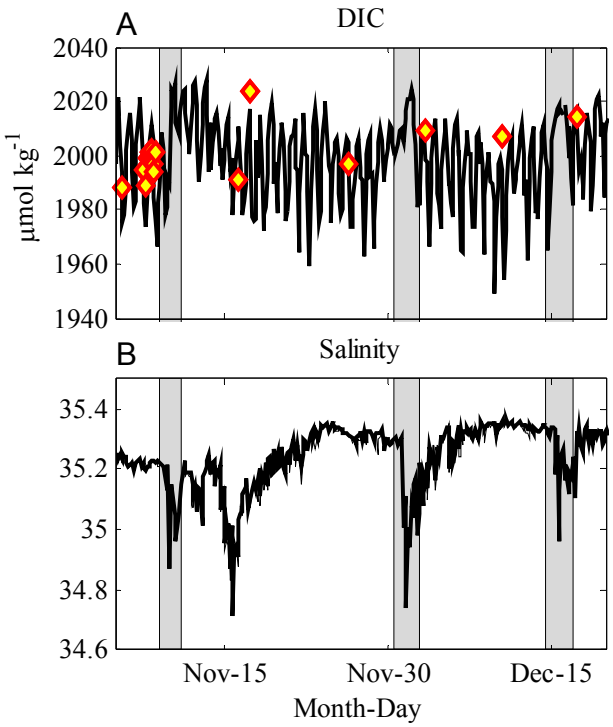

Figure 4. In situ **(A)** DIC (µmol kg^{-1}) and **(B)** salinity measurements during November and December 2013 of the Honolulu field deployment. Yellow diamonds in subplot **a** are DIC bottle sample concentrations. Grey regions highlight elevated DIC concentrations associated with rain events.

Weekly to monthly DIC variability during the deployment largely tracked water mass changes, where the low-pass filtered DIC concentrations were positively correlated to seawater density. Superimposed on these lower-frequency variations were intermitted rain events that occurred throughout the deployment. Notable increases in surface water xCO_2 and DIC concentrations coinciding with some of these rain events suggests that nearby marinas and land were occasionally acting as sources of carbon to the near shore marine environment (**Figure 4**). This finding agrees well with prior work by *Tomlinson et al.*, (2011) near the Ala Wai Canal who identified elevated nutrient and suspended particulate matter concentrations during the first pulse of stormwater

runoff. Based on xCO_2 data alone, it would be challenging to determine whether the observed increases in xCO_2 during storms were caused by low pH levels in the runoff or by high concentrations of total inorganic carbon. With the DIC sensor measurements it is clear that the freshwater runoff contained more total inorganic carbon (DIC) than ambient seawater, and that a transfer of carbon from land to sea was occurring.

In addition to the lower-frequency and intermittent DIC variability, a distinct diel cycle was observed at this location, where DIC values were lower during the day and higher at night with an average cycle magnitude of 17.5 μmol kg^{-1} (**Figure 5**). Higher diel cycle amplitudes, as previously described by *Drupp et al.*, (2013) for other parameters, were observed for DIC during periods of low wind speed (<2m s^{-1}). This suggests a strong link between the mixed layer stratification that occurs in association with low winds and the magnitude of the diel DIC cycle, as CO_2 gas exchange was found to be negligible in this location under such conditions. *In situ* oxygen (O_2) data from the MAPCO_2 buoy (unpublished data) were used to estimate primary productivity and respiration contributions to the daily DIC cycle. O_2 saturation was calculated using the empirical relationship of *Garcia and Gordon*, (1992) and the difference between observed O_2 and calculated O_2 saturation (the O_2 anomaly) is assumed to be a lower bound estimate on primary production and respiration because we neglect the effect of O_2 gas exchange. The O_2 anomaly was converted to units of carbon using ratios from *Anderson and Sarmiento*, (1994) and the results indicate that, at most times, less than 50% of the observed daily DIC cycle can be attributed to primary production and respiration. The most likely explanation for the remaining portion of the daily DIC cycle at this site is diurnal variations in calcium carbonate ($CaCO_3$) processes in this fringing reef environment.

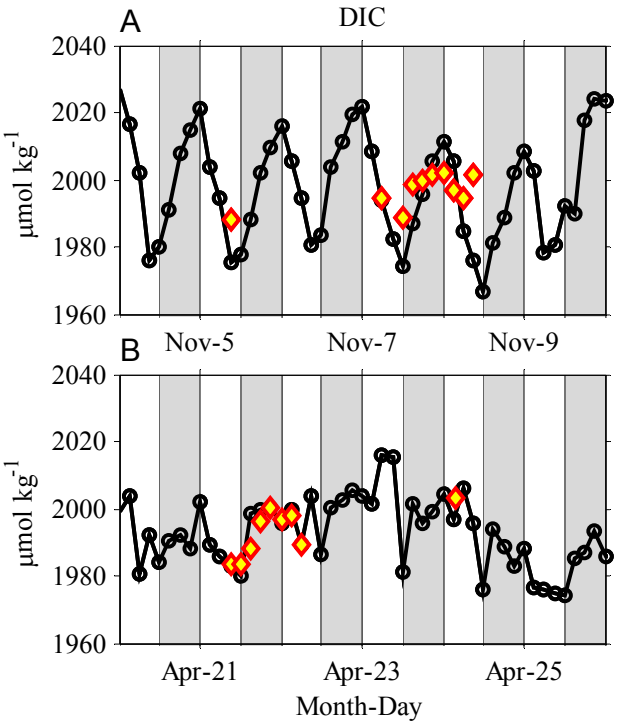

Figure 5. Zoom in on two 6 day periods of the Honolulu DIC (µmol kg^{-1}) time series; (**A**) one at the start of the deployment in 2013 and (**B**) one near the end of the deployment in 2014. Grey bars indicate night time (8pm-8am local time) and yellow diamonds show DIC bottle sample concentrations.

During the day, $CaCO_3$ precipitation and photosynthesis cause a decrease in the concentration of DIC while at night $CaCO_3$ dissolution and respiration cause an increase in the concentration of DIC. The combined effect of these processes is what controls the large daily DIC cycle observed at this location. This was not quantitatively predictable from xCO_2 and (semiquantative) O_2 time series data alone because $CaCO_3$ precipitation results in an increase in xCO_2 (due to the reduction in CO_3^{2-} concentration), which counteracts the effect of xCO_2 reductions caused by photosynthesis. Similarly, $CaCO_3$ dissolution results in a decrease in the xCO_2 concentration of seawater while respiration causes xCO_2 to increase. The opposing effects of these processes result in a muted and more erratic xCO_2 daily cycle. As a result, the MADIC sensor was especially informative in this environment where both primary production and calcium carbonate processes are occurring.

4.3. Implications

Results from the first two field deployments of the MADIC sensor indicate that DIC sensor measurements are ~90% more accurate than calculations of DIC from *in situ* measurements of pH and xCO_2. The MADIC sensor did not show any signs of measurement bias during the two deployments and provided new insights about seawater carbon chemistry not obtainable from the pH or xCO_2 sensors alone, or when paired together. The MADIC sensor was robust throughout seven months of unattended field operation, and was still functioning properly at the time of recovery.

Many investigators have engaged in the development of autonomous marine carbon sensors that can be used to better constrain ocean carbon storage and learn about complex carbon cycle feedback mechanisms. As advancement continues, careful consideration of the long-term utility and robustness of these sensors is needed. A growing emphasis on carbon cycle research in coastal seas and high latitude oceans, where freshwater input and sea ice melt can dramatically influence the characteristics of seawater, brings new challenges to the carbon cycle community. pH and TA are carbonate system parameters that have been defined by charge balances that are themselves based on various assumptions about seawater composition that may not hold true in these regions [*Dickson et al.*, 2007]. Direct measurement of DIC can provide clearer information in areas where riverine and freshwater fluxes result in complex carbonate chemistry and observed variations are outside of the range of modern empirically derived definitions and equilibrium constants.

Air-sea CO_2 fluxes have been a powerful way to constrain ocean CO_2 uptake [*Takahashi et al.*, 2009]; however, the ultimate goal is to describe changes in the carbon storage of the ocean. As the

integrator of all processes influencing seawater inorganic carbon chemistry, DIC is the master variable for ocean carbon storage and cycling studies. Continuous observations of DIC coupled with pH or xCO_2 will make it possible to unravel carbon dynamics in complex and highly variable systems that require continuous monitoring in order to quantify their contribution to the global carbon budget. These systems include areas influenced by rivers or sea ice, coastal upwelling, and areas with significant calcium carbonate production. In such regions, the integrating power of autonomous high-frequency determinations of DIC, which is not biased by carbonate system speciation shifts that can complicate interpretation of pH and xCO_2 signals, will be a powerful measurement tool for studying marine carbon cycling.

5. Acknowledgements

This work was funded by the NOAA Ocean Acidification and Global Carbon Cycle Programs and the NSF IGERT Program on Ocean Change. The authors thank our collaborators at the Settle Aquarium, the Battelle Memorial Institute and at the University of Hawaii including: Ryan Tabata, Patrick Drupp, Jeff Jaeger and Gerianne Terlouw. We also thank our numerous collaborators at PMEL including: Richard Feely, Geoff Lebon, Cathy Cosca, Patrick McLain, Dirk Tagawa, Danna Greeley, Sylvia Musielewicz, Randy Bott, and Joseph Resing. This is PMEL contribution number 4234.

6. Supporting Information

6.1. Reagents

The MADIC system relies on the use of 8.5% phosphoric acid (H_3PO_4) to acidify each seawater sample. Approximately 0.75L of 8.5% H_3PO_4 is contained within a Tedlar bag with a Tedlar

compression tube fitting (Pollution Measurement Corporation, Oak Park, Illinois). This bag is enclosed within a liquid tight Seal Line Padded Storm Sack (Cascade Designs, Inc., Seattle, Washington) to protect the Tedlar bag during the deployment. The acid bag is positioned in the base of the instrument housing and is connected directly to a pump with PTFE tubing and Upchurch Scientific fittings.

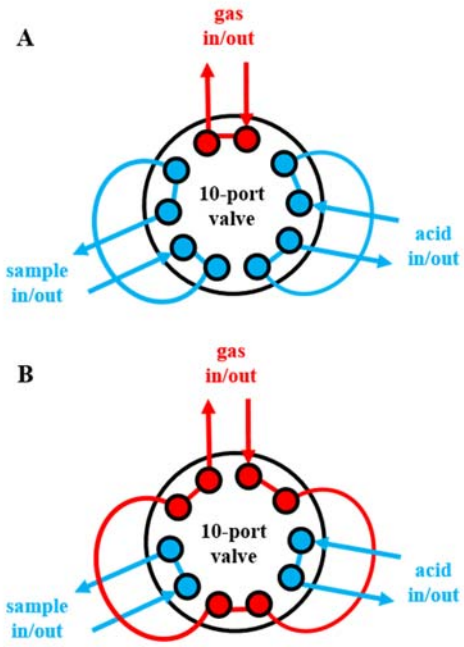

Figure S1. 10-port valve flow pathways used to control sample and acid additions. The sample and acid loops are filled when the valve is in position **a**. The valve is then switched to position **b** to inject the fluid into the equilibration chamber. Loops are not drawn to scale.

6.2. System Components

The MADIC system was modified from the PMEL MAPCO$_2$ design[*Sutton et al.*, 2014] to meet the DIC measurement methodology requirements, and is nearly identical in size, weight and mounting platform requirements. The sensor is comprised of two ~1m x 15cm cylindrical towers that house the major components of the instrument. The electronics tube contains the infrared gas analyzer (Li-820, Biogeosciences, Incorporated, Lincoln, Nebraska) and a relative humidity and

temperature sensor (SHT71, Sensirion AG, Switzerland). Six ASCO 3-way latching solenoid valves and a Thomas 3003-0312 Pump are used to control gas pathways and flow during different sequences of the measurement. The equilibrator tube contains a ten-port valve and its controller (ASCO Valve, Inc., Florham Park, New Jersey), acid, and a 30cm cylindrical PTFE tube equilibration chamber with an internal diameter (ID) of ~9.5mm. A Seabird Electronics 38 thermometer is housed (without its case) inside the base of the equilibration chamber to record the temperature of the acidified sample at the time of measurement. Three Takasago 3-way latching solenoid valves are used to control fluid pathways in the equilibrator tube and two KNF Neuberger, Inc. miniature liquid diaphragm pumps are used to pump the acid and seawater sample during measurement cycles. Gas flow pathways linking the electronics and equilibrator tubes are made of ~1.6mm ID Zeus PTFE tubing with a small portion of ~1.6mm ID Nalgene PVC tubing outfitted with Upchurch Scientific fittings (IDEX health and Science LLC, Oak Harbor, Washington). A Seabird Electronics 16plus V2 SeaCAT CTD collects salinity and temperature measurements that are used to calculate the density values needed for sample DIC computation. A compressed gas cylinder (traceable to World Meteorological Organization standards), battery pack, and antenna are mounted on the buoy and instrument data are transmitted back to PMEL after every two sample measurements through two way Iridium satellite communication.

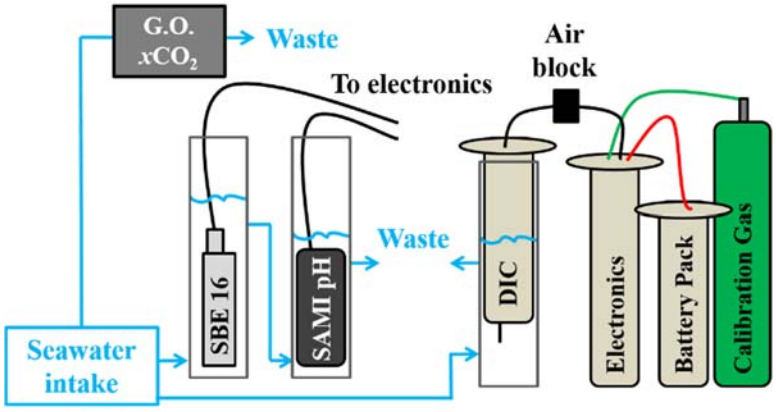

Figure S2. Diagram of the Seattle Aquarium flow-through system. Water from ~12m depth was pumped through a valve manifold that fed into the three flow-through pathways depicted. Discrete bottle samples were collected from a valve on the manifold for later coulometric DIC analysis.

7. References

Anderson, L. A., and J. L. Sarmiento (1994), Redfield ratios of remineralization determined by nutrient data analysis, *Global Biogeochem. Cycles*, *8*(1), 65–80.

Bandstra, L., B. Hales, and T. Takahashi (2006), High-frequency measurements of total CO_2: Method development and first oceanographic observations, *Mar. Chem.*, *100*, 24–38, doi:10.1016/j.marchem.2005.10.009.

Broecker, W. S., and T. Takahashi (1966), Calcium carbonate precipitation on the Bahama Banks, *J. Geophys. Res.*, *71*(6), 1575–1602, doi:10.1029/JZ071i006p01575.

Cullison Gray, S. E., M. D. DeGrandpre, T. S. Moore, T. R. Martz, G. Friederich, and K. S. Johnson (2011), Applications of in situ pH measurements for inorganic carbon calculations, *Mar. Chem.*, *125*, 82–90, doi:10.1016/j.marchem.2011.02.005.

Dickson, A., C. Sabine, and J. Christian (Eds.) (2007), *Guide to best practices for ocean CO_2 measurements*, PICES Special Publication 3, 191 pp.

Dickson, A. G. (1990), Standard potential of the reaction : $AgCl_{(s)} + 1/2H_{2(g)} = Ag_{(s)} + HCl_{(aq)}$, and the standard acidity constant of the ion HSO_4^- in synthetic sea water from 273.15 to 318.15 K, *J. Chem. Thermodyn.*, (22), 113–127.

Dickson, A. G., and J. Riley (1978), The effect of analytical error on the evaluation of the components of the aquatic carbon-dioxide system, *Mar. Chem.*, *6*, 77–85, doi:10.1016/0304-4203(78)90008-7.

Drupp, P. S., E. H. De Carlo, F. T. Mackenzie, C. L. Sabine, R. A. Feely, and K. E. Shamberger (2013), Comparison of CO2 Dynamics and Air–Sea Gas Exchange in Differing Tropical Reef Environments, *Aquat. Geochemistry*, *19*(5-6), 371–397, doi:10.1007/s10498-013-9214-7.

Evans, W., B. Hales, and P. G. Strutton (2011), Seasonal cycle of surface ocean pCO_2 on the Oregon shelf, *J. Geophys. Res.*, *116*, doi:10.1029/2010JC006625.

Friedrich, T., and A. Oschlies (2009), Neural network-based estimates of North Atlantic surface pCO_2 from satellite data: A methodological study, *J. Geophys. Res.*, *114*, doi:10.1029/2007JC004646.

Garcia, H. E., and L. I. Gordon (1992), Oxygen solubility in seawater: Better fitting equations, *Limnol. Oceanogr.*, *37*(6), 1307–1312, doi:10.4319/lo.1992.37.6.1307.

Gledhill, D., R. Wanninkhof, and C. M. Eakin (2009), Observing ocean acidification from space, *Oceanography*, *22*(4), 48–59, doi:10.5670/oceanog.2009.96.

Goulden, P. D. (1976), Automated determination of carbon in natural waters, *Water Res.*, *10*, 487–490, doi:10.1016/0043-1354(76)90183-4.

Goyet, C. (1994), High-accuracy measurements of total dissolved inorganic carbon in the ocean: comparison of alternate detection methods—a reply, *Mar. Chem.*, *48*, 89–90.

Goyet, C., and A. K. Snover (1993), High-accuracy measurements of total dissolved inorganic carbon in the ocean: comparison of alternate detection methods, *Mar. Chem.*, *44*(2-4), 235–242, doi:10.1016/0304-4203(93)90205-3.

Hales, B., D. W. Chipman, and T. Takahashi (2004), High-frequency measurement of partial pressure and total concentration of carbon dioxide in seawater using microporous hydrophobic membrane contractors, *Limnol. Oceanogr.*, *2*, 356–364.

Hales, B., L. Karp-Boss, A. Perlin, and P. A. Wheeler (2006), Oxygen production and carbon sequestration in an upwelling coastal margin, *Global Biogeochem. Cycles*, *20*(3), doi:10.1029/2005GB002517.

Hales, B., P. G. Strutton, M. Saraceno, R. Letelier, T. Takahashi, R. A. Feely, C. L. Sabine, and F. P. Chavez (2012), Satellite-based prediction of pCO_2 in coastal waters of the eastern North Pacific, *Prog. Oceanogr.*, *103*, doi:10.1016/j.pocean.2012.03.001.

Hamme, R. et al. (2010), Volcanic ash fuels anomalous plankton bloom in subarctic northeast Pacific, *Geophys. Res. Lett.*, *37*, doi:10.1029/2010GL044629.

Van Heuven, S. M. A. C., D. Pierrot, J. W. B. Rae, E. Lewis, and D. W. R. Wallace (2011), MATLAB Program Developed for CO_2 System Calculations, *ORNL/CDIAC-105b. Carbon Dioxide Inf. Anal. Center, Oak Ridge Natl. Lab. U.S. Dep. Energy, Oak Ridge, Tennessee*. Available from: http://cdiac.ornl.gov/ftp/co2sys/CO2SYS_calc_MATLAB_v1.1/ (Accessed 2 July 2014)

Johnson, K. S., W. M. Berelson, E. S. Boss, Z. Chase, H. Claustre, S. R. Emerson, N. Gruber, A. Kortzinger, M. J. Perry, and S. C. Riser (2009), Observing biogeochemical cycles at global scales with profiling floats and gliders: Prospects for a global array, , *22*, 216–225, doi:10.5670/oceanog.2009.81.

Kaltin, S., C. Haraldsson, and L. G. Anderson (2005), A rapid method for determination of total dissolved inorganic carbon in seawater with high accuracy and precision, *Mar. Chem.*, *96*, 53–60, doi:10.1016/j.marchem.2004.10.005.

Karl, D. M., E. A. Laws, P. Morris, P. J. Williams, and S. R. Emerson (2003), Metabolic balance of the open sea, *Nature*, *426*, 6962, doi:doi:10.1038/426032a.

Liu, X., R. H. Byrne, L. Adornato, K. K. Yates, E. Kaltenbacher, X. Ding, and B. Yang (2013), In situ spectrophotometric measurement of dissolved inorganic carbon in seawater., *Environ. Sci. Technol.*, *47*, 11106–11114, doi:10.1021/es4014807.

Lueker, T. J., A. G. Dickson, and C. D. Keeling (2000), Ocean pCO_2 calculated from dissolved inorganic carbon, alkalinity, and equations for K_1 and K_2: validation based on laboratory measurements of CO_2 in gas and seawater at equilibrium, *Mar. Chem.*, *70*, 105–119, doi:10.1016/S0304-4203(00)00022-0.

McGillicuddy, D. J., A. Robinson, D. Siegel, H. Jannasch, R. Johnson, T. Dickey, J. McNeil, A. Michaels, and A. Knap (1998), Influence of mesoscale eddies on new production in the Sargasso Sea, *Nature*, *394*, doi:10.1038/28367.

McGillicuddy, D. J. et al. (2007), Eddy/wind interactions stimulate extraordinary mid-ocean plankton blooms., *Science*, *316*(5827), 1021–6, doi:10.1126/science.1136256.

Millero, F. J. (2007), The marine inorganic carbon cycle., *Chem. Rev.*, *107*, 308–341, doi:10.1021/cr0503557.

O'Sullivan, D. W., and F. J. Millero (1998), Continual measurement of the total inorganic carbon in surface seawater, *Mar. Chem.*, *60*, 75–83, doi:10.1016/S0304-4203(97)00079-0.

Salonen, K. (1981), Rapid and precise determination of total inorganic carbon and some gases in aqueous solutions, *Water Res.*, *15*, 403–406, doi:DOI: 10.1016/0043-1354(81)90049-X.

Sayles, F. L., and C. Eck (2009), An autonomous instrument for time series analysis of TCO_2 from oceanographic moorings, *Deep Sea Res. Part I Oceanogr. Res. Pap.*, *56*(9), 1590–1603, doi:10.1016/j.dsr.2009.04.006.

Schuster, U., A. Hannides, L. Mintrop, and A. Körtzinger (2009), Sensors and instruments for oceanic dissolved carbon measurements, *Ocean Sci. Discuss.*, *5*(1), 491–524, doi:10.5194/osd-6-491-2009.

Sutton, A. J. et al. (2014), A high-frequency atmospheric and seawater pCO_2 data set from 14 open ocean sites using a moored autonomous system, *Earth Syst. Sci. Data Discuss.*, *7*, 385–418, doi:10.5194/essdd-7-385-2014.

Takahashi, T. et al. (2009), Climatological mean and decadal change in surface ocean pCO_2, and net sea–air CO_2 flux over the global oceans, *Deep Sea Res. Part II Top. Stud. Oceanogr.*, *56*(8-10), 554–577, doi:10.1016/j.dsr2.2008.12.009.

Tomlinson, M. et al. (2011), Characterizing the effects of two storms on the coastal waters of O'ahu, Hawai'i, using data from the Pacific Islands Ocean Observing System, *Oceanography*, *23*(2), 182–199, doi:10.5670/oceanog.2011.38.

Wang, Z. A., S. N. Chu, and K. a Hoering (2013), High-frequency spectrophotometric measurements of total dissolved inorganic carbon in seawater., *Environ. Sci. Technol.*, *47*, 7840–7847, doi:10.1021/es400567k.

Weiss, R. (1974), Carbon dioxide in water and seawater: the solubility of a non-ideal gas, *Mar. Chem.*, *2*(3), 203–215, doi:10.1016/0304-4203(74)90015-2.

Wong, C. (1970), Quantitative analysis of total carbon dioxide in sea water: A new extraction method, *Deep Sea Res. Oceanogr. Abstr.*, *17*, 9–17, doi:10.1016/0011-7471(70)90084-7.

Chapter 5

Summary of research findings

1. Summary

Biogeochemical drivers of carbon cycling in the surface ocean were quantitatively evaluated from seven years of high-frequency observations at NOAA's Station Papa and Kuroshio Extension Observatory (KEO) moorings. Mixed-layer total alkalinity (TA) and dissolved inorganic carbon (DIC) time series were derived from *in situ* observations of salinity and carbon dioxide (CO_2) and used to diagnostically assess the influence of gas exchange, physical processes, evaporation and precipitation, and biological processes on mixed-layer carbon inventories. This was accomplished using a dual-tracer, mixed-layer mass-balance approach to evaluate the daily evolution of these processes throughout each annual deployment.

Carbon cycling in both regions was dominated by the competing effects of vertical carbon input from diapycnal processes and biological carbon drawdown, and both regions were found to be autotrophic. The annual net community production (NCP), defined as the gross photosynthesis minus the community respiration, is a measure of the carbon export from the ocean surface to the interior and reflects the strength of the biological pump. The mean annual NCP at Ocean Station Papa (OSP) was 1.9 ± 0.5 mol C m^{-2} yr^{-1}, which was less than half of the mean annual NCP found at KEO 4.5 ± 2.2 mol C m^{-2} yr^{-1}. The mean annual calcium carbonate ($CaCO_3$) production at both locations was found to be 0.4 mol C m^{-2} yr^{-1}, though it was not statistically significant at KEO. The finding of an elevated $CaCO_3$ production to NCP ratio at OSP (~0.21 ± 0.1) relative to the

global ocean (~0.06-0.09) adds to a growing body of literature indicating that calcifiers contribute significantly to carbon export in this ocean region.

Seasonal variability was larger than interannual variability in NCP at both moorings, excluding one year at KEO that was particularly anomalous. At KEO, autotrophy is confined to approximately four months during spring, while at OSP autotrophy occurs over nearly seven months from winter to summer. Different durations of productivity reflect dissimilar limitations on primary production. Macronutrient limitation at KEO is relieved seasonally through fall/winter entrainment and is followed by rapid nutrient consumption and exhaustion in spring when light levels are sufficient. At OSP, iron limitation is relieved seasonally by entrainment, but iron is also thought to be supplied through numerous other mechanisms throughout the year, allowing low and slow continuous production. Fall and winter heterotrophy (~1 mol C m^{-2} yr^{-1}) was consistently observed at OSP, and may be fueled by dissolved organic carbon remaining in the water column after the spring and summer productive periods. This seasonal recycling of organic carbon in the mixed layer contributes to the lower annual carbon export in this region. With new understanding of the large seasonality in NCP at these two locations, it follows that summertime estimates of NCP may not be scalable to annual NCP as they lack important information about the peak productive period (spring) and seasonality in ecosystem dynamics (e.g. winter heterotrophy).

KEO and OSP are regions of net atmospheric CO_2 uptake, though this varies seasonally. The timing of NCP largely influences the role of biology in maintaining sea surface CO_2 levels below the atmospheric concentration. Seawater cooling in winter, as well as some productivity at OSP, outcompetes the influence of seasonal entrainment that brings high-CO_2 waters to the sea surface.

As a result, the KEO and OSP regions are sinks for atmospheric CO_2 during winter, though this effect is much larger at KEO. Mismatched timing between spring production and summer heating at KEO means that biological processes do little to directly combat CO_2 increases resulting from seasonal warming, though the biological drawdown of mixed-layer DIC in spring does play a role. This leads KEO to be a source of CO_2 to the atmosphere in summer. At OSP, continuous production throughout the summer warm period substantially lowers sea surface CO_2 concentrations and significantly reduces the seasonal atmospheric CO_2 source strength. Thus, although NCP is smaller at OSP than at KEO on an annual basis, its contribution to the local air-sea CO_2 gas exchange is larger.

In addition to seasonality and timing of NCP, both regions show notable interannual variability in NCP. At KEO, diapycnal processes and biology counteract each other, such that interannual variability in the physical DIC input is reflected in the annual NCP. This leads to very minimal imbalances in the seawater carbon inventory on an annual basis and, thus, minimal interannual variability in gas exchange. As a result, air-sea gas exchange at KEO is almost entirely driven by the influence of temperature on CO_2 solubility. At OSP, there is less interannual variability in physical processes that influence DIC due to a halocline that restricts the depth of winter mixing. On the other hand, there is a larger component of interannual variability in biology, which may be due to the numerous, and somewhat episodic nature of, iron supply mechanisms. The decoupling of physical and biological processes in this location through allochthonous iron input leads to larger interannual variability in air-sea CO_2 exchange, which compensates for the physical and biological imbalance.

The timing and magnitude of physical and biological processes is greatly important to the unraveling of regional carbon cycle dynamics; however, seawater carbon chemistry also plays an important and subtle role. The low buffer capacity (high Revelle factor) of waters near OSP relative to those in the subtropical gyre near KEO allows biology to be ~50% more effective at lowering seawater CO_2 levels near OSP. This means that 50% less biological activity is required at OSP than at KEO for the same surface ocean CO_2 reduction, suggesting that the coupling between air-sea CO_2 exchange and biology is very important in the eastern subarctic Pacific. The significant difference in seawater inorganic carbon characteristics between subtropical and subarctic waters may explain why biological processes play a dominant role in maintaining the North Pacific carbon sink across the subtropical-subarctic interface.

In addition to seasonal and interannual variability, coastal regions exhibit more dynamic, high-frequency environmental variations that are also of interest for closing the global carbon budget. Results from the seven-month deployment of a novel dissolved inorganic carbon (DIC) sensor on a moored buoy in Honolulu, Hawaii revealed the utility of high-frequency DIC observations in a near-shore fringing coral reef environment. Weekly to monthly DIC variability largely followed seawater density and, thus, large-scale circulation; however, superimposed on this was a large daily DIC cycle. Contemporaneous sea surface CO_2 measurements also revealed a daily cycle, but it was much smaller and more erratic. The dissimilarity between daily fluctuations in DIC and CO_2 was found to be caused by the competing effects that photosynthesis and calcification have on seawater CO_2 concentrations, which are additive for DIC. Thus, simultaneous inorganic and organic carbon production were confounded in the CO_2 signal, but emphasized in the DIC measurements. Additionally, the *in situ* measurements of DIC made it possible to identify a

terrestrial carbon source to the near-shore marine environment during heavy precipitation events. CO_2 measurements also peaked during these events, but, previously, it was not clear whether the CO_2 increase was due to elevated carbon content or lower pH levels in the terrestrial runoff. Findings from this test deployment provided new information about environmental conditions in this productive urban coastal region and displayed the utility of measuring the total carbon inventory (DIC) of seawater, in addition to CO_2, when assessing carbon cycling in dynamic coastal regions.

DIC variability occurs on all timescales, from hourly to interannual, and the importance of these variations depends on the questions being asked and the environmental signal that one is trying to study. The development of modern reference points for carbon cycling, at both the coastal and open-ocean scale, must include consideration of the physical, chemical and biological drivers of carbon inventory changes, as well as the complex interplay between them. While significant information continues to be gleaned from the amassing observations of air-sea CO_2 flux, *in situ* observations of DIC coupled with pH or xCO_2 will make it possible to discover new linkages between carbon cycle dynamics in complex and highly variable systems. Full constraint of the carbonate system from *in situ* high-frequency observations can contribute to better understanding of the processes governing carbon cycling, rather than their net effect, making it possible to more accurately project how ocean change will influence the global carbon cycle and climate.